

## **Copyright Warning & Restrictions**

**The copyright law of the United States (Title 17, United States Code) governs the making of photocopies or other reproductions of copyrighted material.**

**Under certain conditions specified in the law, libraries and archives are authorized to furnish a photocopy or other reproduction. One of these specified conditions is that the photocopy or reproduction is not to be “used for any purpose other than private study, scholarship, or research.” If a user makes a request for, or later uses, a photocopy or reproduction for purposes in excess of “fair use” that user may be liable for copyright infringement,**

**This institution reserves the right to refuse to accept a copying order if, in its judgment, fulfillment of the order would involve violation of copyright law.**

**Please Note: The author retains the copyright while the New Jersey Institute of Technology reserves the right to distribute this thesis or dissertation**

**Printing note: If you do not wish to print this page, then select “Pages from: first page # to: last page #” on the print dialog screen**



The Van Houten library has removed some of the personal information and all signatures from the approval page and biographical sketches of theses and dissertations in order to protect the identity of NJIT graduates and faculty.

## ABSTRACT

# REDUCED ORDER MODELS FOR FLUID-STRUCTURE INTERACTION SYSTEMS BY MIXED FINITE ELEMENT FORMULATION

by  
Ye Yang

In this work, mixed finite element formulations are introduced for acoustoelastic fluid-structure interaction (FSI) systems. For acoustic fluid, in addition to displacement-pressure ( $\mathbf{u}/p$ ) mixed formulation, a three-field formulation, namely, displacement-pressure-vorticity moment formulation ( $\mathbf{u} - p - \mathbf{\Lambda}$ ) is employed to eliminate some zero frequencies. This formulation is introduced in order to compute the coupled frequencies without the contamination of nonphysical spurious non-zero frequencies. Furthermore, gravitational forces are introduced to include the coupled sloshing mode. In addition,  $\mathbf{u}/p$  mixed formulation is the first time employed in solid. The numerical examples will demonstrate that the mixed formulations are capable of predicted coupled frequencies and mode shapes even if primary slosh, structural, and acoustic modes are within separate frequency ranges. That is to say, the mixed finite element formulations are used to deal with fluid and solid monolithically. In numerical analysis, boundary conditions, wetted surface, and skew systems are considered in order to obtain the symmetrical, nonsingular mass and stiffness matrices. An implicit time integration scheme, the Newmark method, is employed in the transient analysis. Appropriate finite elements corresponding to the mixed finite element formulations are selected based on the inf-sup condition, which is the fundamental solvability and stability condition of finite element methods. In addition, the inf-sup values of the FSI system using a sequence of three meshes are evaluated in order to identify and confirm that the 'locking' effect does not occur. The numerical examples in this work will also show that by imposing external forces near different coupled frequencies, predominant slosh, structural, and acoustic motions can be triggered in the FSI systems. Further, it

is discussed that the frequency range on which energy mainly focuses can be evaluated with Fast Fourier Transform, if the system is activated by single-frequency excitations.

In the second part, fluid-structure interaction systems with both immersed flexible structures and free surfaces are employed to study the traditional mode superposition methods and singular value decomposition (SVD) based model reduction methods, e.g., principal component analysis (PCA). The numerical results confirm that SVD-based model reduction methods are reliable by comparing the Rayleigh-Ritz quotients obtained by the principal singular vector and the natural frequencies of the system. If an initial excitation is loaded on a nodal points on the free surface or the structure, the corresponding natural frequency by the transient data of the first few time snapshots can be captured. Excellent agreements are confirmed between the original transient solutions and the data reconstructed with a few dominant principal components. The figures of energy are also plotted in order to verify the realization of this objective, which is recovering the transient data with a few principal components without losing dominant characteristics. The numerical results further demonstrate that different time steps lead to distinct mode shapes of the FSI system, if a combined eigenmode is given as the initial displacement. This is because the natural frequency of sloshing, structural, and acoustic modes are separated. Therefore, the errors between original transient data and recovered results *vs* different time steps are compared in order to find the appropriate time step and further capture all the eigenmodes. Finally, the coarse-grained system is employed to study the long-time behavior of the FSI system based on model reduction methods. The extrapolation results in coarse temporal scale can be obtained based on dominant principal components provided by PCA. The data at some time instances in fine temporal scale can be neglected. The numerical results show excellent agreement for some generic initial conditions.

**REDUCED ORDER MODELS FOR FLUID-STRUCTURE  
INTERACTION SYSTEMS BY MIXED FINITE ELEMENT  
FORMULATION**

by  
**Ye Yang**

**A Dissertation  
Submitted to the Faculty of  
New Jersey Institute of Technology and  
Rutgers, The State University of New Jersey – Newark  
in Partial Fulfillment of the Requirements for the Degree of  
Doctor of Philosophy in Mathematical Sciences**

**Department of Mathematical Sciences, NJIT  
Department of Mathematics and Computer Science, Rutgers-Newark**

**August 2009**

Copyright © 2009 by Ye Yang

ALL RIGHTS RESERVED

APPROVAL PAGE

REDUCED ORDER MODELS FOR FLUID-STRUCTURE  
INTERACTION SYSTEMS BY MIXED FINITE ELEMENT  
FORMULATION

Ye Yang

7/20/09  
\_\_\_\_\_  
Sheldon Wang, Ph.D, Dissertation Advisor Date  
Associate Professor, Department of Mathematical Sciences, NJIT

7/20/09  
\_\_\_\_\_  
Eliza Michalopoulou, Ph.D, Committee Member Date  
Professor, Department of Mathematical Sciences, NJIT

7/20/09  
\_\_\_\_\_  
Michael Siegel, Ph.D, Committee Member Date  
Professor, Department of Mathematical Sciences, NJIT

7-20-2009  
\_\_\_\_\_  
David J. Horntrop, Ph.D, Committee Member Date  
Associate Professor, Department of Mathematical Sciences, NJIT

7/20/09  
\_\_\_\_\_  
Hongya Ge, Ph.D, Committee Member Date  
Associate Professor, Department of Electrical and Computer Engineering, NJIT

## BIOGRAPHICAL SKETCH

**Author:** Ye Yang  
**Degree:** Doctor of Philosophy  
**Date:** August 2009

### **Undergraduate and Graduate Education:**

- Doctor of Philosophy in Mathematical Sciences,  
New Jersey Institute of Technology, Newark, NJ, 2009
- Master of Science in Applied Mathematics,  
New Jersey Institute of Technology, Newark, NJ, 2009
- Bachelor of Science in Applied Mathematics,  
Tianjin University, Tianjin, China, 2005

**Major:** Mathematical Sciences

*To my beloved parents and my husband*

## ACKNOWLEDGMENT

I wish to express my special appreciation to my dissertation advisor Dr. Sheldon Wang for his valuable ideas, untiring guidance, continued encouragement and constructive advise. He brought me into my research area from the beginning of my graduate study. Not only a great mentor, he has also laid the foundation of my professional development.

I am very grateful to Dr. Hongya Ge and Dr. David J. Horntrop for their help in signal processing and stochastic issues. I wish to thank Dr. Eliza Michalopoulou for her kindness and encouragement to my research. Thanks to Dr. Michael Siegel for agreeing to be my committee member and the help during my preparation for the qualifying examinations.

Sincere appreciation to Dr. Daljit Ahluwalia for his assistance and advice throughout my graduate period. Thanks to him and the math department for the generous financial support. I would also like to thank all the faculty in the Department of Mathematical Sciences at NJIT. They gave me a lot of valuable assistance in the field of mathematics. I would also like to thank Dr. Kane for his help in completing the dissertation document.

My keen appreciation goes to my best friends Yan Liu and Xia Cai for their continued moral support, Tao Wu and Wen Deng for their help not only in computational aspects of my research but also in daily life. I also would like to thank all my friends in New Jersey Institute of Technology, who accompanied me throughout my graduate study.

Finally, I am forever indebted to my parents, Huizhi Zheng and Ruihua Yang, and my husband, Qiming Wang, for their understanding, endless patience and emotional support. Without them, I would not have been able to accomplish this.

## TABLE OF CONTENTS

Chapter	Page
1 INTRODUCTION . . . . .	1
2 MIXED FORMULATION AND FINITE ELEMENT FOR ACOUSTIC FLUID AND SOLID . . . . .	5
2.1 $\mathbf{u}/p$ and $\mathbf{u} - p - \Lambda$ Formulations for Fluid . . . . .	5
2.2 Displacement-Based and Displacement-Pressure Formulations for Solids	9
2.3 Acoustoelastic FSI System and Coupled Formulation . . . . .	14
2.4 Mixed Element and Interpolation Functions . . . . .	17
2.5 Mesh Generation and Stability Analysis . . . . .	18
3 NUMERICAL PROCEDURES . . . . .	21
3.1 Free Surface, Interface and Other Boundaries . . . . .	21
3.2 Modal Analysis . . . . .	23
3.3 Transient Analysis . . . . .	24
3.4 Model Reduction Method . . . . .	25
3.4.1 Mode Superposition Method . . . . .	25
3.4.2 Singular Value Decomposition and Principal Component Analysis	27
3.5 Ito Process and Brownian Motion . . . . .	30
4 NUMERICAL EXAMPLES . . . . .	33
4.1 Flexible Square Solid Vibrations in Acoustic Fluid . . . . .	33
4.2 2-D Rectangular Solid Attached to the Wall of an Open Cavity . . . .	46
4.3 Three Masses Connected to the Walls with Springs . . . . .	73
5 CONCLUSION . . . . .	82
APPENDIX A NEWMARK METHOD . . . . .	84
APPENDIX B PATHWISE AND MOMENTS APPROXIMATIONS . . . . .	86
APPENDIX C ORTHONORMAL BASIS CHOSEN BY SINGULAR VALUES	90
REFERENCES . . . . .	92

## LIST OF TABLES

Table	Page
4.1 Frequencies of sloshing/structural/acoustic modes of FSI model I. . . . .	35
4.2 Frequency range of FSI model II. . . . .	46
4.3 Eigenvalues and eigenvectors. . . . .	74
4.4 SVD and Raleigh-Ritz results with initial impulse. . . . .	75

## LIST OF FIGURES

Figure	Page
2.1 Two mixed elements for $\mathbf{u} - p - \Lambda$ formulation. Full numerical integration is used (i.e. $3 \times 3$ Gauss integration). . . . .	17
3.1 Illustration of principal component. . . . .	29
4.1 Model I: Square solid vibrations in acoustic fluid. . . . .	34
4.2 Macromesh generation figure by ADINA. . . . .	34
4.3 Displacement of sloshing/structural/acoustic modes of model I. . . . .	38
4.4 Pressure of sloshing/structural/acoustic modes of model I. . . . .	39
4.5 Pressure of sloshing/structural/acoustic modes of model I with 144 elements. . . . .	40
4.6 Numerical inf-sup test of $9 - 4c - 4c$ elements for $\mathbf{u} - p - \Lambda$ formulation. . . . .	41
4.7 Singular value of matrix $[\mathbf{K}_{up} \ \mathbf{K}_{ul}]$ for $\mathbf{u} - p - \Lambda$ formulation. . . . .	42
4.8 Displacement wave propagation of transient analysis of FSI model I. . . . .	44
4.9 Pressure wave propagation of transient analysis of FSI model I. . . . .	45
4.10 Model II: Rectangular solid attached to the wall of a open cavity. . . . .	46
4.11 Displacement of sloshing/structural/acoustic modes of model II. . . . .	48
4.12 Pressure of sloshing/structural/acoustic modes of model II. . . . .	49
4.13 Displacement wave propagation of transient analysis of model II. . . . .	50
4.14 Pressure wave propagation of transient analysis of model II. . . . .	51
4.15 Rayleigh-Ritz quotient <i>vs. nstep</i> for sloshing mode. . . . .	52
4.16 Rayleigh-Ritz quotient <i>vs. nstep</i> for structural mode. . . . .	52
4.17 Energy of transient data and recovered results of sloshing mode. . . . .	53
4.18 Energy of transient data and recovered results of structural mode. . . . .	53
4.19 Rayleigh-Ritz quotient/sloshing frequency <i>vs. nstep</i> . . . . .	55
4.20 Rayleigh-Ritz quotient/structural frequency <i>vs. nstep</i> . . . . .	55
4.21 Original and recovered transient data of sloshing mode. . . . .	56
4.22 Original and recovered transient data of structural mode. . . . .	57

**LIST OF FIGURES**  
(Continued)

Figure	Page
4.23 Original and recovered transient data of combined mode. . . . .	58
4.24 Data recovery by SVD and relaxation. . . . .	58
4.25 RMSD error <i>vs.</i> $dT$ with $dt = 0.01$ and $dt = 0.0001$ . . . . .	59
4.26 RMSD error <i>vs.</i> $nstep$ with different $dt$ . . . . .	59
4.27 Temporal coarse graining using SVD with snapshots at fine time step $dt$ , extrapolation at coarse time step $dT$ , and relaxation. . . . .	60
4.28 Energy of transient combined modes and recovered data by SVD and relaxation. . . . .	61
4.29 Energy of transient sloshing mode and recovered data by SVD and relaxation. . . . .	62
4.30 Rayleigh-Ritz quotient <i>vs.</i> $nstep$ for sloshing mode with white noise. . . . .	64
4.31 Rayleigh-Ritz quotient <i>vs.</i> $nstep$ for structural mode with white noise. . . . .	64
4.32 Displacement wave propagation of transient analysis with white noise. . . . .	66
4.33 Pressure wave propagation of transient analysis with white noise. . . . .	67
4.34 Sample variance <i>vs.</i> sample number. . . . .	67
4.35 Confidence intervals of displacement for increasing number of batches based on mean error. . . . .	69
4.36 Confidence intervals of velocity for increasing number of batches based on mean error. . . . .	69
4.37 Confidence intervals of displacement for increasing number of snapshots based on mean error. . . . .	70
4.38 Confidence intervals of velocity for increasing number of snapshots based on mean error. . . . .	70
4.39 Confidence intervals of displacement for increasing number of batches based on absolute error. . . . .	72
4.40 Confidence intervals of velocity for increasing number of batches based on absolute error. . . . .	72
4.41 Model III: Three masses connected to the walls with springs. . . . .	73
4.42 Rayleigh-Ritz quotients <i>vs.</i> $nstep$ activated by initial force proportional to the first eigenmode. . . . .	76

**LIST OF FIGURES**  
(Continued)

Figure	Page
4.43 Rayleigh-Ritz quotients <i>vs. nstep</i> activated by initial force proportional to the second eigenmode. . . . .	76
4.44 Rayleigh-Ritz quotients <i>vs. nstep</i> activated by initial force proportional to the third eigenmode. . . . .	77
4.45 Power spectrum <i>vs.</i> frequency with $k=1,2,3$ . . . . .	79
4.46 Explicit and numerical solution of displacement/velocity <i>vs.</i> time. . . . .	80
4.47 Displacement/velocity <i>vs.</i> time by implicit Euler method. . . . .	80
4.48 Raleigh-Ritz quotient <i>vs</i> nstep with noise. . . . .	81
B.1 Explicit and numerical solution of displacement/velocity <i>vs.</i> time. . . . .	87
B.2 Confidence intervals of displacement for increasing numbers of batches based on absolute error. . . . .	87
B.3 Confidence intervals of velocity for increasing numbers of batches based on absolute error. . . . .	88
B.4 Confidence intervals of displacement for increasing time based on mean error. . . . .	89
B.5 Confidence intervals of velocity for increasing time based on mean error. . . . .	89

# CHAPTER 1

## INTRODUCTION

Since the 1950s, increasing effort has been devoted to the applications of finite element method (FEM) [10], even though the rigorous mathematical foundation was not provided by Strang and Fix until 1973. Among these applications, the analysis of fluid-structure interaction by finite element method is generally used for numerical modeling of physical systems in a wide variety of engineering applications, such as nuclear reactor components, naval structures, biomedical engineering, aerospace industry, underwater explosions, and so on.

Various finite element formulations based on displacement, pressure, and potential have been applied to problems involving the interaction between acoustic fluids and elastic structures. Pressure approach [11], [13], [18], [35], [44] has the advantages of fewer unknowns and a smaller matrix bandwidth, but leads to a nonsymmetric stiffness matrix. On the other hand, the displacement approach [4], [5], [6], [43] results in symmetric coefficient matrices and the condition of a wetted surface is easier to implement. However, it is widely reported that the pure displacement-based fluid elements in frequency and transient analysis produce spurious nonzero frequency rotational modes [22], [26]. Spurious modes are scattered throughout the whole frequency spectrum and therefore hard to recognize. Various methods have been performed to explore the origins of these spurious frequencies, but only recently have the true causes been identified. One of the primary reasons is that the use of pure displacement formulation exhibits 'locking' phenomenon which can be eventually overcome by mixed elements satisfying the inf-sup condition. Extensive research has been devoted to the improvement of finite element formulations for acoustic fluid-structure interaction problems, including a 4-node element based on a reduced

integration technique in the stiffness calculation in combination with a projection on the element mass matrix [9], the displacement potential, and pressure formulation [34]. Finite element formulations involving velocity potential [16], [36], [37] provide a good alternative to displacement-based fluid element for steady state problems with damping terms, however, when they are applied to frequency and transient models, some modifications are necessary. The mixed displacement/ pressure finite element formulation for both fluids and solids proposed by Wang and Bathe [41], has been proven to be reliable and free of spurious non-zero frequencies [2], [42]. In this work, the displacement-pressure-vorticity moment formulation is employed to acoustic fluid and the displacement-pressure formulation is implement to elastic solid. Since the problems considered in this work are FSI systems, the vibration of the elastic solid, the acoustic properties of the fluid surrounding the elastic body and the interaction between acoustic fluid and solid need to be taken into account carefully.

In order to obtain sufficiently continuous solutions with mixed finite element formulations, a dense finite element mesh is needed. Consequently, the overall number of degrees of freedom may be quite large. In practice, it is anticipated that model reduction methods must be implemented to the FSI systems. One kind of the most commonly used model reduction methods is the mode superposition method [3], [13]; another kind is the so-called singular value decomposition-based model reduction method, including principal component analysis and singular value decomposition [12], [14]. The earliest descriptions of PCA were given by Pearson (1901) and Hotelling (1933) [24]. Eckart and Young indicated that SVD can be applied for general rectangular matrices in 1939. SVD and PCA are very important and fundamental tools in many areas [20], [25], [27], [29], for example, spatial coherence in turbulence problems [23], [32], [39], structure dynamics [1], [19], digital signal processing [7], microelectromechanical systems [30], and so on. In this work, we demonstrate by using a simple two-dimensional acoustoelastic model with submerged structure and free surface that

the SVD-based method can be applied to FSI systems and that the method is reliable in comparison with the mode superposition method.

In essence, there is a fundamental difference between mode superposition method and singular value decomposition-based model reduction methods. With SVD-based model reduction, if the material properties of the system are unknown, the eigenmodes can still be constructed by taking the first few dominant principal components of transient data. Furthermore, the natural frequencies of the system can be achieved by performing the Rayleigh-Ritz analysis or time-frequency analysis of the principal components or eigen modes.

In Chapter 2, the displacement-pressure ( $\mathbf{u}/p$ ) formulation and displacement-pressure-vorticity moment ( $\mathbf{u} - p - \Lambda$ ) formulation for acoustic fluid are briefly reviewed as well as the pure displacement-based formulation and displacement-pressure formulation for structure with corresponding mixed elements. Mixed formulations are introduced to avoid the aforementioned deficiencies, especially the appearance of spurious non-zero circulation frequency. Three basic assumptions have been used in the formulation of fluid elements: (a) The fluid is compressible and inviscid. (b) Interaction between mechanical and thermal processes is negligible. (c) The deflections of elements are small and therefore all analyses are linear. In addition, the mixed elements and mesh generation satisfied inf-sup condition are introduced to proceed the finite element methods.

In Chapter 3, some details of the numerical procedures will be addressed, e.g., boundary conditions, modal analysis, and transient analysis. Two kinds of model reduction methods, mode superposition method and SVD (PCA), are also described in this section. In addition, explicit solution and numerical scheme to the stochastic differential equation with additive noise are introduced.

The numerical results of three examples are shown in Chapter 4. For the first FSI system, the dominant natural frequencies and mode shapes are mainly

considered. The results are assumed to be a linear combination of the eigenmodes. In addition, inf-sup test, which is the crucial criterion on effectiveness and stability, is performed in order to obtain the convergent inf-sup value. The other stability condition, ellipticity condition, can be automatically satisfied based on the mixed finite element formulations and numerical scheme. Therefore, it can be concluded that the  $\mathbf{u} - p - \Lambda$  formulation for fluid and  $\mathbf{u}/p$  formulation for structure are capable of handling complex fluid-structure interaction systems with both immersed flexible structures and free surfaces. In the second FSI system, the first few principal components of the original data are employed to recover the transient results without losing characteristic information. Then each fluid nodal point is considered as a fluid particle moving randomly to anywhere in a 2-dimensional space. In temporal-discretized system, each nodal point undergoes a random displacement as well as the movement caused by other exterior force. The displacements at each time step are assumed to be independent, identical distributed random variables. In essence, this procedure is the Brownian motion. It is included in the FSI model in order to describe the nature of the fluid motion more accurately. The comparison of the relationship between mode superposition and singular value decomposition methods is shown in the spring test problem.

## CHAPTER 2

# MIXED FORMULATION AND FINITE ELEMENT FOR ACOUSTIC FLUID AND SOLID

### 2.1 $\mathbf{u}/p$ and $\mathbf{u} - p - \Lambda$ Formulations for Fluid

In linear analysis, for the isentropic and inviscid fluid undergoing small vibrations, the momentum balance and constitutive equations show

$$\rho \ddot{\mathbf{u}} + \nabla p - \mathbf{f}^B = \mathbf{0} \quad (2.1)$$

$$\nabla \cdot \mathbf{u} + \frac{p}{\beta} = 0 \quad (2.2)$$

where  $\rho$ ,  $\mathbf{u}$ ,  $p$ ,  $\mathbf{f}^B$  and  $\beta$  represent the density, displacement, pressure, body force and fluid bulk modulus, respectively.

Assuming the inertia force  $-\rho \ddot{\mathbf{u}}$  is included in  $\mathbf{f}^B$  term and combining Eqs. (2.1) and (2.2), a new governing equation only with respect to displacement  $\mathbf{u}$  can be composed into

$$\beta \nabla (\nabla \cdot \mathbf{u}) + \mathbf{f}^B = 0. \quad (2.3)$$

For any smooth scalar-valued function  $\phi$ ,  $\nabla \times \nabla \phi = 0$ . Therefore, if  $\mathbf{v}$  denotes the velocity of the fluid, Eq. (2.3) shows that

$$\frac{\partial}{\partial t} (\nabla \times \mathbf{v}) = 0. \quad (2.4)$$

That is to say, the vorticity of the motion does not change with time. Supposing the fluid starts from rest, the following irrotationality constraint can be obtained

$$\nabla \times \mathbf{u} = 0. \quad (2.5)$$

The variational form of Eq. (2.3) is given by

$$\int_{V_f} \{\beta(\nabla \cdot \mathbf{u})(\nabla \cdot \delta \mathbf{u}) - \mathbf{f}^B \cdot \delta \mathbf{u}\} dV + \int_{S_f} \bar{p} \delta u_n^s dS = 0, \quad (2.6)$$

where  $V_f$  and  $S_f$  stand for the fluid domain and Neumann boundary respectively,  $u_n^s$  is the displacement normal to  $S_f$ , and  $\bar{p}$  is the given pressure on  $u_n^s$ ; whereas the corresponding variational indicator is

$$\Pi = \int_{V_f} \left\{ \frac{\beta}{2} (\nabla \cdot \mathbf{u})^2 - \mathbf{f}^B \cdot \mathbf{u} \right\} dV + \int_{S_f} \bar{p} u_n^s dS. \quad (2.7)$$

The above equation is the often used pure displacement-based formulation. It has been observed that circulation modes with nonzero frequencies may yield other than the zero frequency circulation modes. The spurious nonzero frequencies are difficult to recognize and discard in practice and should not be present in a reliable finite element analysis. In addition, when the fluid acts as almost incompressible, the usual constraint of near incompressibility is shown as Eq. (2.2). However, the pure displacement-based formulation with irrotationality and (almost) incompressibility conditions leads to a much too stiff response, i.e., 'locking' behavior.

In order to eliminate the spurious nonzero frequency and modify the 'locking' behavior, the penalty-form variational indicator based on constraint (2.2) is introduced

$$\Pi = \int_{V_f} \left\{ \frac{p^2}{2\beta} - \mathbf{u} \cdot \mathbf{f}^B - \lambda_p \left( \frac{p}{\beta} + \nabla \cdot \mathbf{u} \right) \right\} dV + \int_{S_f} \bar{p} u_n^s dS, \quad (2.8)$$

where  $\lambda_p$  is the Lagrange multiplier. The variable unknowns are displacement  $\mathbf{u}$  and pressure  $p$ . For this indicator, the first term corresponds to the strain energy with respect to pressure, the second term stands for the external body force potential, which also includes the gravity force (it will be discussed in detail in Chapter 4.), and the last term is the potential due to the boundary pressure. Eq. (2.8) is often called  $\mathbf{u}/p$  mixed finite element formulation.

Notice that the irrotationality constraint is not imposed in the  $\mathbf{u}/p$  formulation and will therefore result in too many exact zero frequencies. In order to eliminate these zero frequency modes, a modification of Eq. (2.5) is introduced

$$\nabla \times \mathbf{u} = \frac{\mathbf{\Lambda}}{\alpha}, \quad (2.9)$$

where  $\mathbf{\Lambda}$  is the vorticity moment and  $\alpha$  is a very large number.

With this constraint, another variational indicator (which is based on the weak form) is defined by the Lagrange multiplier method on the bases of  $\mathbf{u}/p$  formulation

$$\begin{aligned} \Pi &= \int_{V_f} \left\{ \frac{p^2}{2\beta} - \mathbf{u} \cdot \mathbf{f}^B - \lambda_p \left( \frac{p}{\beta} + \nabla \cdot \mathbf{u} \right) + \frac{\mathbf{\Lambda} \cdot \mathbf{\Lambda}}{2\alpha} - \boldsymbol{\lambda}_\Lambda \cdot \left( \frac{\mathbf{\Lambda}}{\alpha} - \nabla \times \mathbf{u} \right) \right\} dV \\ &+ \int_{S_f} \bar{p} u_n^S dS, \end{aligned} \quad (2.10)$$

where  $\boldsymbol{\lambda}_\Lambda$  is a Lagrange multiplier vector corresponding to the vorticity moment; whereas the unknowns of this equation are  $\mathbf{u}$ ,  $p$ , and  $\mathbf{\Lambda}$ .

The fourth term is added to statically condense out the degrees of freedom of the vorticity moment  $\mathbf{\Lambda}$ . This will not change the numerical results. From the numerical tests, it is found that  $\alpha$  can be any numerically reasonable value larger than  $\beta$ , for example,  $100\beta \leq \alpha \leq 10^6\beta$ . In this work,  $\alpha$  is defined as  $1000\beta$ .

Invoking the stationarity of  $\Pi$  with respect to  $\mathbf{u}$ ,  $p$ ,  $\mathbf{\Lambda}$  and identifying  $\lambda_p = p$  and  $\boldsymbol{\lambda}_\Lambda = \mathbf{\Lambda}$ ,

$$\begin{aligned} \delta\Pi &= \int_{V_f} \left\{ -\frac{p}{\beta} \delta p - \delta \mathbf{u} \cdot \mathbf{f}^B + \delta \mathbf{u} \cdot (\nabla p) - (\nabla \cdot \mathbf{u}) \delta p - \frac{\delta \mathbf{\Lambda} \cdot \mathbf{\Lambda}}{\alpha} + \delta \mathbf{\Lambda} \cdot (\nabla \times \mathbf{u}) \right. \\ &+ \left. \delta \mathbf{u} \cdot (\nabla \times \mathbf{\Lambda}) \right\} dV \\ &= \int_{V_f} \left\{ (-\mathbf{f}^B + \nabla p + \nabla \times \mathbf{\Lambda}) \cdot \delta \mathbf{u} - \left( \frac{p}{\beta} + \nabla \cdot \mathbf{u} \right) \delta p \right. \\ &+ \left. \left( \nabla \times \mathbf{u} - \frac{\mathbf{\Lambda}}{\alpha} \right) \cdot \delta \mathbf{\Lambda} \right\} dV \\ &= 0. \end{aligned}$$

This preceding equation leads to three field equations

$$-\mathbf{f}^B + \nabla p + \nabla \times \mathbf{\Lambda} = \mathbf{0}, \quad (2.11)$$

$$\frac{p}{\beta} + \nabla \cdot \mathbf{u} = 0, \quad (2.12)$$

$$\nabla \times \mathbf{u} - \frac{\mathbf{\Lambda}}{\alpha} = 0, \quad (2.13)$$

with the boundary conditions

$$\mathbf{u} \cdot \mathbf{n} = \bar{u}_n \quad \text{on } S_u, \quad (2.14)$$

$$p = \bar{p} \quad \text{on } S_f, \quad (2.15)$$

$$\mathbf{\Lambda} = \mathbf{0} \quad \text{on } S, \quad (2.16)$$

where the inertia force  $-\rho\ddot{\mathbf{u}}$  is included in  $\mathbf{f}^B$  and  $S = S_u \cup S_f$  ( $S_u \cap S_f = 0$ ). The pressure  $\bar{p}$  is commonly assigned to be zero on the free surface. However, it can also be assumed to be a time-variant function which activates the fluid motions (section 4.1).

Applying the standard Galerkin finite element discretization, and considering a typical element,

$$\mathbf{u} = \mathbf{H}\hat{\mathbf{U}}, \quad (2.17)$$

$$p = \mathbf{H}_p\hat{\mathbf{P}}, \quad (2.18)$$

$$\mathbf{\Lambda} = \mathbf{H}_\Lambda\hat{\mathbf{\Lambda}}, \quad (2.19)$$

$$\nabla \cdot \mathbf{u} = (\nabla \cdot \mathbf{H})\hat{\mathbf{U}} = \mathbf{B}\hat{\mathbf{U}}, \quad (2.20)$$

$$\nabla \times \mathbf{u} = (\nabla \times \mathbf{H})\hat{\mathbf{U}} = \mathbf{D}\hat{\mathbf{U}}, \quad (2.21)$$

where  $\hat{\mathbf{U}}$ ,  $\hat{\mathbf{P}}$ , and  $\hat{\mathbf{\Lambda}}$  list all the nodal point displacements, pressure, and vorticity moment, respectively in global coordinates and  $\mathbf{H}$ ,  $\mathbf{H}_p$ ,  $\mathbf{H}_\Lambda$  are the displacement, pressure, and vorticity moment interpolation matrix respectively.

Therefore, the field equations can be expressed into matrix form with respect to  $\hat{\mathbf{U}}$ ,  $\hat{\mathbf{P}}$ ,  $\hat{\mathbf{\Lambda}}$

$$\begin{pmatrix} \mathbf{M} & \mathbf{0} & \mathbf{0} \\ \mathbf{0} & \mathbf{0} & \mathbf{0} \\ \mathbf{0} & \mathbf{0} & \mathbf{0} \end{pmatrix} \begin{pmatrix} \ddot{\hat{\mathbf{U}}} \\ \ddot{\hat{\mathbf{P}}} \\ \ddot{\hat{\mathbf{\Lambda}}} \end{pmatrix} + \begin{pmatrix} \mathbf{0} & \mathbf{L} & \mathbf{Q} \\ \mathbf{L}^T & \mathbf{A} & \mathbf{0} \\ \mathbf{Q}^T & \mathbf{0} & \mathbf{G} \end{pmatrix} \begin{pmatrix} \hat{\mathbf{U}} \\ \hat{\mathbf{P}} \\ \hat{\mathbf{\Lambda}} \end{pmatrix} = \begin{pmatrix} \mathbf{R} \\ \mathbf{0} \\ \mathbf{0} \end{pmatrix}, \quad (2.22)$$

with

$$\begin{aligned} \mathbf{M} &= \int_{V_f} \rho \mathbf{H}^T \mathbf{H} dV, & \mathbf{L} &= - \int_{V_f} \mathbf{B}^T \mathbf{H}_p dV, \\ \mathbf{Q} &= \int_{V_f} \mathbf{D}^T \mathbf{H}_\Lambda dV, & \mathbf{A} &= - \int_{V_f} \frac{1}{\kappa} \mathbf{H}_p^T \mathbf{H}_p dV, \\ \mathbf{G} &= - \int_{V_f} \frac{1}{\alpha} \mathbf{H}_\Lambda^T \mathbf{H}_\Lambda dV, & \mathbf{R} &= - \int_{S_f} (\mathbf{H}_n^s)^T \bar{p} dS. \end{aligned}$$

Due to the coefficient of different variables, the entries of the mass matrix and stiff matrix can be rewrote with subscripts indicating their corresponding unknowns

$$\begin{pmatrix} \mathbf{M}_{uu} & \mathbf{0} & \mathbf{0} \\ \mathbf{0} & \mathbf{0} & \mathbf{0} \\ \mathbf{0} & \mathbf{0} & \mathbf{0} \end{pmatrix} \begin{pmatrix} \ddot{\hat{\mathbf{U}}} \\ \ddot{\hat{\mathbf{P}}} \\ \ddot{\hat{\mathbf{\Lambda}}} \end{pmatrix} + \begin{pmatrix} \mathbf{0} & \mathbf{K}_{up} & \mathbf{K}_{ul} \\ \mathbf{K}_{pu} & \mathbf{K}_{pp} & \mathbf{0} \\ \mathbf{K}_{lu} & \mathbf{0} & \mathbf{K}_{ll} \end{pmatrix} \begin{pmatrix} \hat{\mathbf{U}} \\ \hat{\mathbf{P}} \\ \hat{\mathbf{\Lambda}} \end{pmatrix} = \begin{pmatrix} \mathbf{R} \\ \mathbf{0} \\ \mathbf{0} \end{pmatrix}. \quad (2.23)$$

## 2.2 Displacement-Based and Displacement-Pressure Formulations for Solids

Consider a structure with isotropic material

$$\tau_{ij,j} + f_i^B = 0 \quad \text{in } V, \quad (2.24)$$

$$\tau_{ij}n_j = f_i^{S_f} \quad \text{on } S_f, \quad (2.25)$$

$$u_i = u_i^{S_u} \quad \text{on } S_u, \quad (2.26)$$

where  $\tau$ ,  $f^B$ ,  $n_j$ , and  $f^{S_f}$  represent the stress, body force, outward normal direction, and the applied traction on the Neumann boundary  $S_f$ , respectively.

Consider any arbitrary chosen continuous displacement  $\bar{u}_i$  satisfying

$$\bar{u}_i = 0 \quad \text{on } S_u, \quad (2.27)$$

based on Eq. (2.24), the following equation can be obtained

$$\int_V (\tau_{ij,j} + f_i^B) \bar{u}_i dV = 0, \quad (2.28)$$

where  $\bar{u}_i$  is called virtual displacement. The virtual displacements are not real displacements which the body actually undergoes as a consequence of the loading on the body; instead they are used to establish the integral equilibrium equations. Apply the mathematical identity  $(\tau_{ij}\bar{u}_i)_{,j} = \tau_{ij,j}\bar{u}_i + \tau_{ij}\bar{u}_{i,j}$ , Eq. (2.28) can be written as

$$\int_V [(\tau_{ij}\bar{u}_i)_{,j} - \tau_{ij}\bar{u}_{i,j} + f_i^B\bar{u}_i] dV = 0. \quad (2.29)$$

From the divergence theorem, Eq. (2.29) turns to be

$$\int_V (-\tau_{ij}\bar{u}_{i,j} + f_i^B\bar{u}_i) dV + \int_S (\tau_{ij}\bar{u}_i)n_j dS = 0. \quad (2.30)$$

Employing the boundary condition (2.25), it can be obtained that

$$\int_V (-\tau_{ij}\bar{u}_{i,j} + f_i^B\bar{u}_i) dV + \int_S f_i^{S_f}\bar{u}_i^{S_f} dS = 0. \quad (2.31)$$

Since the stress tensor is symmetric ( $\tau_{ij} = \tau_{ji}$ ), it is known that

$$\tau_{ij}\bar{u}_{i,j} = \tau_{ij} \left[ \frac{1}{2}(\bar{u}_{i,j} + \bar{u}_{j,i}) \right] = \tau_{ij}\bar{\epsilon}_{ij}, \quad (2.32)$$

Substituting the notation above into Eq. (2.31), the desirable result can be obtained as

$$\int_V \tau_{ij} \bar{\epsilon}_{ij} dV = \int_V f_i^B \bar{u}_i dV + \int_{S_f} f_i^{S_f} \bar{u}_i^{S_f} dS. \quad (2.33)$$

In fact, the equation above comes from the principle of virtual displacements

$$\int_V \bar{\epsilon}^T \tau dV = \int_V \bar{u}^T f^B dV + \int_{S_f} \bar{u}_i^{S_f T} f^{S_f} dS + \sum_i \bar{U}^{iT} R_c^i. \quad (2.34)$$

Here the concentrated load  $R_c^i$  is also included, where  $i$  denotes the point of load application, even though such force can be considered as part of surface traction  $f^{S_f}$  over a very small area.

Applying the standard Galerkin discretization

$$\mathbf{u} = \mathbf{H}\hat{\mathbf{U}}, \quad (2.35)$$

$$\boldsymbol{\epsilon} = \mathbf{B}\hat{\mathbf{U}}, \quad (2.36)$$

and the constitutive relation  $\boldsymbol{\tau} = \mathbf{C}\boldsymbol{\epsilon} + \boldsymbol{\tau}^I$  ( $\boldsymbol{\tau}^I$  is the initial stresses for given elements) to Eq. (2.34), we obtain the matrix form pure displacement based formulation with respect to displacement  $\mathbf{U}$

$$\mathbf{K}\mathbf{U} = \mathbf{R}_B + \mathbf{R}_S - \mathbf{R}_I + \mathbf{R}_C, \quad (2.37)$$

with

$$\mathbf{K} = \int_V \mathbf{B}^T \mathbf{C} \mathbf{B} dV, \quad \mathbf{R}_B = \int_V \mathbf{H}^T \mathbf{f}^B dV,$$

$$\mathbf{R}_S = \int_V \mathbf{H}^{ST} \mathbf{f}^S dS, \quad \mathbf{R}_I = \int_V \mathbf{B}^T \boldsymbol{\tau}^I dV.$$

If the material is almost incompressible, the constitutive relations shows

$$\tau_{ij} = \kappa \epsilon_v \delta_{ij} + 2G \epsilon'_{ij}, \quad (2.38)$$

where  $\kappa$  is the bulk modulus with  $\kappa = \frac{E}{3(1-2\nu)}$ ,  $G$  is the shear modulus,  $\epsilon_v$  is the volumetric strain with  $\epsilon_v = \epsilon_{kk}$  in Cartesian coordinates and  $\epsilon'_{ij}$  are the deviatoric strain components with respect to Kronecker delta,  $\epsilon'_{ij} = \epsilon_{ij} - \frac{\epsilon_v}{3}\delta_{ij}$ .

If the Poisson's ratio  $\nu$  gradually increases to 0.5, the bulk modulus  $\kappa$  approaches infinity and the volumetric strain  $\epsilon_v$  goes to zero. However, it is difficult to evaluate the pressure from the relationship  $p = -\kappa\epsilon_v$  when the bulk modulus is very large, even though the pressure is finite for this case. Therefore, the governing equation should involve another unknown, namely, pressure  $p$  independent of the displacement unknown  $\mathbf{u}$ . Consequently, the relation can be achieved as

$$\boldsymbol{\tau}_{ij} = -p\boldsymbol{\delta}_{ij} + 2G\boldsymbol{\epsilon}'_{ij}. \quad (2.39)$$

Now the principle of virtual work is introduced in terms of independent variables  $\mathbf{u}$  and  $p$

$$\int_V (\bar{\boldsymbol{\epsilon}}'^T : \mathbf{S} - \bar{\epsilon}_v p \mathbf{I}) dV = \bar{R}, \quad (2.40)$$

$$\int_V \left( \frac{p}{\kappa} + \epsilon_v \right) \bar{p} dV = 0, \quad (2.41)$$

where  $\mathbf{S} = \mathbf{C}'\boldsymbol{\epsilon}'$  and  $\boldsymbol{\epsilon}'$  are the deviatoric stress and strain vectors which satisfy  $\mathbf{S} = \boldsymbol{\tau} + p\boldsymbol{\delta}$ ,  $\boldsymbol{\epsilon}' = \boldsymbol{\epsilon} - \frac{1}{3}\epsilon_v\boldsymbol{\delta}$ ; whereas the overbar indicates virtual quantities and  $\bar{R}$  corresponds to the net external virtual work.

Implementing the standard Galerkin discretization as above

$$\boldsymbol{\epsilon}' = \mathbf{B}_D \hat{\mathbf{U}} \quad (2.42)$$

$$\epsilon_v = \mathbf{B}_v \hat{\mathbf{U}} \quad (2.43)$$

$$p = \mathbf{H}_p \hat{\mathbf{P}}, \quad (2.44)$$

the matrix form can be obtained with respect to  $\mathbf{U}$  and  $P$

$$\begin{pmatrix} \mathbf{K}_{uu} & \mathbf{K}_{up} \\ \mathbf{K}_{pu} & \mathbf{K}_{pp} \end{pmatrix} \begin{pmatrix} \hat{\mathbf{U}} \\ \hat{P} \end{pmatrix} = \begin{pmatrix} \mathbf{R} \\ \mathbf{0} \end{pmatrix}, \quad (2.45)$$

where  $\mathbf{B}_D$  and  $\mathbf{B}_v$  are the deviatoric and volumetric strain interpolation matrix respectively and the components of stiffness matrix are defined as

$$\mathbf{K}_{uu} = \int_v \mathbf{B}_D^T \mathbf{C}' \mathbf{B}_D dV, \quad \mathbf{K}_{pp} = - \int_v \frac{1}{\kappa} \mathbf{H}_p^T \mathbf{H}_p dV,$$

$$\mathbf{K}_{up} = \mathbf{K}_{pu} = - \int_v \mathbf{B}_v^T \mathbf{H}_p dV.$$

Both Eqs. (2.37) and (2.45) can be rewritten as

$$\mathbf{K}\mathbf{U} = \mathbf{R}. \quad (2.46)$$

Eq. (2.46) is a statement of static equilibrium of the solid element assemblage. If the loads are applied rapidly, the inertia forces need to be considered. Using d'Alembert's principle, the element inertia forces can be directly included as part of the body forces. Assuming the element accelerations are expressed in the same way as the element displacements, the contribution to the total body force is

$$\mathbf{R}_B = \int_V \mathbf{H}^T [\mathbf{f}^B - \rho \mathbf{H}\ddot{\mathbf{U}}] dV, \quad (2.47)$$

where  $\mathbf{R}_B$  is the body force,  $\rho$  is the mass density and  $\ddot{\mathbf{U}}$  lists the nodal point accelerations, i.e. the second time derivative of  $\mathbf{U}$ .

At this point,  $\mathbf{f}^B$  no longer includes the inertia forces. Then the equilibrium equations are

$$\mathbf{M}\ddot{\mathbf{U}} + \mathbf{K}\mathbf{U} = \mathbf{R}, \quad (2.48)$$

where the matrix  $\mathbf{M}$  is the mass matrix of the structure,

$$\mathbf{M} = \int_V \rho \mathbf{H}^T \mathbf{H} dV.$$

The damping term can also be imposed in this method, i.e., introducing the damping forces as additional contributions to the body forces, therefore

$$\mathbf{R}_B = \int_V \mathbf{H}^T [\mathbf{f}^B - \rho \mathbf{H} \ddot{\mathbf{U}} - c \mathbf{H} \dot{\mathbf{U}}] dV, \quad (2.49)$$

where  $c$  is the damping property parameter and  $\dot{\mathbf{U}}$  is a vector of the nodal point velocities.

The equilibrium equations are

$$\mathbf{M} \ddot{\mathbf{U}} + \mathbf{C} \dot{\mathbf{U}} + \mathbf{K} \mathbf{U} = \mathbf{R}, \quad (2.50)$$

where the matrix  $\mathbf{C}$  is the damping matrix,

$$\mathbf{C} = \int_V c \mathbf{H}^T \mathbf{H} dV.$$

Of course, there may be some other methods in order to add the damping term, e.g., Rayleigh damping in mode superposition method,

$$\mathbf{C} = \alpha \mathbf{M} + \beta \mathbf{K},$$

where  $\alpha$  and  $\beta$  are two parameters dependent on the damping ratios of the system.

### 2.3 Acoustoelastic FSI System and Coupled Formulation

To clearly illustrate the coupling procedures for mixed formulations, the following generic governing equations are introduced with subscripts to identify the entries for acoustic fluid elements and linear elastic structure elements. Taking pure displacement-based formulation for solid and  $\mathbf{u}/p$  formulation for fluid as an example, the equation

of solid and fluid are

$$\begin{pmatrix} \mathbf{M}_{ss} & \mathbf{M}_{sc} \\ \mathbf{M}_{cs} & \mathbf{M}_{cc}^s \end{pmatrix} \begin{pmatrix} \ddot{\mathbf{U}}_s \\ \ddot{\mathbf{U}}_c \end{pmatrix} + \begin{pmatrix} \mathbf{K}_{ss} & \mathbf{K}_{sc} \\ \mathbf{K}_{cs} & \mathbf{K}_{cc}^s \end{pmatrix} \begin{pmatrix} \mathbf{U}_s \\ \mathbf{U}_c \end{pmatrix} = \begin{pmatrix} \mathbf{R}_s \\ \mathbf{R}_c^s \end{pmatrix}, \quad (2.51)$$

and

$$\begin{pmatrix} \mathbf{M}_{ff} & \mathbf{M}_{fc} & \mathbf{0} \\ \mathbf{M}_{cf} & \mathbf{M}_{cc}^f & \mathbf{0} \\ \mathbf{0} & \mathbf{0} & \mathbf{0} \end{pmatrix} \begin{pmatrix} \ddot{\mathbf{U}}_f \\ \ddot{\mathbf{U}}_c \\ \ddot{\mathbf{P}} \end{pmatrix} + \begin{pmatrix} \mathbf{K}_{ff} & \mathbf{K}_{fc} & \mathbf{K}_{fp} \\ \mathbf{K}_{cf} & \mathbf{K}_{cc}^f & \mathbf{K}_{cp} \\ \mathbf{K}_{pf} & \mathbf{K}_{pc} & \mathbf{K}_{pp} \end{pmatrix} \begin{pmatrix} \mathbf{U}_f \\ \mathbf{U}_c \\ \mathbf{P} \end{pmatrix} = \begin{pmatrix} \mathbf{R}_f \\ \mathbf{R}_c^f \\ \mathbf{0} \end{pmatrix}, \quad (2.52)$$

respectively, where  $\mathbf{U}_s$ ,  $\mathbf{U}_f$ , and  $\mathbf{U}_c$  refer to the nodal displacement unknowns in the structure interior, fluid interior, and fluid-structure interface, respectively. In the practical analysis,  $\mathbf{U}_c$  consists of normal displacement components of fluid elements.

In the assemblage process, Eqs. (2.51) and (2.52) are combined and yield the final governing equation for the fluid-structure interaction problem

$$\begin{pmatrix} \mathbf{M}_{ss} & \mathbf{0} & \mathbf{M}_{sc} & \mathbf{0} \\ \mathbf{0} & \mathbf{M}_{ff} & \mathbf{M}_{fc} & \mathbf{0} \\ \mathbf{M}_{cs} & \mathbf{M}_{cf} & \mathbf{M}_{cc} & \mathbf{0} \\ \mathbf{0} & \mathbf{0} & \mathbf{0} & \mathbf{0} \end{pmatrix} \begin{pmatrix} \ddot{\mathbf{U}}_s \\ \ddot{\mathbf{U}}_f \\ \ddot{\mathbf{U}}_c \\ \ddot{\mathbf{P}} \end{pmatrix} + \begin{pmatrix} \mathbf{K}_{ss} & \mathbf{0} & \mathbf{K}_{sc} & \mathbf{0} \\ \mathbf{0} & \mathbf{K}_{ff} & \mathbf{K}_{fc} & \mathbf{K}_{fp} \\ \mathbf{K}_{cs} & \mathbf{K}_{cf} & \mathbf{K}_{cc} & \mathbf{K}_{cp} \\ \mathbf{0} & \mathbf{K}_{pf} & \mathbf{K}_{pc} & \mathbf{K}_{pp} \end{pmatrix} \begin{pmatrix} \mathbf{U}_s \\ \mathbf{U}_f \\ \mathbf{U}_c \\ \mathbf{P} \end{pmatrix} = \begin{pmatrix} \mathbf{R}_s \\ \mathbf{R}_f \\ \mathbf{0} \\ \mathbf{0} \end{pmatrix}, \quad (2.53)$$

with  $\mathbf{M}_{cc} = \mathbf{M}_{cc}^s + \mathbf{M}_{cc}^f$  and  $\mathbf{K}_{cc} = \mathbf{K}_{cc}^s + \mathbf{K}_{cc}^f$ .

Note that due to dynamic matching at the fluid-structure interface, the force  $\mathbf{R}_c^s$  and  $\mathbf{R}_c^f$  cancel each other, which is where the third  $\mathbf{0}$  of the right hand side of the equation come from.

Similarly, implementing the  $\mathbf{u} - p - \Lambda$  formulation for fluid elements and  $\mathbf{u}/p$  formulation for structure elements, the coupled equation can be written as

$$\begin{aligned}
 & \begin{pmatrix} \mathbf{M}_{ss} & \mathbf{0} & \mathbf{M}_{sc} & \mathbf{0} & \mathbf{0} \\ \mathbf{0} & \mathbf{M}_{ff} & \mathbf{M}_{fc} & \mathbf{0} & \mathbf{0} \\ \mathbf{M}_{cs} & \mathbf{M}_{cf} & \mathbf{M}_{cc} & \mathbf{0} & \mathbf{0} \\ \mathbf{0} & \mathbf{0} & \mathbf{0} & \mathbf{0} & \mathbf{0} \\ \mathbf{0} & \mathbf{0} & \mathbf{0} & \mathbf{0} & \mathbf{0} \end{pmatrix} \begin{pmatrix} \ddot{\mathbf{U}}_s \\ \ddot{\mathbf{U}}_f \\ \ddot{\mathbf{U}}_c \\ \ddot{\mathbf{P}} \\ \ddot{\Lambda} \end{pmatrix} \\
 + & \begin{pmatrix} \mathbf{K}_{ss} & \mathbf{0} & \mathbf{K}_{sc} & \mathbf{0} & \mathbf{0} \\ \mathbf{0} & \mathbf{K}_{ff} & \mathbf{K}_{fc} & \mathbf{K}_{fp} & \mathbf{K}_{f\lambda} \\ \mathbf{K}_{cs} & \mathbf{K}_{cf} & \mathbf{K}_{cc} & \mathbf{K}_{cp} & \mathbf{K}_{c\lambda} \\ \mathbf{0} & \mathbf{K}_{pf} & \mathbf{K}_{pc} & \mathbf{K}_{pp} & \mathbf{0} \\ \mathbf{0} & \mathbf{K}_{\lambda f} & \mathbf{K}_{\lambda c} & \mathbf{0} & \mathbf{K}_{\lambda\lambda} \end{pmatrix} \begin{pmatrix} \mathbf{U}_s \\ \mathbf{U}_f \\ \mathbf{U}_c \\ \mathbf{P} \\ \Lambda \end{pmatrix} = \begin{pmatrix} \mathbf{R}_s \\ \mathbf{R}_f \\ \mathbf{0} \\ \mathbf{0} \\ \mathbf{0} \end{pmatrix}, \quad (2.54)
 \end{aligned}$$

with

$$\mathbf{K}_{pp}^p = \begin{pmatrix} \mathbf{K}_{ss}^p & \mathbf{0} & \mathbf{K}_{sc}^p \\ \mathbf{0} & \mathbf{K}_{ff}^p & \mathbf{K}_{fc}^p \\ \mathbf{K}_{cs}^p & \mathbf{K}_{cf}^p & \mathbf{K}_{cc}^p \end{pmatrix} \quad \text{and} \quad \mathbf{P} = \begin{pmatrix} \mathbf{P}_s \\ \mathbf{P}_f \\ \mathbf{P}_c \end{pmatrix}. \quad (2.55)$$

Here, the superscript  $p$  is used in order to distinguish the pressure stiffness entries from the displacement entries. Condensing the entries of displacement unknown, Eq. (2.54) becomes

$$\begin{pmatrix} \mathbf{M}_{uu} & \mathbf{0} & \mathbf{0} \\ \mathbf{0} & \mathbf{0} & \mathbf{0} \\ \mathbf{0} & \mathbf{0} & \mathbf{0} \end{pmatrix} \begin{pmatrix} \ddot{\mathbf{U}} \\ \ddot{\mathbf{P}} \\ \ddot{\Lambda} \end{pmatrix} + \begin{pmatrix} \mathbf{K}_{uu} & \mathbf{K}_{up} & \mathbf{K}_{ul} \\ \mathbf{K}_{pu} & \mathbf{K}_{pp} & \mathbf{0} \\ \mathbf{K}_{lu} & \mathbf{0} & \mathbf{K}_{ll} \end{pmatrix} \begin{pmatrix} \mathbf{U} \\ \mathbf{P} \\ \Lambda \end{pmatrix} = \begin{pmatrix} \mathbf{R} \\ \mathbf{0} \\ \mathbf{0} \end{pmatrix}, \quad (2.56)$$

with  $\mathbf{U} = (\mathbf{U}_s \mathbf{U}_f \mathbf{U}_c)^T$ .

Even though it looks similar as Eq. (2.23), structure elements components are included. Reference [40] provides a more comprehensive explanation for the coupled fluid-structure matrices.

## 2.4 Mixed Element and Interpolation Functions

In order to further the numerical analysis by the finite element method, appropriate mixed elements should be chosen to match the mixed formulation and satisfy the inf-sup condition. It has been proven that  $9-4c-4c$  and  $9-3-3$  mixed elements are appropriate choices [3] in two-dimensional analysis. Chapter 4 includes calculations regarding the numerical inf-sup values *vs.* number of elements, which show that the  $9-4c-4c$  elements for  $\mathbf{u}-p-\Lambda$  formulation pass the inf-sup test. Of course, additional elements can be proposed based on the mixed formulation. For instance, another reasonable element is the  $9-3-1$  element; however, this does not impose the zero vorticity as strongly as  $9-3-3$  element. Fig. 2.1 depicts the element configurations schematically. Take the second one as an example, there are 9 continuous nodal displacements and 4 continuous pressure and vorticity moment nodes in each element. Letter *c* indicates that these quantities are continuous among elements. Due to the linearity,  $9-4c-4c$  elements are implemented for this problem.

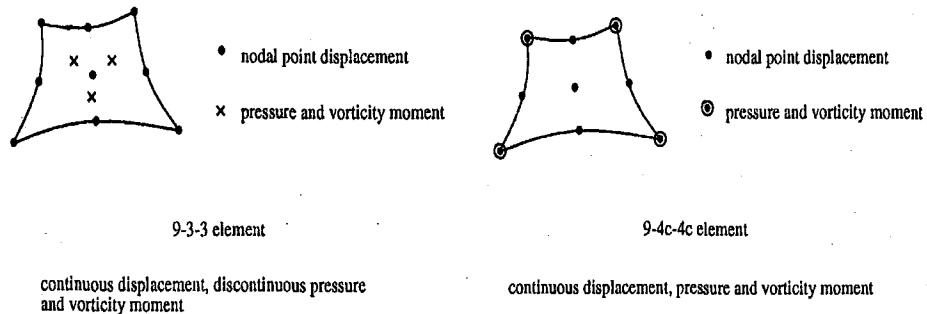


**Figure 2.1** Two mixed elements for  $\mathbf{u}-p-\Lambda$  formulation. Full numerical integration is used (i.e.  $3 \times 3$  Gauss integration).

In the mesh generation figure, it shows that each pressure node, except the nodes on the boundary, is shared by four neighboring elements. Therefore, a bilinear interpolation function

$$p = p_1 + p_2r + p_3s + p_4rs, \quad (2.57)$$

is used to describe the pressure of a generic element, where  $r$  and  $s$  are the natural coordinates for a single element. Comparing Eq. (2.2) with (2.9) in Chapter 2, it can be observed that these two constraints are very similar in nature and are not coupled in the displacement-based formulation. Therefore, it can be assumed that they should be imposed with the same interpolation functions in generic element discretization. That is to say, for the inviscid fluid formulation, the interpolation for the vorticity moment can be built up as

$$\Lambda = \Lambda_1 + \Lambda_2r + \Lambda_3s + \Lambda_4rs. \quad (2.58)$$

With the selected element, the macroelements design of the mathematical models can be constructed. Different numbering of the nodes leads to different matrix patterns. Assuming the diagonal mass matrix with no damping involved in the system, the number of operations for one time step is around  $2nm_k$ , where  $n$  and  $m_k$  are the order and half-bandwidth of the stiffness matrix, respectively. Therefore, in order to achieve more efficient operation, these two parameters should be decreased by numbering the nodal points. Usually, the computer program ADINA is employed to finish part of this work.

## 2.5 Mesh Generation and Stability Analysis

In the following discussion, the stability analysis is based on the  $\mathbf{u}-p-\Lambda$  formulation for acoustic fluid and the  $\mathbf{u}/p$  formulation for structure. The basic observations

and conclusions are also directly applicable to the  $\mathbf{u}/p$  formulation for fluid and displacement-based formulation for structure.

Let

$$\bar{\mathbf{U}}_h = \bar{\mathbf{U}}, \quad \bar{\mathbf{S}}_h = (\bar{\mathbf{P}} \ \bar{\mathbf{\Lambda}})^T$$

$$\mathbf{R}_h = \mathbf{R}, \quad (\mathbf{K}_{us})_h = (\mathbf{K}_{up} \ \mathbf{K}_{ul}), \quad (\mathbf{K}_{ss})_h = \begin{pmatrix} \mathbf{K}_{pp} & \mathbf{0} \\ \mathbf{0} & \mathbf{K}_{ll} \end{pmatrix}$$

Then, Eq. (2.56) is

$$\begin{pmatrix} \mathbf{M}_{uu} & \mathbf{0} \\ \mathbf{0} & \mathbf{0} \end{pmatrix} \begin{pmatrix} \ddot{\bar{\mathbf{U}}}_h \\ \ddot{\bar{\mathbf{S}}}_h \end{pmatrix} + \begin{pmatrix} (\mathbf{K}_{uu})_h & (\mathbf{K}_{us})_h \\ (\mathbf{K}_{us})_h^T & (\mathbf{K}_{ss})_h \end{pmatrix} \begin{pmatrix} \bar{\mathbf{U}}_h \\ \bar{\mathbf{S}}_h \end{pmatrix} = \begin{pmatrix} \mathbf{R}_h \\ \mathbf{0} \end{pmatrix}, \quad (2.59)$$

where  $\bar{\mathbf{U}}_h$  contains all the variables of the nodal point displacements in two directions and  $\bar{\mathbf{S}}_h$  lists all the pressure and vorticity moment unknowns.

In frequency analysis, there must be zero frequencies since the stiffness matrix is invertible. The number of zero frequencies can be exactly calculated by the the dimension of  $(\mathbf{K}_{uu})_h$  and  $(\mathbf{K}_{ss})_h$ . It will be discussed in detail in Chapter 4.

For step-by-step transient analysis, after transforming, the following equation is considered for every time step:

$$\begin{pmatrix} (\mathbf{K}_{uu}^*)_h & (\mathbf{K}_{us})_h \\ (\mathbf{K}_{us})_h^T & (\mathbf{K}_{ss})_h \end{pmatrix} \begin{pmatrix} \bar{\mathbf{U}}_h \\ \bar{\mathbf{S}}_h \end{pmatrix} = \begin{pmatrix} \mathbf{R}_h^* \\ \mathbf{0} \end{pmatrix}, \quad (2.60)$$

where  $\mathbf{R}_h^*$  is an effective load vector. Moreover, it is known that the shear modulus  $G = 0$  for inviscid fluid, therefore,

$$(\mathbf{K}_{uu}^*)_h = C(\mathbf{M}_{uu})_h, \quad (2.61)$$

where  $C$  is a constant depending on the time integration method (for example,  $C = \frac{1}{\alpha \Delta t^2}$  with  $\alpha \geq 0.25$  for Newmark method). Since  $(\mathbf{M}_{uu})_h$  is positive definite,  $(\mathbf{K}_{uu}^*)_h$  is always a positive-definite matrix.

The stability and effectiveness of the  $\mathbf{u}/p$ ,  $\mathbf{u}-p-\Lambda$  formulation and corresponding mixed elements which will be employed in the test problems are verified through ellipticity and inf-sup conditions, which are necessary and sufficient conditions for well-posedness.

(a) Ellipticity Condition:

$$\bar{\mathbf{V}}_h^T (\mathbf{K}_{uu})_h^* \bar{\mathbf{V}}_h \geq c_1 \|\bar{\mathbf{V}}_h\|_V^2 \quad \text{for all } \bar{\mathbf{V}}_h \in \ker[(\mathbf{K}_{us})_h^T], \quad (2.62)$$

where  $c_1 > 0$ ,  $\|v\|_V^2 = \sum_{i,j} \|\frac{\partial v_i}{\partial x_j}\|_{L^2(Vol)}^2$  and

$$\ker[(\mathbf{K}_{us})_h^T] = \{\bar{\mathbf{V}}_h | \bar{\mathbf{V}}_h \in R^n, (\mathbf{K}_{us})_h^T \bar{\mathbf{V}}_h = 0\}.$$

(b) Inf-Sup Condition:

$$\inf_{\bar{\mathbf{s}}_h} \sup_{\bar{\mathbf{u}}_h} \frac{\bar{\mathbf{U}}_h^T (\mathbf{K}_{us})_h \bar{\mathbf{S}}_h}{\|\bar{\mathbf{U}}_h\| \|\bar{\mathbf{S}}_h\|} \geq c_2 > 0, \quad (2.63)$$

where the constant  $c$  is independent of the mesh size  $h$ , the constant  $\alpha$  in the irrotationality constraint and the bulk modulus  $\beta$ .

Generally, whether the inf-sup condition is satisfied depends on the specific finite element, the boundary condition and the macromesh generation of the mathematical models. The inf-sup condition was popularized by Babuska in 1972 and stated in an earlier theoretical work by Necas in 1962. Reference [15] introduces this condition from the viewpoint of Banach space theorems. Reference [3] gives the numerical proof of inf-sup condition derived from the matrix equations.

Although the inf-sup condition for mixed formulations was proposed some time ago, the analytical proof of whether the inf-sup condition is satisfied by a specific element can be very difficult. Reference [8] gives a numerical test in practice.

## CHAPTER 3

### NUMERICAL PROCEDURES

#### 3.1 Free Surface, Interface and Other Boundaries

The benefit of using primitive variable formulation is the direct coupling of fluid and solid domains in element assemblage procedures. No other interaction conditions need to be considered. Moreover, due to the elasticity and continuity of the fluid, shear stress is omitted. There are several points worth mentioning before the numerical analysis is proceed.

For both of the fluid-structure interaction models shown in Chapter 4, the top is a free surface and the other three sides are fixed walls. Assume the density and bulk modulus of the fluid are very similar to those of water. Therefore, the gravity force can be considered as the dominant force of the free surface and surface tension effects can be neglected. In this way, the Bond number, which is a measure of the importance of surface tension forces compared to body forces, is relatively large. One of the three modes need focus on in the FSI model is the fluid sloshing mode, which is subject to Earth's gravity. From the numerical results in next section, it can be clearly concluded that the sloshing frequencies are far below structural resonance frequencies and acoustic frequencies.

For most of the displacement nodal points, such as the nodes on the free surface, there are two degrees of freedom. The tangential and normal direction can be considered as the the natural coordinates for the whole system. As for the boundary conditions of the other three sides, some degrees of freedom can be eliminated. For example, the two corner nodes at the bottom and three nodes to the left of the structure in the first model (Fig. 4.10) lost both of two degrees of freedom. The nodes on the walls (Dirichlet boundaries) other than the five mentioned above lost

only one degree of freedom (in the normal direction). They satisfy the following boundary condition:

$$\mathbf{v} \cdot \mathbf{n} = 0 \quad \text{on } S_u, \quad (3.1)$$

where  $\mathbf{v}$  is the fluid velocity and  $\mathbf{n}$  is the outward normal vector.

The question of how to deal with the boundary conditions on the wetted surface, which is the interface between fluid and structure, is among the most important sticking points for fluid-structure interaction problems. In the test problems, the fluid density is assumed to be sufficiently high, such that the effects of coupling between the fluid and structure become important. The slip boundary conditions are assumed such that the requirements of mass and momentum conservation on the wetted surface are satisfied. It is also assumed that there is no transport of fluid across the wetted surface. The method implemented here is to simulate the deflection of the structure nodes on the wetted surface, which are called master nodes. The corresponding nodes in the fluid elements are named slave nodes. During the calculation, one degree of freedom (in normal direction) of slave nodes in the matrix and vector assemblage is eliminated and the slave nodes is given the quantities of their corresponding master nodes in the normal direction on the fluid structure interface. That is to say, the inviscid flow satisfies the following condition

$$\mathbf{v}^s \cdot \mathbf{n} = \mathbf{v}^f \cdot \mathbf{n} \quad \text{on } S_c, \quad (3.2)$$

where  $\mathbf{v}^s$  and  $\mathbf{v}^f$  are the velocity of the solid and fluid nodal points respectively and  $S_c$  indicates the wetted surface.

For any mathematical model with finite element discretization, there are two groups of coordinates natural coordinates  $(r, s)$  for generic element and global coordinates  $(U, V)$ / local coordinates  $(u, v)$  for general macromesh. Since the system is two-dimensional, the tangential and normal directions of a generic node are assumed

to be its two natural coordinate directions. In this way, the global/local coordinates of most nodal points in the system are the same as natural coordinates, except for several nodes, such as the four corner points of the structure. Since the boundary is fixed, it is assumed that the wave reaching the corners only has tangential direction. Assuming  $r$  is the tangential direction and  $s$  the normal direction, a rotation (transformation) of their natural coordinates is necessary prior to the assemblage of the stiff matrix. That is why it is called a skew system.

Based on the components of the mass matrix, pressure and vorticity unknowns can be statically condensed out. Eq. (2.56) is equivalent to the following equation only with respect to the displacement unknown  $\mathbf{U}$

$$\mathbf{M}_{uu} \ddot{\mathbf{U}} + \left\{ \mathbf{K}_{uu} - \begin{pmatrix} \mathbf{K}_{up} & \mathbf{K}_{ul} \end{pmatrix} \begin{pmatrix} \mathbf{K}_{pp} & 0 \\ 0 & \mathbf{K}_{ll} \end{pmatrix}^{-1} \begin{pmatrix} \mathbf{K}_{pu} \\ \mathbf{K}_{lu} \end{pmatrix} \right\} \mathbf{U} = \mathbf{R}(t). \quad (3.3)$$

Simplifying the matrix multiplication, the following equation can be observed

$$\mathbf{M} \ddot{\mathbf{U}} + \mathbf{K} \mathbf{U} = \mathbf{R}(t), \quad (3.4)$$

with

$$\mathbf{M} = \mathbf{M}_{uu}$$

and

$$\mathbf{K} = \mathbf{K}_{uu} - \begin{pmatrix} \mathbf{K}_{up} & \mathbf{K}_{ul} \end{pmatrix} \begin{pmatrix} \mathbf{K}_{pp} & 0 \\ 0 & \mathbf{K}_{ll} \end{pmatrix}^{-1} \begin{pmatrix} \mathbf{K}_{pu} \\ \mathbf{K}_{lu} \end{pmatrix}.$$

### 3.2 Modal Analysis

Assume the exterior force  $\mathbf{R}$  is zero and the equation above turns out to be a homogeneous equation while the problem turns out to be a steady-state problem. The natural frequencies can be found by solving a general eigenvalue problem:

$$\mathbf{K} \boldsymbol{\phi} = \omega^2 \mathbf{M} \boldsymbol{\phi}, \quad (3.5)$$

where  $\mathbf{M}\phi$  corresponds to the strain energy and  $\mathbf{K}\phi$  to the kinetic energy. It then becomes necessary to investigate the physical stability of the system under consideration. That is to say, assuming that the steady-state solution of the system is known, is there another solution into which the system could bifurcate if it were slightly disturbed from its equilibrium position? The answer is yes. Since a main characteristic of the eigenvalue problem is the non-uniqueness of the solution, varies of eigenvalues, i.e., natural frequencies  $\omega$  can be achieved.

In addition, the number of zero frequencies can be predicted by the degrees of freedom of fluid elements. Assuming that there are  $n$  displacement unknowns,  $m$  pressure (and vorticity moment) unknowns, and  $k$  free surface nodes, then the number of zero frequencies can be obtained base on the following formula:

$$\text{Number of zero frequency} = n - m - (k - 1). \quad (3.6)$$

Here, assuming the physical constant pressure mode arising with the boundary condition

$$\mathbf{v} \cdot \mathbf{n} = 0 \quad \text{on } S,$$

has been eliminated.

### 3.3 Transient Analysis

Consider the problem described by Eq. (3.4) with  $\mathbf{R}(t)$  a vector of time-dependent nodal forces. For this case, the time effect on the element equilibrium relations is negligible but the load vector  $\mathbf{R}(t)$  is a function of time. Since such an analysis is in essence still a steady-state analysis, but with steady-state conditions considered at any time  $t$ , the analysis may be referred to as a pseudo steady-state analysis.

If Newmark method (Appendix A) is implemented, the displacement unknowns can be calculated iteratively as well as the pressure and vorticity variables. Notice that full numerical integration is employed for all elements.

### 3.4 Model Reduction Method

Since the finite element procedure is realized on the basis of elements, a large number of elements and the degrees of freedom may lead to high-dimensional material matrices. In this way, the problem of simulation and modelling turns to developing efficient methods to create low-dimensional dynamic descriptions which can capture most of the accuracy of the fully meshed FEM model. Therefore, two different model reduction methods are introduced, mode superposition method and singular value decomposition based model reduction methods, e.g., singular value decomposition and principal component analysis.

#### 3.4.1 Mode Superposition Method

In numerical analysis, the number of operations required is directly proportional to the half-bandwidth of the stiffness matrix. Therefore, the reduction of bandwidth will decrease proportionally the cost of iterative solutions. This is why the nodal point numbering should be rearranged properly. However, there is a minimum bandwidth obtained by this method. Therefore, a different procedure, mode superposition method is introduced [3],[13].

Suppose the equilibrium equation with damping neglected is built up as

$$\mathbf{M}\ddot{\mathbf{X}} + \mathbf{K}\mathbf{X} = \mathbf{R}(t). \quad (3.7)$$

We propose to transform this equation into a more effective form for direct integration by using the following transformation

$$\mathbf{X}(t) = \mathbf{P}\mathbf{U}(t), \quad (3.8)$$

where  $\mathbf{P}$  is a square modal matrix and  $\mathbf{U}$  is a time-dependent general coordinate vector.

Substituting Eq. (3.8) into (3.7) and premultiply the result by  $\mathbf{P}^T$ , the equation can be derived as

$$\tilde{\mathbf{M}}\ddot{\mathbf{U}} + \tilde{\mathbf{K}}\mathbf{U} = \tilde{\mathbf{R}}(t) \quad (3.9)$$

with  $\tilde{\mathbf{M}} = \mathbf{P}^T\mathbf{M}\mathbf{P}$ ,  $\tilde{\mathbf{K}} = \mathbf{P}^T\mathbf{K}\mathbf{P}$  and  $\tilde{\mathbf{R}} = \mathbf{P}^T\mathbf{R}$ .

Theoretically, there are various of transformation matrix  $\mathbf{P}$  which can reduce the bandwidth of the matrices. An effective transformation matrix is established by solving the free-vibration equilibrium equation, i.e.,

$$\mathbf{M}\ddot{\mathbf{U}} + \mathbf{K}\mathbf{U} = \mathbf{0}. \quad (3.10)$$

The solution of Eq. (3.10) can be written as

$$\mathbf{U}(t) = \mathbf{P}_i \sin \omega_i(t - t_i), \quad (3.11)$$

where  $\mathbf{P}_i$  is the eigenvector satisfying the  $\mathbf{M}$  orthonormalized condition  $\phi_i^T \mathbf{M} \phi_j = \delta_{ij}$ , and  $\omega_i$  and  $t_i$  indicate the corresponding eigenvalue and time constant related to the initial conditions.

Substituting Eq. (3.11) into (3.10), the generalized eigen problem can be built up

$$\mathbf{K}\mathbf{P}_i = \omega_i^2 \mathbf{M}\mathbf{P}_i. \quad (3.12)$$

Therefore, the transformation matrix can be finally defined as  $\mathbf{P} = [\mathbf{P}_1, \mathbf{P}_2, \dots, \mathbf{P}_n]$  and  $\mathbf{\Lambda} = \text{diag}\{\omega_1^2, \omega_2^2, \dots, \omega_n^2\}$ . Introduce these notations, Eq. (3.12) can be written as

$$\mathbf{K}\mathbf{P} = \mathbf{M}\mathbf{P}\mathbf{\Lambda} \quad (3.13)$$

with  $\mathbf{P}^T\mathbf{K}\mathbf{P} = \mathbf{\Lambda}$  and  $\mathbf{P}^T\mathbf{M}\mathbf{P} = \mathbf{I}$ .

### 3.4.2 Singular Value Decomposition and Principal Component Analysis

Both singular value decomposition and principal component analysis are powerful techniques for extracting the structure of data from high-dimensional data sets and representing by low-dimensional approximations. SVD and PCA are widely used in data reduction, image compression and feature extraction. Consider an  $m \times n$  matrix  $\mathbf{A}$ . Two symmetric matrices  $\mathbf{A}^T\mathbf{A}$  and  $\mathbf{A}\mathbf{A}^T$  can be easily constructed. Supposing the rank of the matrix  $\mathbf{A}$  is  $r$ , there will be  $r$  non-zero eigenvalues of these two symmetric matrices. In fact, these  $r$  eigenvalues are positive. However, while it can be shown that the positive eigenvalues of the  $n \times n$  matrix  $\mathbf{A}^T\mathbf{A}$  are the same as those of the  $m \times m$  matrix  $\mathbf{A}\mathbf{A}^T$ , the number of zero eigenvalues will be different. For the symmetric matrix  $\mathbf{A}^T\mathbf{A}$ , the dimension of the null space will be  $n - r$ , which means there are  $n - r$  null space vectors. It can be easily shown that these  $n - r$  null space vectors of the matrix  $\mathbf{A}^T\mathbf{A}$  are also the null space vectors of the matrix  $\mathbf{A}$ . Likewise, there will be  $m - r$  null space vectors of the matrix  $\mathbf{A}\mathbf{A}^T$  and they are the same as the left null space vector of the matrix  $\mathbf{A}$ .

Based on the linear algebra theories, the orthogonal subspace of the null space must be the row space while the orthogonal subspace of the left null space is the column space. As a consequence, the eigenvectors of the matrix  $\mathbf{A}^T\mathbf{A}$  denoted as  $\mathbf{v}_i$  span the row space of the matrix  $\mathbf{A}$  and the eigenvectors of the matrix  $\mathbf{A}\mathbf{A}^T$  represented with  $\mathbf{u}_i$  construct the column space of the matrix  $\mathbf{A}$ . In fact,  $\mathbf{u}_i$  and  $\mathbf{v}_i$  are similar to the right and left eigenvectors of the square matrix.

Denote a matrix  $\mathbf{U}$ , the first  $r$  columns of which are the eigenvectors of the symmetric matrix  $\mathbf{A}\mathbf{A}^T$ , and the last  $m - r$  columns are constructed with the left null space vectors. In addition, introduce a matrix  $\mathbf{V}$ , the first  $r$  columns of which are the eigenvectors of the symmetric matrix  $\mathbf{A}^T\mathbf{A}$ , and the last  $n - r$  columns are made of the null space vectors. The singular value decomposition of the matrix  $\mathbf{A}$  is

then depicted as

$$\mathbf{A} = \mathbf{U}\mathbf{\Sigma}\mathbf{V}^T = \sum_{i=1}^r \sigma_i \mathbf{A}_i, \quad (3.14)$$

where  $\mathbf{A}_i = \mathbf{u}_i \mathbf{v}_i$  are the basis matrices.  $r$  diagonal entities  $\sigma_i$  of the  $m \times n$  matrix  $\mathbf{\Sigma}$  are the square root of the non-zero eigenvalues of the matrix  $\mathbf{A}^T \mathbf{A}$  or  $\mathbf{A} \mathbf{A}^T$  or the singular values of the matrix  $\mathbf{A}$  (the weight of the basis matrices). Singular values can help identify the most important basis matrices. The column of  $\mathbf{U}$  contains the left singular vectors and the row of  $\mathbf{V}^T$  contain the elements of the right singular vectors, also called the coefficients. Each row of  $\mathbf{U}\mathbf{\Sigma}$  is called the score of the coefficient. By picking up the singular vectors having the largest singular values, as little information as possible is lost in the mean-square sense (Appendix C).

Suppose the Wiener process is also considered in the FSI system. If SVD is implemented and only the first few dominant components are kept, the noise with small variance can be reduced significantly. That is because the signal is well represented by the first few terms, but noise is typically spread out over all the terms. That is to say, most of the signal is maintained but most of the noise with small variance is eliminated.

Another efficient procedure based on singular value decomposition is called principal component analysis. As a linear combination of all state variables, for instance, nodal unknowns in finite element analysis, the general coordinate  $\xi(t)$  can be introduced as

$$\xi(t) = \sum_{i=1}^m \phi_i x_i(t) = \boldsymbol{\phi}^T \mathbf{x}(t), \quad (3.15)$$

where  $m$  represents the total number of channels or state variables and  $x_i(t)$  is the  $i$ -th time dependent variable.

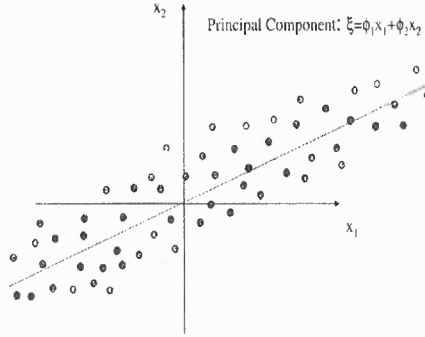


Figure 3.1 Illustration of principal component.

If the variance of  $\xi(t)$  within the time interval  $[t_0, t_1]$  is maximized, the data spread primarily in this general direction. Consequently, the direction is represented as a linear combination of all state variables will be called the principal direction as illustrated in Fig. 3.1. Of course, it is anticipated that the total number of principal directions  $r$  should be much smaller than the spatial dimension  $m$ . Denoting the time averaged value  $\bar{\xi}$  as  $\int_{t_0}^{t_1} \xi(t) dt / (t_1 - t_0)$ , the variance of  $\xi(t)$  can be expressed as

$$\int_{t_0}^{t_1} (\xi(t) - \bar{\xi})^2 dt.$$

Instead of dealing with infinite dimensional problems in the time domain, it is often more practical to use the temporal discretization. For example, let us have  $n$  time snapshots within the time interval  $[t_0, t_1]$ . For a typical channel  $k$ , denote  $\bar{x}_k = \frac{1}{n} \sum_{j=1}^n x_{kj}$ , the variance of this channel can be expressed as  $\frac{1}{n} \sum_{j=1}^n (x_{kj} - \bar{x}_k)^2$ . Consequently, the variance based on the general coordinate  $\boldsymbol{\xi}$  in equation (3.15) can be expressed as  $\frac{1}{n} \sum_{j=1}^n (\xi_j - \bar{\xi})^2$ , where the mean value of  $\boldsymbol{\xi}$  is defined as  $\bar{\xi} = \frac{1}{n} \sum_{j=1}^n \xi_j$ .

The procedure to maximize the variance  $\boldsymbol{\xi}$  in  $R^n$  leads to an optimization problem: find  $\boldsymbol{\phi} \in R^m$  such that  $\boldsymbol{\phi}^T (\mathbf{x}_k - \bar{x}_k) (\mathbf{x}_k - \bar{x}_k)^T \boldsymbol{\phi}$ , is maximized subject to the constraint  $\boldsymbol{\phi}^T \boldsymbol{\phi} = 1$ . It is then clear that the principal component  $\boldsymbol{\phi}$  is in fact the eigenvector of the covariance matrix  $\mathbf{C} = \frac{1}{m-1} (\mathbf{x}_k - \bar{x}_k) (\mathbf{x}_k - \bar{x}_k)^T$ , and the number of principal components  $r$  depends on the rank of the covariant matrix  $\mathbf{C}$ . The eigenvalues, which are also called principal values, represent the variances

of each principal component. Then the singular values are sorted in descending order. Likewise, rearranging the eigenvectors (principal components). In this way, the directions in which the data set has the most significant amounts of energy can be found. Assume the first  $l$  principal components are selected, a  $m \times l$  matrix  $\mathbf{F} = [\phi_1, \phi_2, \dots, \phi_l]$  can be built up. This matrix is called feature vectors. Using the feature vectors, the projected data set can be obtained by  $\mathbf{F}^T \mathbf{x}$ .

Principal component analysis involves a procedure that transforms a number of correlated variables into a smaller number of uncorrelated variables, i.e., principal components. The objective of PCA is to discover and reduce the dimensionality of the data in a way which best explains the variance in the data. Besides, it provides the most efficient way of capturing the dominant components of many process with only few instead. Another method closely related to PCA and SVD is called proper orthogonal decomposition (POD) or Karhunen-Loève decomposition (KLD). Reference [31] provides the mathematical proof of the equivalence of three methods.

### 3.5 Ito Process and Brownian Motion

As mentioned in Chapter 1, it is assumed that each fluid nodal point undergoes a random displacement in a 2-dimensional space at each time step. Similar as the deterministic nodal displacements, the random displacements are decomposed in two directions in the FSI model.

In order to understand the effect of Brownian motion, the 1-dimensional Ito process  $X = \{X_t, t_0 \leq t \leq T\}$  satisfying the stochastic differential equation (SDE) [28] is introduced as

$$dX_t = -a(t, X_t)dt + b(t, X_t)dW_t, \quad (3.16)$$

with the initial value  $X_{t_0} = X_0$  is assumed. Likewise, the vector stochastic differential equation can be obtained by changing the scalar variable to vector variables.

Assuming the drift  $a(t, X_t) = aX_t$  and diffusion coefficient  $b(t, X_t) = b$ , the Ito process  $X_t$  satisfies Langevin equation

$$\frac{dX_t}{dt} = -aX_t + bV_t, \quad (3.17)$$

where  $V_t$  is a white noise process.

It is also can be written as a stochastic integral equation

$$X_t = X_0 - \int_0^t aX_s ds + \int_0^t b dW_s, \quad (3.18)$$

where  $dW_t = V_t dt$ ,  $W_t$  is the Brownian motion and the second integral is an Ito stochastic integral. This process is also called *Ornstein-Uhlenbeck* process. It is clear that the noise term does not depend on the state variable, so the equation has additive noise.

Therefore, the explicit solution of Eq. (3.18) is

$$X_t = e^{-at} \left( X_0 + \int_0^t e^{as} b dW_s \right) \quad (3.19)$$

$$= e^{-at} X_0 + bW_t - e^{-at} \int_0^t a e^{as} b W_s ds, \quad (3.20)$$

for  $t \in [t_0, T]$  and the given Wiener process  $W = \{W_t, t \geq 0\}$ .

To simulate this SDE with implicit Euler approximation, starting from the initial value  $Y_0 = X_0$ , and proceeding recursively to generate the next value

$$Y_{n+1} = Y_n - aY_{n+1}\Delta_n + b\Delta W_n, \quad (3.21)$$

for  $n = 0, 1, 2, \dots$ , where  $\Delta W_n = W_{t_{n+1}} - W_{t_n}$  is the  $N(0; \Delta_n)$  distributed Gaussian increment of Wiener process  $W$  in the subinterval  $t_n \leq t \leq t_{n+1}$ . Here, the equidistant discretization times, ie,  $t_n = t_0 + n\Delta_n$  is employed and the implicit Euler approximation is chosen in terms of the stability issue [38]. As soon as the time step  $\Delta_n$  satisfies the inequality  $|I + a\Delta_n|^{-1} \leq 1$ , the stochastic scheme is A-stable. Of course, an A-stable stochastic scheme is also A-stable in the deterministic sense [28].

In order to describe how to employ this method, a realistic problem, which depicts a mass immersed into fluid is considered. The mass is suspended vertically by a soft spring affixed to a rigid wall. In this model, the effect of vertical Brownian motion on the oscillation of the mass is considered. Therefore, an SDE can be built up to describe the mass motion:

$$m\ddot{x} + kx = V(t). \quad (3.22)$$

Let  $y = \dot{x}$  and rewrite the above SDE, the equation above can be rewritten as

$$\begin{pmatrix} \dot{x} \\ \dot{y} \end{pmatrix} = - \begin{pmatrix} 0 & -1 \\ k/m & 0 \end{pmatrix} \begin{pmatrix} x \\ y \end{pmatrix} + \begin{pmatrix} 0 \\ 1/m \end{pmatrix} V(t). \quad (3.23)$$

Assuming  $\mathbf{X} = \begin{pmatrix} x \\ y \end{pmatrix}$ ,  $\mathbf{a} = \begin{pmatrix} 0 & -1 \\ k/m & 0 \end{pmatrix}$ ,  $\mathbf{b} = \begin{pmatrix} 0 \\ 1/m \end{pmatrix}$ , the stochastic differential equation as above can be derived as

$$d\mathbf{X} = -\mathbf{a}\mathbf{X}dt + \mathbf{b}d\mathbf{W}(t). \quad (3.24)$$

The results of explicit solution, numerical simulation, and confidence intervals are shown in Appendix B.

## CHAPTER 4

### NUMERICAL EXAMPLES

For the mathematical models considered in this Chapter, working in  $R^2$  is not restrictive. Therefore, only two-dimensional solutions are considered and the application can be directly extended to three dimensions.

To demonstrate the capabilities of proposed formulations for both fluid and structure, the numerical results of two typical acoustoelastic problems are presented, which involve acoustic fluids and their interaction with elastic structures.

#### 4.1 Flexible Square Solid Vibrations in Acoustic Fluid

The first model is a typical fluid-structure interaction system as shown in Fig. 4.1. It depicts a square immersed deformable solid in an open square cavity, which is connected to the bottom of the cavity with two springs. The meshes used in the analysis have been derived by starting with coarse meshes and subdividing in each refinement each element into four elements. All the elements employed are  $9 - 4c - 4c$  elements. As mentioned in Chapter 3, the software ADINA is used to generate the macromesh of the mathematical model. Fig. 4.2 shows the workspace of the mesh generation of pressure nodes when the model is divided into 32 fluid elements and 4 structure elements.

Table 4.1 lists the first few frequencies of sloshing /structure /acoustic modes based on different formulations and different mesh density. As for the number of zero frequency, take the 9-elements case as an example, after condensation,  $n = 67$ ,  $m = 32$ , and  $k = 7$  and therefore the prediction is  $67 - 32 - (7 - 1) = 29$  according to Eq. (3.6). However, the numerical result shows that there are 31 zero frequencies. Compared to the theoretical number of zero frequencies for the numerical results, there is a slight difference with 2. That is because the number of free surface nodes

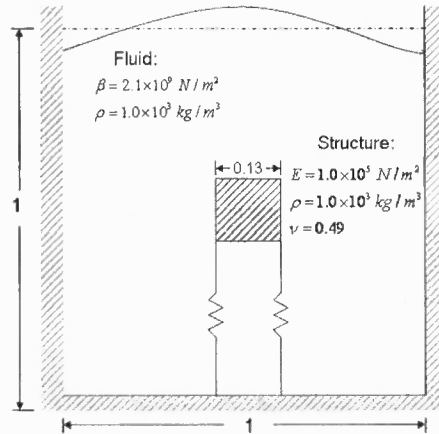


Figure 4.1 Model I: Square solid vibrations in acoustic fluid.

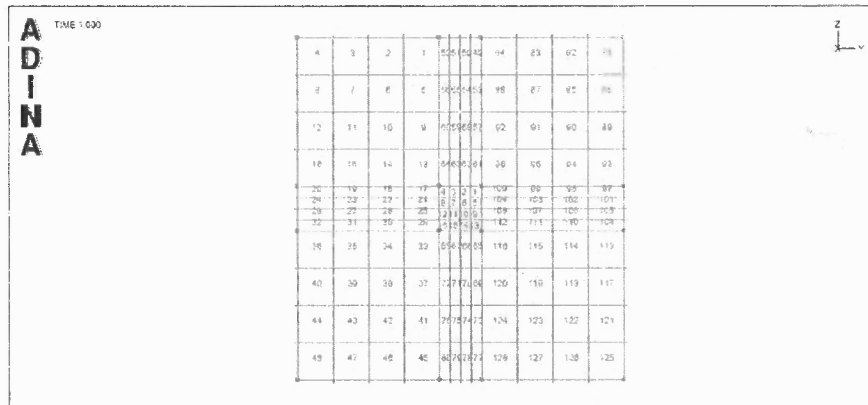


Figure 4.2 Macromesh generation figure by ADINA.

no more need to subtract 1, since the immersed solid will provide some stiffness to balance the constant pressure, which results in one constant pressure mode with zero frequency. Furthermore, 2 translational and one rotational degrees of freedom need to be added to the solid on the basis of the result from Eq. (3.6).

**Table 4.1** Frequencies of Sloshing/Structural/Acoustic Modes of FSI Model I

Formulation Fluid Structure	Eigenmode	Number of elements	Number of zero		Frequencies (rad/s)			
			Theory	Result	First	Second	Third	Fourth
$\mathbf{u} - p - \Lambda \quad \mathbf{u}$	Sloshing	9	31	31	1.6742	5.6735	7.7958	10.027
	Structure				127.72	156.75	276.62	281.72
	Acoustic				10228	12939	14644	14886
$\mathbf{u} - p - \Lambda \quad \mathbf{u}$	Sloshing	36	159	159	1.7952	5.5529	7.9521	10.099
	Structure				115.43	130.39	140.16	156.83
	Acoustic				10327	11930	12695	13523
$\mathbf{u} - p - \Lambda \quad \mathbf{u}$	Sloshing	144	703	703	1.7843	5.5405	7.8638	9.6822
	Structure				86.456	99.892	99.969	121.25
	Acoustic				10160	10164	10174	10267
$\mathbf{u} - p - \Lambda \quad \mathbf{u}/p$	Sloshing	36	159	159	1.8029	5.5529	7.9523	10.099
	Structure				64.306	73.208	85.608	94.529
	Acoustic				10430	12120	12725	13942
$\mathbf{u} - p - \Lambda \quad \mathbf{u}/p$	Sloshing	144	703	703	1.7925	5.5405	7.8640	9.6822
	Structure				107.11	114.25	122.10	130.74
	Acoustic				10161	10296	10304	10670

The numerical results show that the mixed finite element formulations can capture the characteristic of eigenmodes not only for fluid but also the solid. Fig. 4.3 describes the first four structural modes in addition to the first two sloshing and acoustic modes. The upward direction is defined as positive. The top two sub-figures shows the sloshing modes, which describe the fluid motion on the free surface. Therefore, the surface displacements are involved and the free surface is no longer flat. In the first sloshing mode, it can be observed that the right side of the free surface moves upward while the left side goes down; while in the figure showing the second sloshing mode, the middle of the free surface is higher than both sides, which indicates the displacement distribution on the free surface. It is also can be seen that there is no fluid motion around the solid and at the bottom of the cavity. The next four sub-figures are structural modes, which are the characterization of the structure. Based on the configurations, it can be recognized that the first and fourth structural modes are flexural modes; the second one is a stretching mode and the third is a shear mode, which leads to the volume change of the structure. Except the second structural mode, the other three belongs to rotational modes. Due to the corresponding frequencies are non-zero, there is no rigid body mode. Rigid body modes mean the element must be able to undergo as a rigid body without stresses being developed in it. The last two sub-figures are acoustic modes, which focus on the interior of the fluid. In such figures, the fluid motion is captured, even the free surface, as shown in the second acoustic mode. From this figure and figures after, it also can be seen that the compatibility is satisfied, since the displacements within the elements and across the element boundaries are continuous.

Fig. 4.4 describes the first two pressure band plots of three kinds of eigenmodes. Different from displacement modes, there is no change of the configurations of the model. However, the mode shapes still can be recognized based on the pressure distribution. For example, it can be seen that pressure on the right side of the

free surface is higher than that on the left side in the figure of the first sloshing mode. Therefore, it can be deduced that the nodes on the right side have positive displacements. Likewise, the nodal points in the middle of the surface in the second sloshing mode must have positive displacements since they undergo high pressure. In the next two sub-figures, the pressure around the structure is considered. Similar as the displacement mode shapes can be deduced by the pressure on the boundary of the solid. If the pressure on the bottom of solid is higher than that on the top side, the solid will be pushed upward. At the same time, the fluid provides some impedance to the solid, which can balance part of the pressure. Therefore, the solid is squeezed to both right and left sides, as shown in the second structural mode. Acoustic pressure modes belong to high-frequency modes. The complexity makes them not so easy to understand as sloshing and structural modes. For example, the last two sub-figures are the mode shapes in pressure with two minimal acoustic frequencies. However, they display quite different patterns.

Then each element is divided into four subelements. Therefore, both the number of elements and the degrees of freedom of the system are changed. Likewise, the eigenmodes of pressure are plotted in Fig. 4.5. It is known that any displacement and pressure pattern is a linear combination of the eigenmodes. Compare the structural modes in Fig. 4.4 and 4.5, it can be concluded that the eigenmodes show more simple pattern if more elements are employed to discretize the FSI model. Table 4.1 shows the same phenomenon but in terms of natural frequencies. Take the second and third rows as an example. The result shows that two more hiding structure frequencies  $130.19 \text{ rad/s}$   $140.16 \text{ rad/s}$  on the third row can be found between the first two frequencies when 9 elements is used (on the second row).

As with the stability issue referred in Chapter 3, the mixed formulation should satisfy the ellipticity and inf-sup condition. The ellipticity condition is easy to obtain, since  $(\mathbf{K}_{uu}^*)_h$  is always a positive-definite matrix based on the relationship

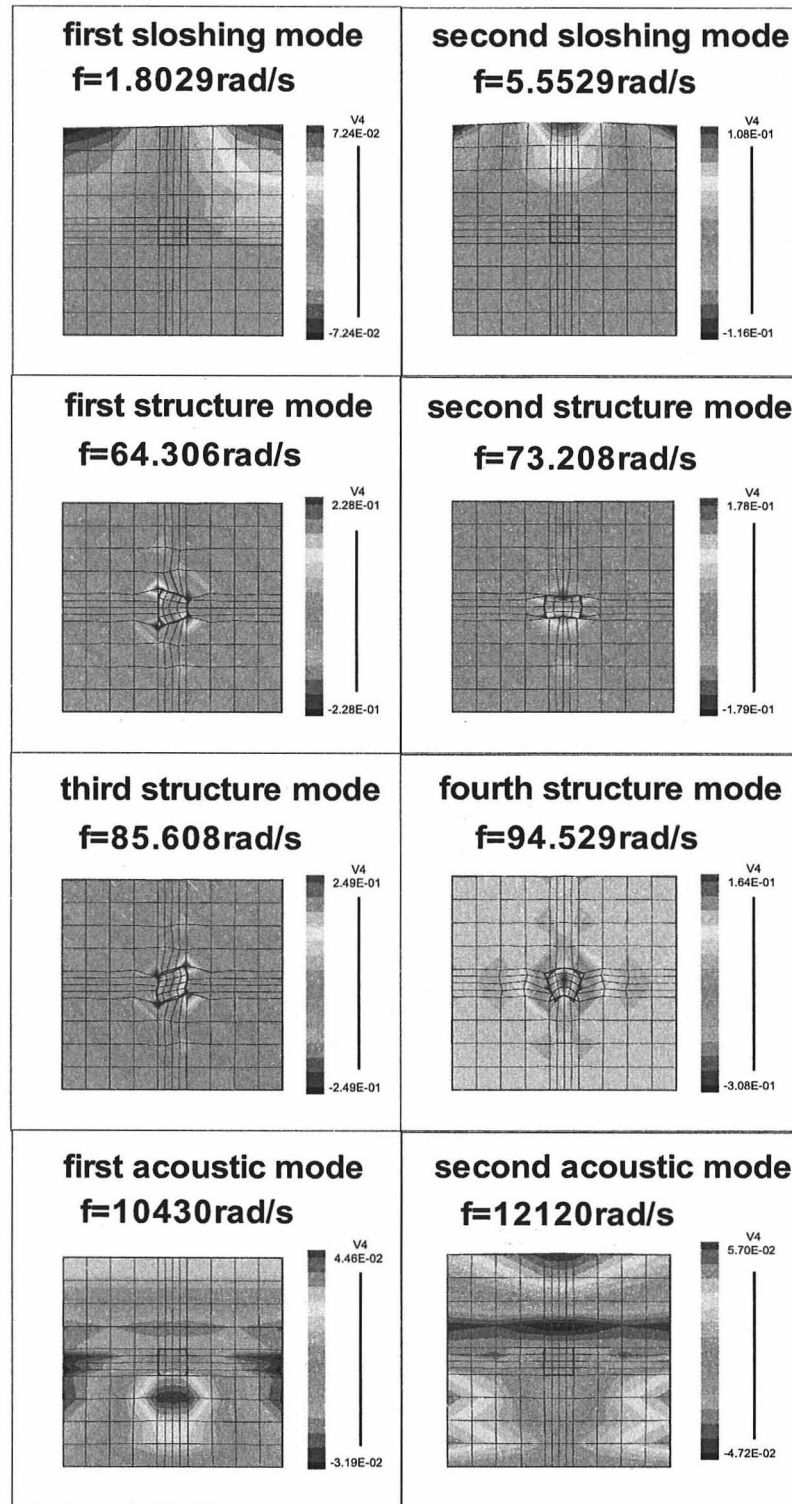
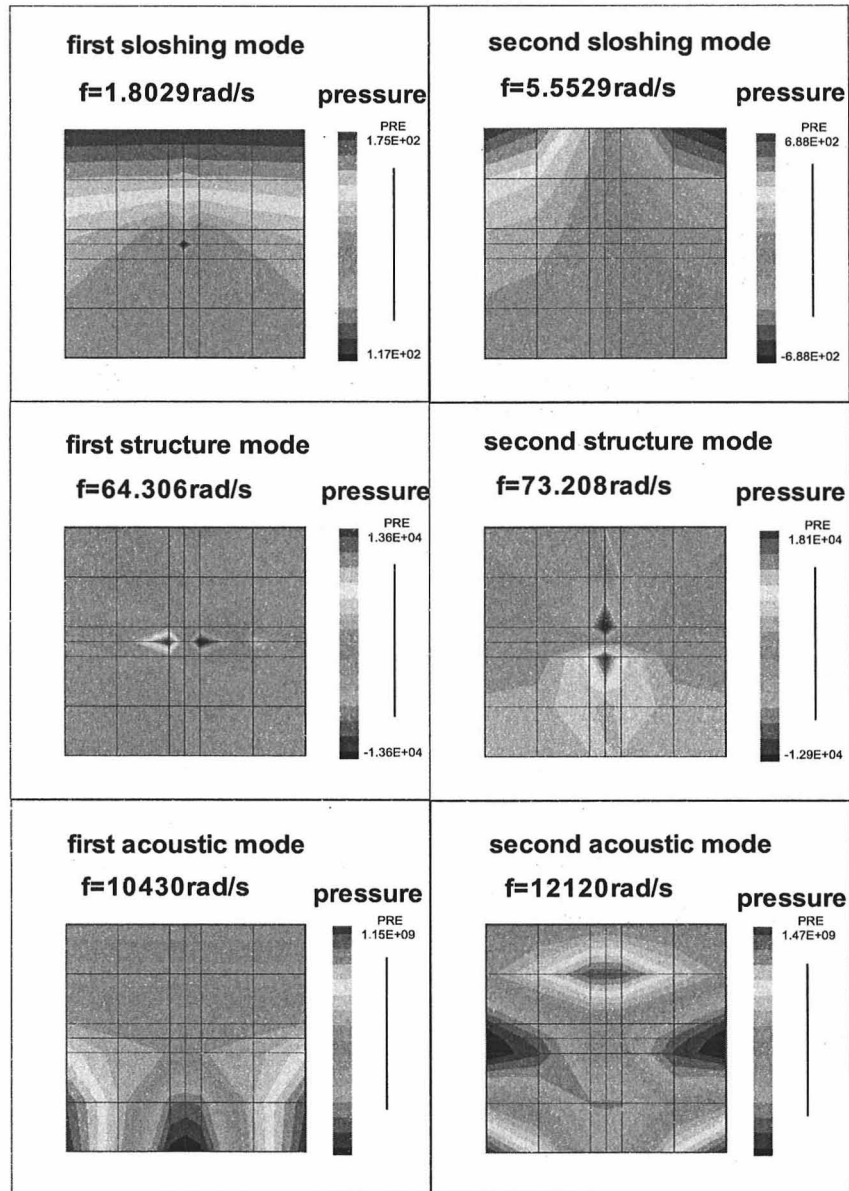
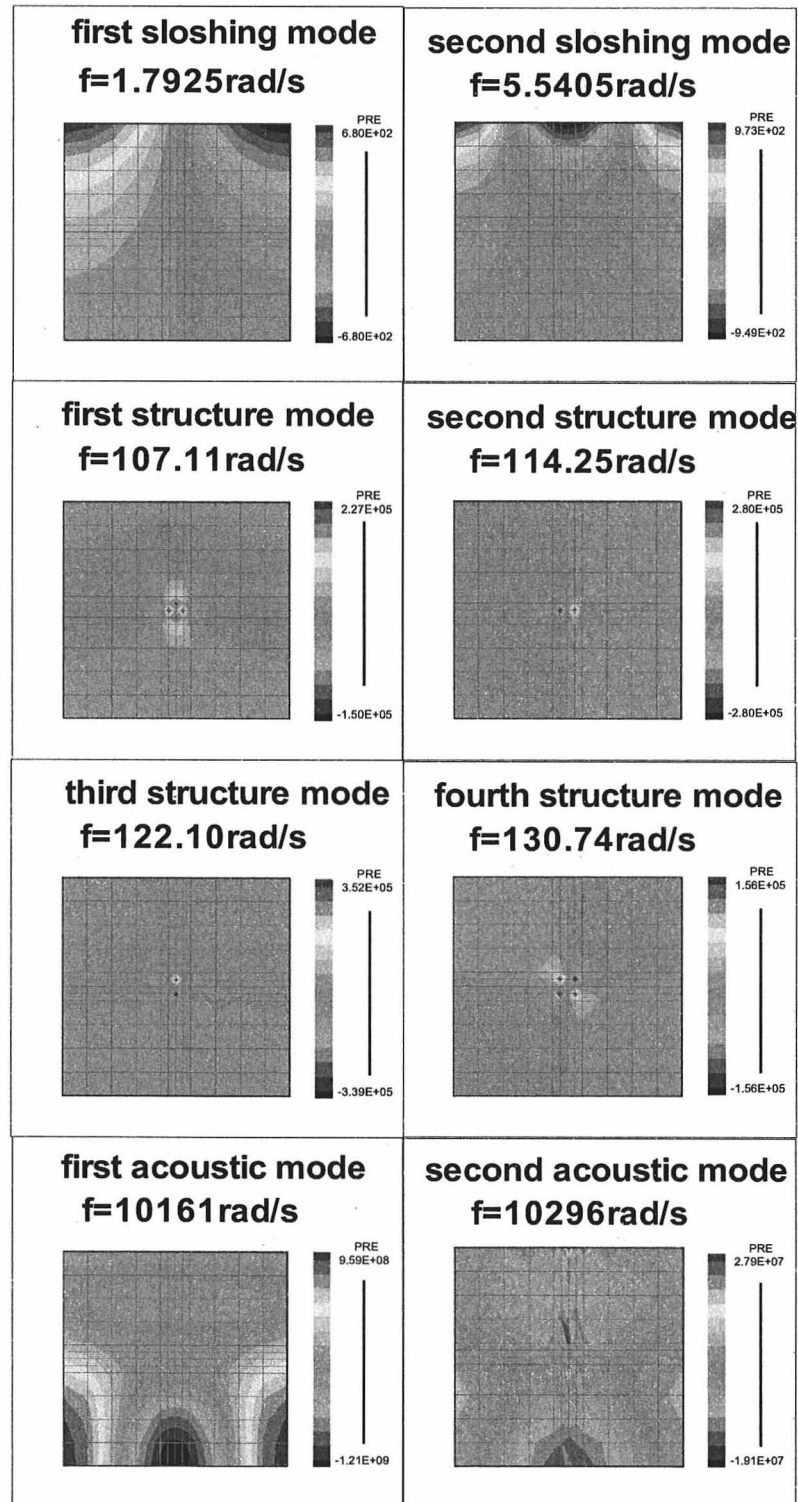


Figure 4.3 Displacement of sloshing/structural/acoustic modes of model I.



**Figure 4.4** Pressure of sloshing/structural/acoustic modes of model I.

with mass matrix  $(M_{uu})_h$ . Therefore, the problem becomes proving that the  $\mathbf{u}-p-\Lambda$  formulation with  $9-4c-4c$  elements satisfies the inf-sup condition. Fig. 4.6 shows the inf-sup value *vs.* the number of elements  $N$  in  $\log-\log$  coordinates. Three quantities are located in a very small interval. It is clear that the inf-sup value approaches some value without blowing up, which indicates that the  $9-4c-4c$  elements pass the



**Figure 4.5** Pressure of sloshing/structural/acoustic modes of model I with 144 elements.

test.  $N$  represents the square root of the number of the elements used for any local element. If the appropriate basis for displacement and pressure unknowns is selected, the  $\mathbf{K}_{up}$  matrix can be composed by a diagonal matrix followed by the kernel of  $\mathbf{K}_{up}$ . Therefore, the first singular value is attempted to generate inf-sup value. The result is shown in Fig. 4.7. Similar as Fig. 4.6, the value does not decay as the number of elements employed increases.

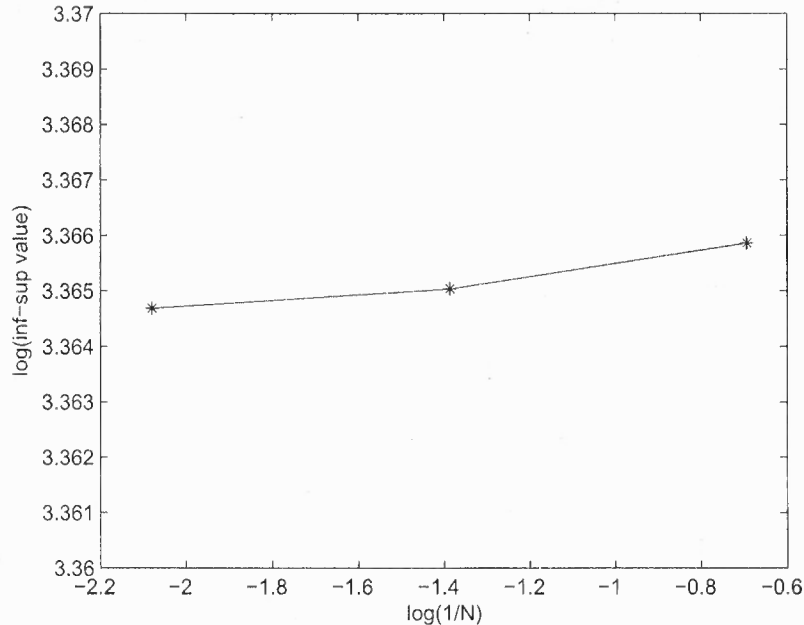


**Figure 4.6** Numerical inf-sup test of 9-4c-4c elements for  $\mathbf{u}-p-\Lambda$  formulation.

If a constant pressure is loaded on the free surface, the elastic solid is subjected to an external incident pressure. The known nodal pressure with subscript  $a$  and its corresponding entries of the stiffness matrix should be transferred to the right hand side of the equation. Starting from Eq. (2.56), the pressure stiffness matrix and pressure vectors can be decomposed as follows:

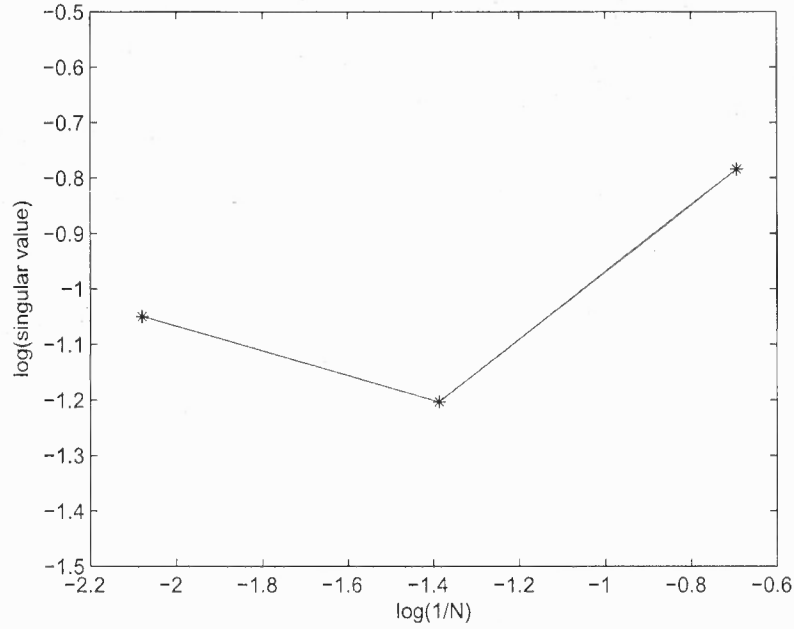


Figure 4.7 Singular value of matrix  $[\mathbf{K}_{up} \ \mathbf{K}_{ul}]$  for  $\mathbf{u} - p - \Lambda$  formulation.

$$\begin{pmatrix} \mathbf{M}_{uu} & \mathbf{0} & \mathbf{0} \\ \mathbf{0} & \mathbf{0} & \mathbf{0} \\ \mathbf{0} & \mathbf{0} & \mathbf{0} \end{pmatrix} \begin{pmatrix} \ddot{\mathbf{U}} \\ \ddot{\mathbf{P}} \\ \ddot{\Lambda} \end{pmatrix} + \begin{pmatrix} \mathbf{K}_{uu} & \mathbf{K}_{up}^a & \mathbf{K}_{up}^b & \mathbf{K}_{ul} \\ \mathbf{K}_{pu}^a & \mathbf{K}_{pp}^{aa} & \mathbf{K}_{pp}^{ab} & \mathbf{0} \\ \mathbf{K}_{pu}^b & \mathbf{K}_{pp}^{ba} & \mathbf{K}_{pp}^{bb} & \mathbf{0} \\ \mathbf{K}_{lu} & \mathbf{0} & \mathbf{0} & \mathbf{K}_{ll} \end{pmatrix} \begin{pmatrix} \mathbf{U} \\ \mathbf{P}_a \\ \mathbf{P}_b \\ \Lambda \end{pmatrix} = \begin{pmatrix} \mathbf{R} \\ \mathbf{0} \\ \mathbf{0} \\ \mathbf{0} \end{pmatrix}, \quad (4.1)$$

where subscript  $b$  indicates the unknown part of pressure vectors. Condensing the rows and columns correspond to  $\mathbf{P}_a$ , it turns out to be

$$\begin{pmatrix} \mathbf{M}_{uu} & \mathbf{0} & \mathbf{0} \\ \mathbf{0} & \mathbf{0} & \mathbf{0} \\ \mathbf{0} & \mathbf{0} & \mathbf{0} \end{pmatrix} \begin{pmatrix} \ddot{\mathbf{U}} \\ \ddot{\mathbf{P}}_b \\ \ddot{\Lambda} \end{pmatrix} + \begin{pmatrix} \mathbf{K}_{uu} & \mathbf{K}_{up}^b & \mathbf{K}_{ul} \\ \mathbf{K}_{pu}^b & \mathbf{K}_{pp}^{bb} & \mathbf{0} \\ \mathbf{K}_{lu} & \mathbf{0} & \mathbf{K}_{ll} \end{pmatrix} \begin{pmatrix} \mathbf{U} \\ \mathbf{P}_b \\ \Lambda \end{pmatrix} = \begin{pmatrix} \mathbf{R} - \mathbf{K}_{up}^a \mathbf{P}_a \\ -\mathbf{K}_{pp}^{ba} \mathbf{P}_a \\ \mathbf{0} \end{pmatrix}. \quad (4.2)$$

Continuously condense out the rows and columns correspond to  $\mathbf{P}_b$  and  $\mathbf{\Lambda}$ , with the result

$$\mathbf{M}_{uu}\ddot{\mathbf{U}} + \left\{ \mathbf{K}_{uu} - \begin{pmatrix} \mathbf{K}_{up}^b & \mathbf{K}_{ul} \end{pmatrix} \begin{pmatrix} \mathbf{K}_{pp}^{bb} & 0 \\ 0 & \mathbf{K}_{ll} \end{pmatrix}^{-1} \begin{pmatrix} \mathbf{K}_{pu}^b \\ \mathbf{K}_{lu} \end{pmatrix} \right\} \mathbf{U} =$$

$$\mathbf{R} - \mathbf{K}_{up}^a \mathbf{P}_a - \begin{pmatrix} \mathbf{K}_{up}^b & \mathbf{K}_{ul} \end{pmatrix} \begin{pmatrix} \mathbf{K}_{pp}^{bb} & 0 \\ 0 & \mathbf{K}_{ll} \end{pmatrix}^{-1} \begin{pmatrix} -\mathbf{K}_{pp}^{ba} \mathbf{P}_a \\ \mathbf{0} \end{pmatrix}.$$

At this point, the problem can be further simplified to

$$\tilde{\mathbf{M}}\ddot{\mathbf{U}} + \tilde{\mathbf{K}}\mathbf{U} = \tilde{\mathbf{R}}, \quad (4.3)$$

with

$$\tilde{\mathbf{M}} = \mathbf{M}_{uu}, \quad (4.4)$$

$$\tilde{\mathbf{K}} = \mathbf{K}_{uu} - \begin{pmatrix} \mathbf{K}_{up}^b & \mathbf{K}_{ul} \end{pmatrix} \begin{pmatrix} \mathbf{K}_{pp}^{bb} & 0 \\ 0 & \mathbf{K}_{ll} \end{pmatrix}^{-1} \begin{pmatrix} \mathbf{K}_{pu}^b \\ \mathbf{K}_{lu} \end{pmatrix} \quad (4.5)$$

$$\text{and } \tilde{\mathbf{R}} = \mathbf{R} - \mathbf{K}_{up}^a \mathbf{P}_a + \begin{pmatrix} \mathbf{K}_{up}^b & \mathbf{K}_{ul} \end{pmatrix} \begin{pmatrix} \mathbf{K}_{pp}^{bb} & 0 \\ 0 & \mathbf{K}_{ll} \end{pmatrix}^{-1} \begin{pmatrix} \mathbf{K}_{pp}^{ba} \mathbf{P}_a \\ \mathbf{0} \end{pmatrix}. \quad (4.6)$$

Figs. 4.8 and 4.9 show the displacement and pressure wave propagation at some time snapshots, respectively. Without loss of generality, it is assumed that both the body force and exterior force  $\mathbf{R}$  to be zero. Therefore, the motion of fluid is only activated by the constant lumped pressure on the free surface, and the incident fluid wave brings to the deflection of the immersed structure. Since the structure frequencies are relatively low, the fluid appears to the structure like an added mass [21], i.e., the fluid pressure on the wetted surface is in phase with structural acceleration [17]. If the fluid motion around the structure in the left column

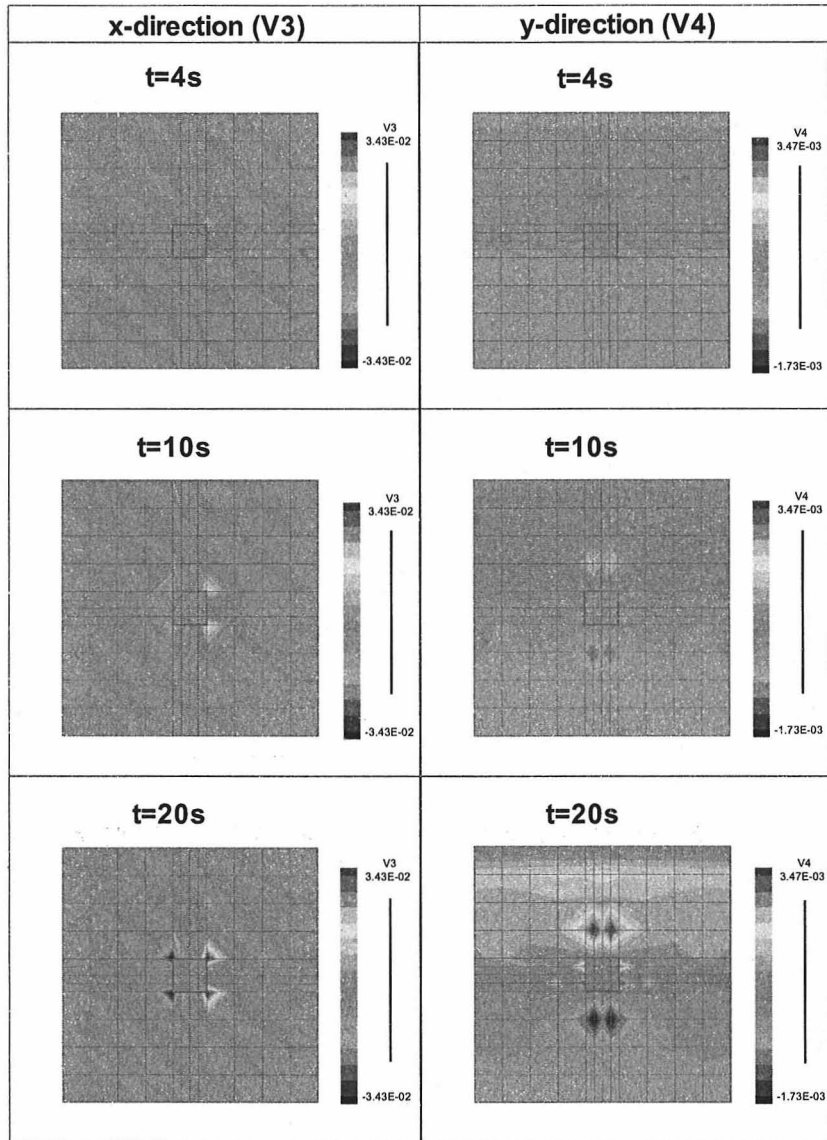


**Figure 4.8** Displacement wave propagation of transient analysis of FSI model I.

of Fig. 4.8 is considered, which depicts the displacement in x-direction, it can be observed that the right corners move to the right while left corners move to the left. That is to say, the structure is stretched in x-direction, which is consistent with the intuitive idea. It can be understood as the flat pressure on the free surface passes downward and keep loading on the structure while the fluid below the solid provides some balance. This pattern is similar as the stretching mode. This phenomenon

can be further observed in the right column of Fig. 4.8. Because of the reciprocity of the force, the structure provides some stiffness to the fluid; therefore, the fluid elements right above the structure move upward compared with other elements at the same height. The structure is squeezed and moves to the bottom of the cavity. Consequently, the nodal displacements right below the structure are relatively large in negative. Fig. 4.8 shows that the pressure wave propagates downward and then bounce back by the boundaries of the solid and the open cavity. Notice that the wave speed  $c$  can be calculated based on the fluid density and bulk modulus,

$$c = \sqrt{\frac{\beta}{\rho}}, \quad (4.7)$$

which is another criterion on the correctness of the numerical solution.

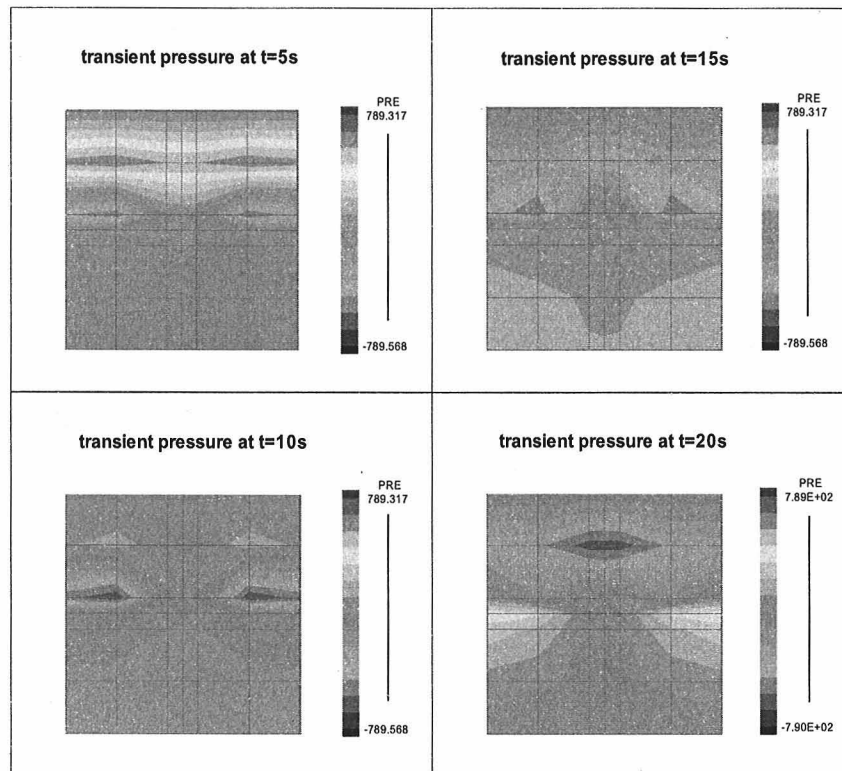


**Figure 4.9** Pressure wave propagation of transient analysis of FSI model I.

## 4.2 2-D Rectangular Solid Attached to the Wall of an Open Cavity

Fig. 4.10 describes the paradigm of another two-dimensional FSI model. In the following example, an elastic beam is immersed into acoustic fluid with the left hand side sticking with the cavity boundary.

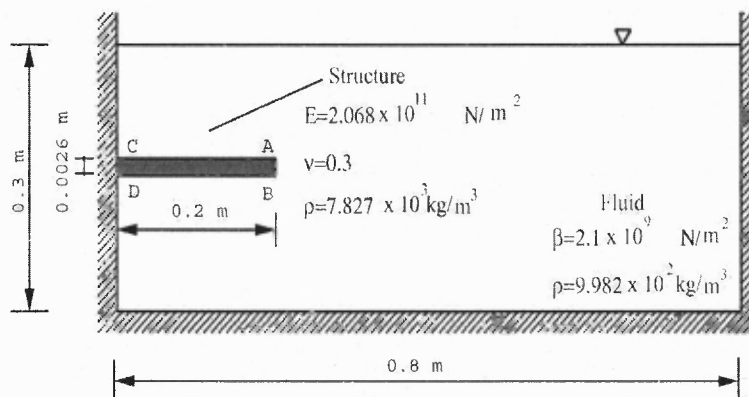


Figure 4.10 Model II: Rectangular solid attached to the wall of a open cavity.

Table 4.2 lists the frequency range (rad/s) of three different modes respectively. Using the mixed finite element formulation, coupled FSI modes within sloshing, structural, and acoustic ranges can be computed simultaneously. To ensure there exists no non-zero spurious frequency, the number of zero frequencies is compared with the mathematical prediction. From Table 4.2, it can be deduced that they are

Table 4.2 Frequency Range of FSI Model II

Eigenmode	Number of elements	Number of zero		Range of frequency (rad/s)
		Theory	Result	
Sloshing				5.3889-33.468
Structure	40	343	343	149.59-1806.7
Acoustic				7384.6-103531

identical to each other. In other words, the theoretic formulation of zero frequency is perfectly applicable for this model.

Fig. 4.11 shows the mode shapes (displacements) of the first two modes for each kind. It can be clearly seen that the free surface is no longer flat in the first two sub-figures, which indicates the fluid sloshing motion. Notice that for surface sloshing waves, the structure is hardly moved, since the structural natural frequencies are much higher than the sloshing frequencies. Likewise, the structural modes hardly trigger the sloshing motion in the next two sub-figures. The structure locates in the middle and to the left side of the cavity. It can be seen that the right end of structure moves upward in the first structural mode while downward in the second structural mode. These results are in agreement with the mechanics of the cantilever beam. The last two sub-figures show the acoustic modes. It can be found that the second acoustic mode looks like the first sloshing mode, except the structure staying at rest. That is may because the fluid in the cavity is considered as a whole, it will be difficult to separate the sloshing motion from the acoustic modes.

Fig. 4.12 is the pressure band plots for the same modes as Fig. 4.11. According to the convention, the pressure is assumed to be positive in compression. Notice that the first two sub-figures (sloshing modes) are similar as the mode shapes of FSI model I. They usually show pressure distribution similar as the wave propagation at some time instance. In the next two structural modes, pressure is discontinuous on the upper and lower side of the solid. The fluid nodes right below the solid undergo higher pressure because of the mode shape of the solid. In acoustic modes, the free surface is essentially a surface with constant pressure conforming to the often used flat free surface with constant pressure assumption for underwater acoustic. Likewise, for sloshing modes, the pressure distributions match the surface elevations in tank sloshing problems.

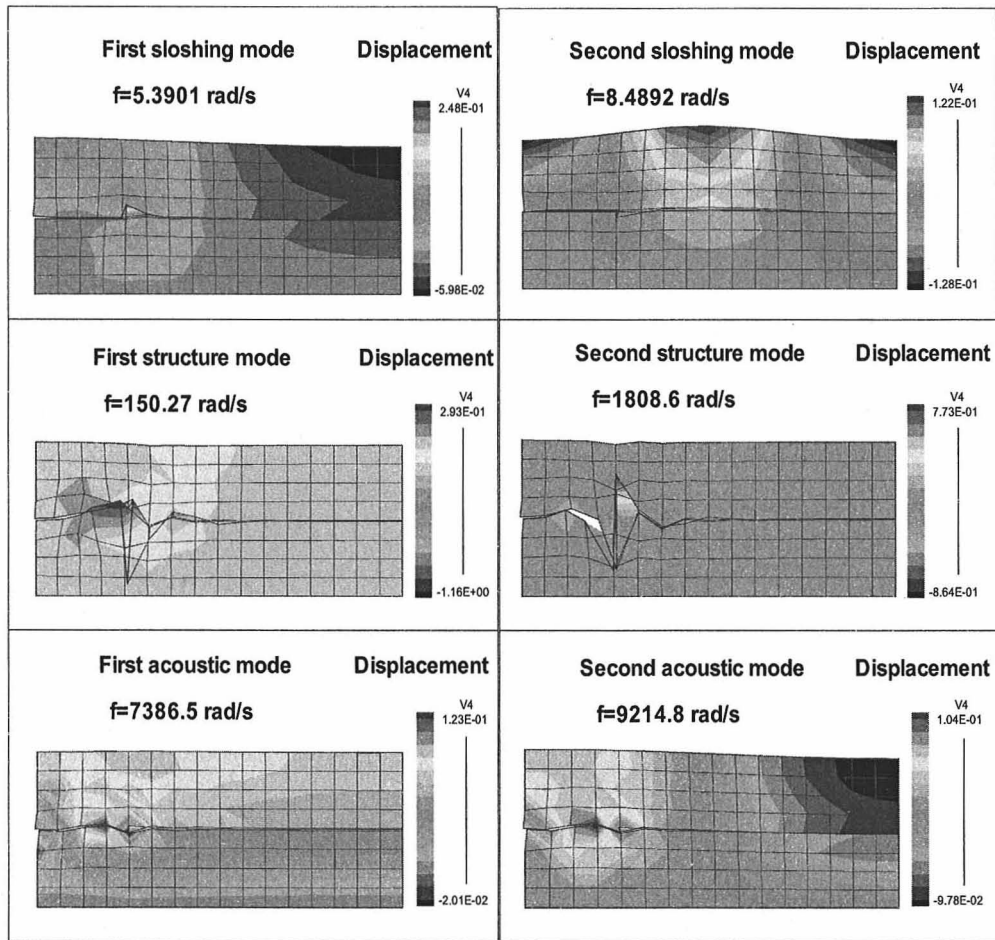
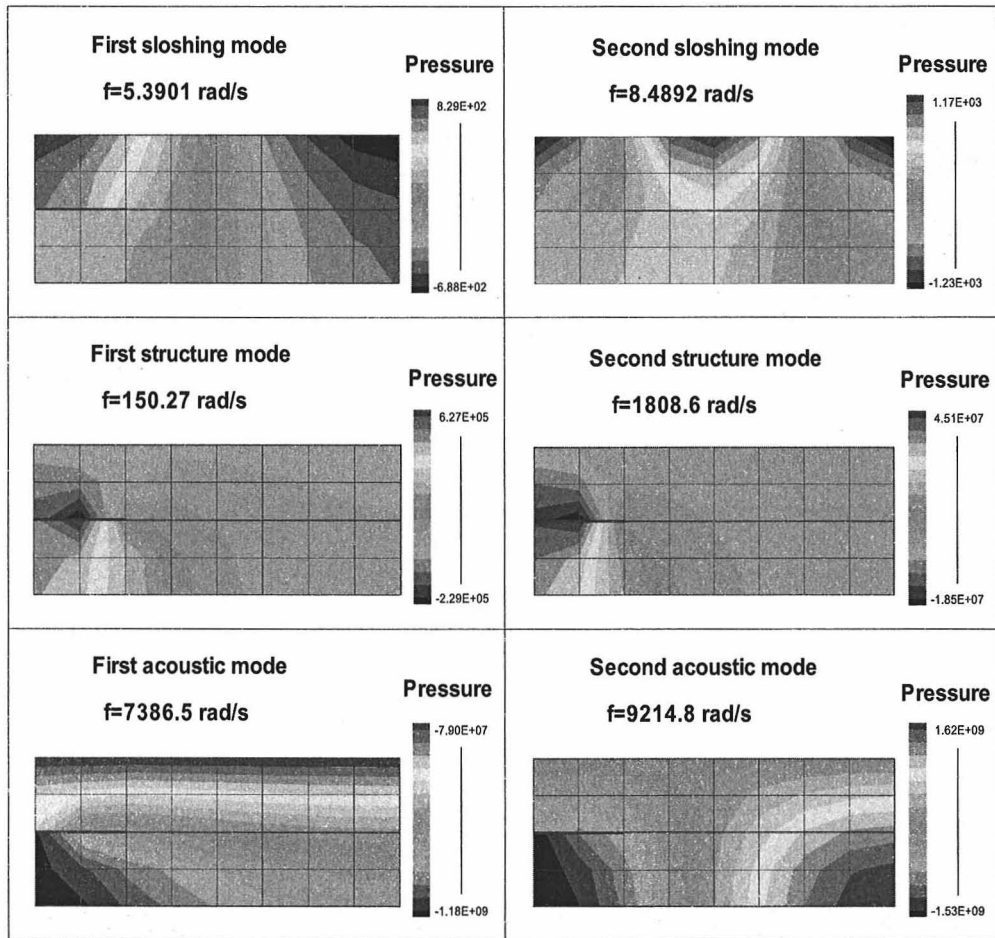


Figure 4.11 Displacement of sloshing/structural/acoustic modes of model II.

Figs. 4.13 and 4.14 show the nodal displacements and pressure of both fluid and structure elements, respectively, if the nodal force  $R(t) = \sin(\omega t)$  is exerted on the right end of the structure in the normal direction at some transient times  $t$ , where  $\omega$  is the natural frequency obtained by mode superposition method or Rayleigh-Ritz quotient by singular value decomposition. Fig. 4.13 describes the fluid motion around the structure when  $\omega$  is set to be a structural frequency. Obviously, neither the sloshing mode nor the acoustic mode is excited. In contrast, Fig. 4.14 clearly displays a wave propagation on the free surface if  $\omega$  is equal to a sloshing frequency. The wave pressure is continuous and consistent among the fluid elements while discontinuous when reaching the structure. At the beginning, the wave crest on the free surface



**Figure 4.12** Pressure of sloshing/structural/acoustic modes of model II.

appears right above the right end of the structure and then propagates to the right. When it arrives at the right side of the cavity, the wave trough moves from the left side of the free surface to the center.

Now the FSI system is activated by picking up any sloshing/structure node and loading concentrated force on it. The nodal displacements are then arranged into columns for each discrete time. Supposing there are  $m$  degrees of freedom in the system after condensation and the maximum number of snapshots is  $nstep$ , then a  $m$ -by- $nstep$  matrix can be built up. Then SVD is performed on this matrix and the first principal singular vector  $u$  can be obtained. Rayleigh-Ritz quotient  $\omega$  can be

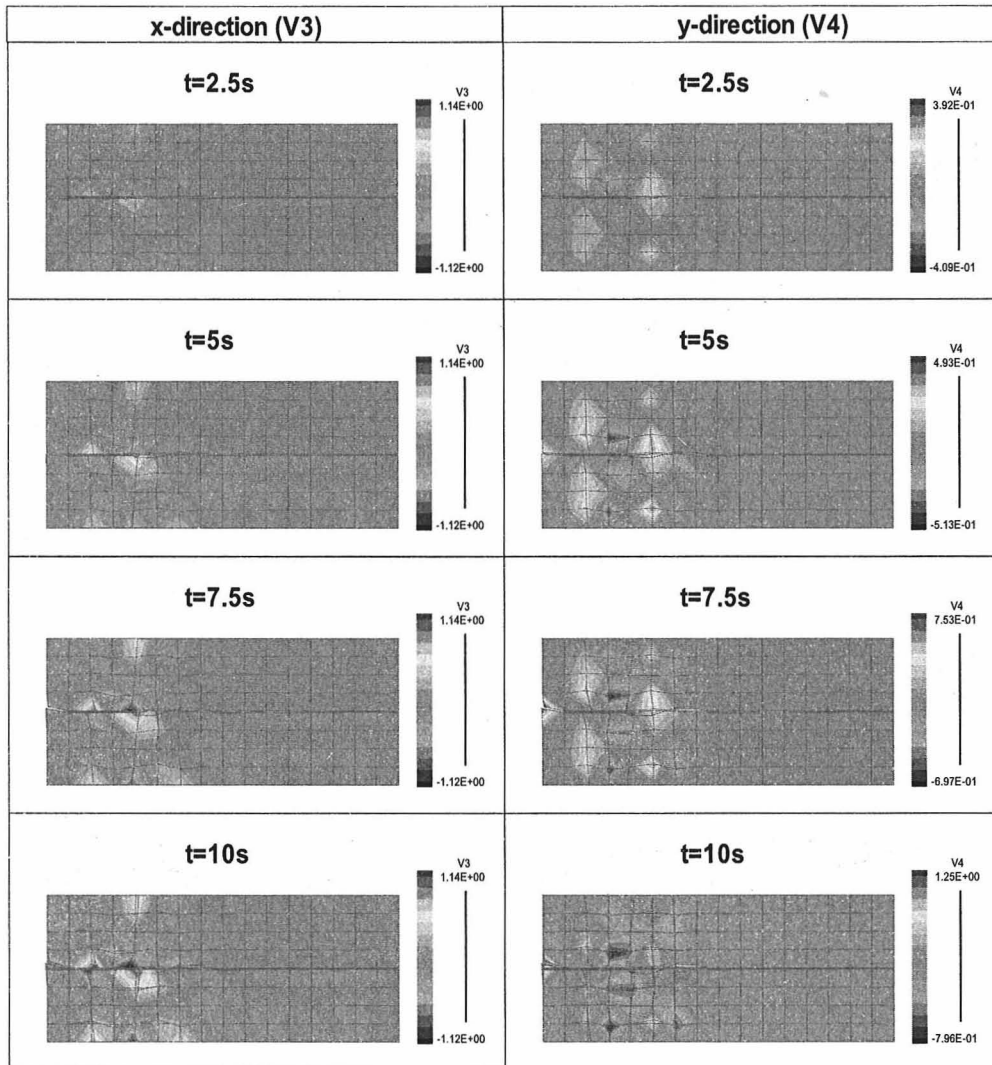


**Figure 4.13** Displacement wave propagation of transient analysis of model II.

calculated according to the following formula:

$$\text{Raleigh-Ritz quotient: } \omega^2 = \frac{u^T \mathbf{K} u}{u^T \mathbf{M} u}. \quad (4.8)$$

Figs. 4.15 and 4.16 show the Rayleigh-Ritz quotients *vs.* the number of snapshots of the SVD. The quotients start from the natural frequency, e.g. 17 rad/s for sloshing mode and 143 rad/s for structural mode, remaining relatively flat up to around 100 snapshots, then gradually decaying to zero. That is to say, the system responds

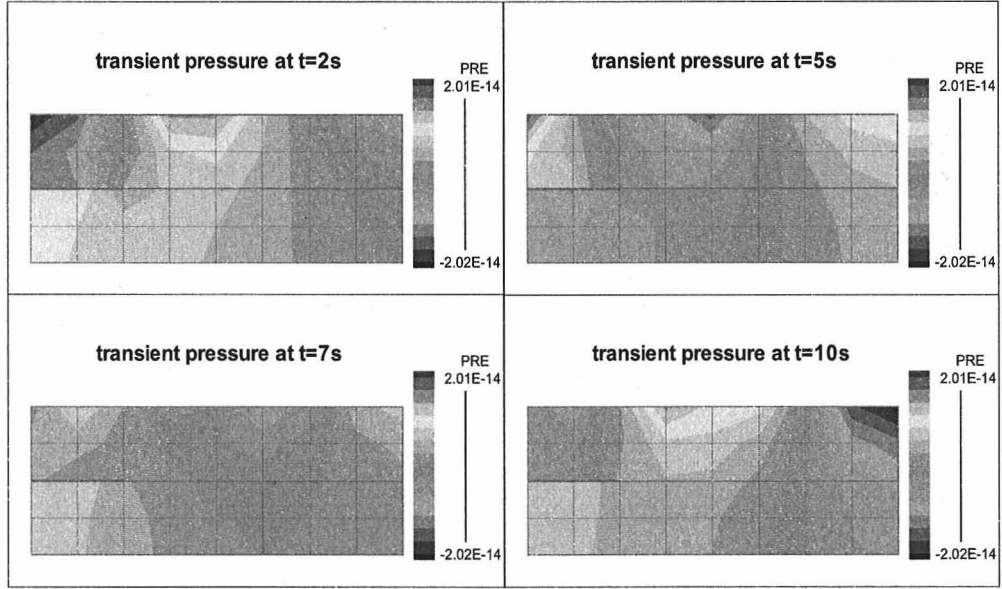


**Figure 4.14** Pressure wave propagation of transient analysis of model II.

quickly to the external force, then the interaction between fluid and solid disturbs the appearance of eigenmodes. In other words, increasing the number of snapshots cannot bring to closer Rayleigh-Ritz quotient to the natural frequency.

In order to verify the effect of SVD, the stored energy in the FSI system is calculated by considering the first order Sobolev norm,

$$(\|\mathbf{v}\|_0)^2 = \sum_i \|v_i\|_{L^2(Vol)}^2 + \sum_{i,j} \left\| \frac{\partial v_i}{\partial x_j} \right\|_{L^2(Vol)}^2. \quad (4.9)$$

Figs. 4.17 and 4.18 show the energy of original transient displacements and recovered data by the first few basis matrices. The solid curve depicts the energy at discretized time snapshots, while the dotted curve describes the energy after SVD. Since the recovery data comes from the projection of original transient data onto principal components, the dotted curve is close to the solid curve but not identical. Even so, the relatively efficient data can be obtained without losing important characteristics in terms of catching the same configuration at any time instance. This phenomenon is more easy to observe in Fig. 4.18. As for the rising of the energy, that is because the

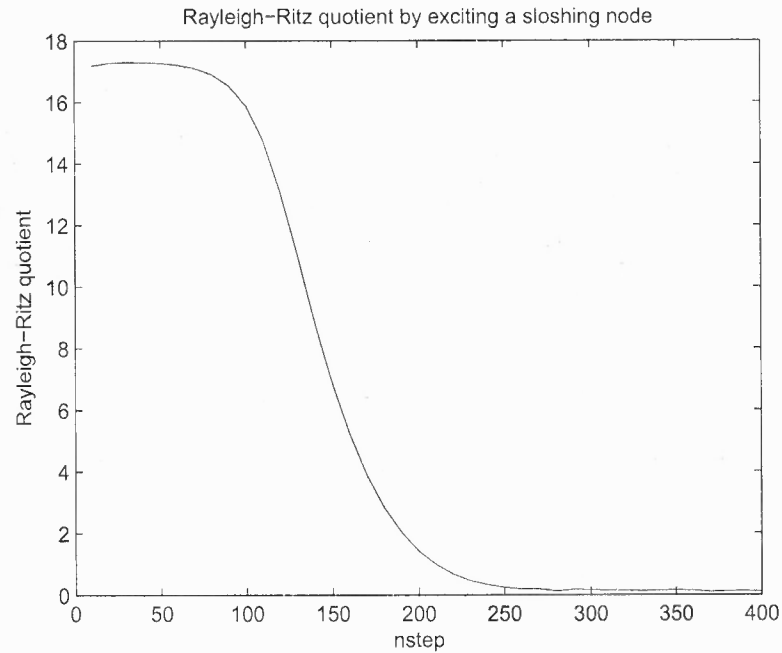


Figure 4.15 Rayleigh-Ritz quotient *vs.*  $nstep$  for sloshing mode.

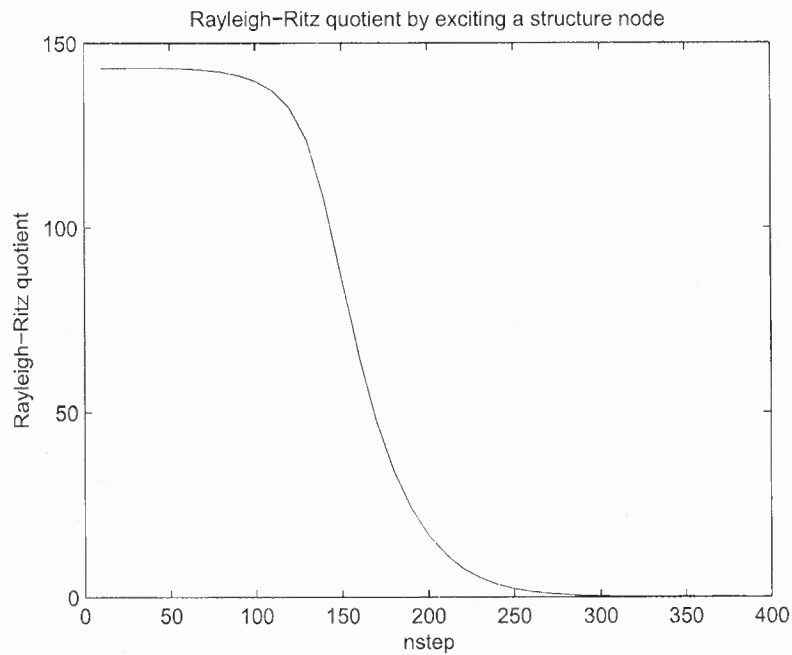


Figure 4.16 Rayleigh-Ritz quotient *vs.*  $nstep$  for structural mode.

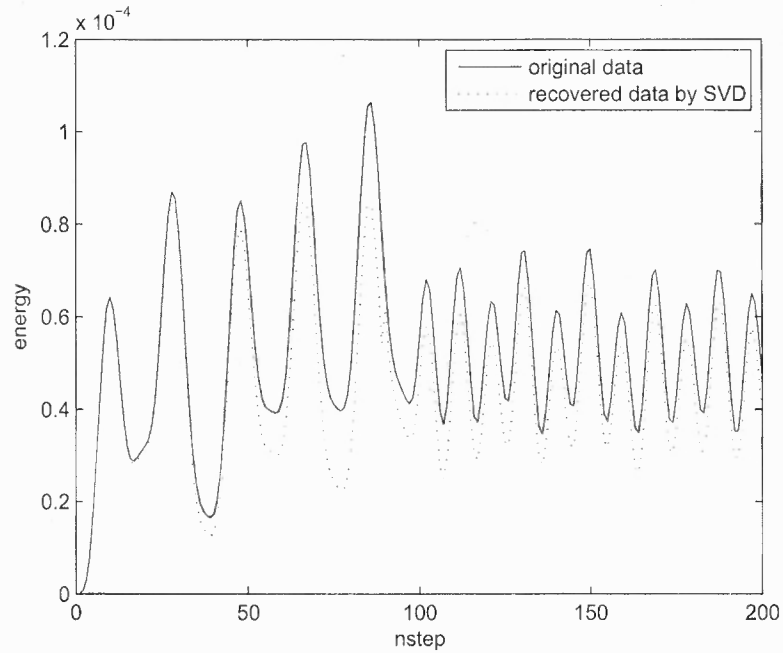


Figure 4.17 Energy of transient data and recovered results of sloshing mode.

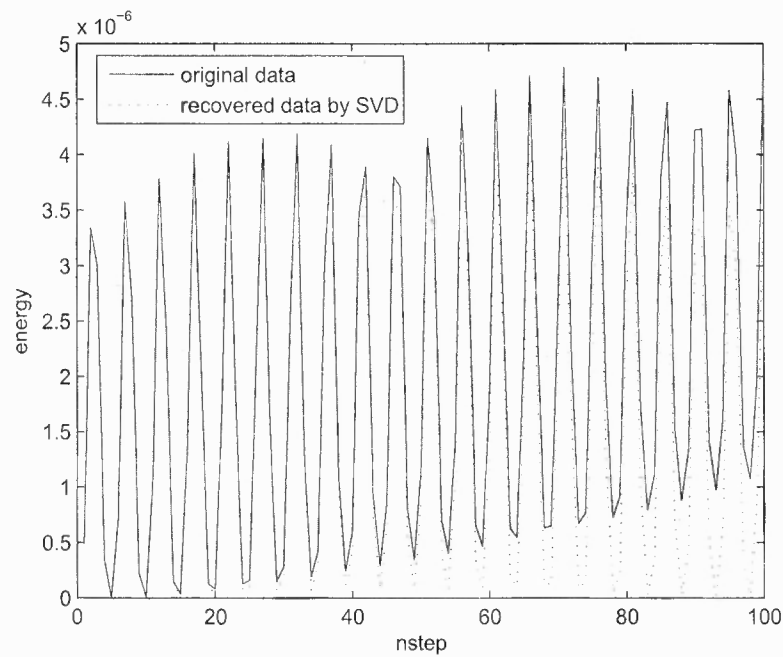


Figure 4.18 Energy of transient data and recovered results of structural mode.

load on the single node is monotonically increasing with constant slope for  $nstep \leq 100$  and equal to one afterwards. Therefore, the energy in a freely vibrating period generally remains constant since no damping forces act to absorb it. The conclusion can be drawn that SVD is reliable for transient analysis activated by a single node.

Now the force term is reset to be the displacement of the given point in the last iteration, which is equivalent to a harmonic excitation even though the natural frequency is unknown in advance. In Fig. 4.19, it is noticed that the Rayleigh-Ritz quotient will converge to the highest sloshing frequency of the system as the number of snapshot  $nstep$  increases. Similar results can be observed if the sloshing node is changed to a structure node. In Fig. 4.20, it can be observed that the Rayleigh-Ritz quotient approaches the lowest structure natural frequency. The small gap between the tail of the convergent curve and the flat line is due to the variance of the singular vector. The larger the percentage of the variance, the smaller the gap. This percentage tells how much the energy is concentrated along the particular singular vectors. For example, the variance of  $u$  is 91.3425% for sloshing mode and 96.8463% for structural mode.

Thus, the conclusion can be drawn that the Rayleigh-Ritz quotients obtained by singular value decomposition can be used to predict the root of eigenvalues achieved by mode superposition method. Therefore, there is no need to solve the eigen problem of large dimension matrix, which size is  $m$ -by- $m$  in order to achieve the natural frequencies of a fluid-structure interaction system.

If a single mode is given as the initial force to the FSI system, the transient data can be recovered by taking the first three principal basis matrices based on the percentage of the variances 83.3439%, 7.5835%, 1.4352%. All the degrees of freedom can be considered as a vector, then compose the vectors at different time snapshots into a matrix and take the singular value decomposition. Fig. 4.21 shows the original displacement (on the left column) and recovered data (on the right column) at some

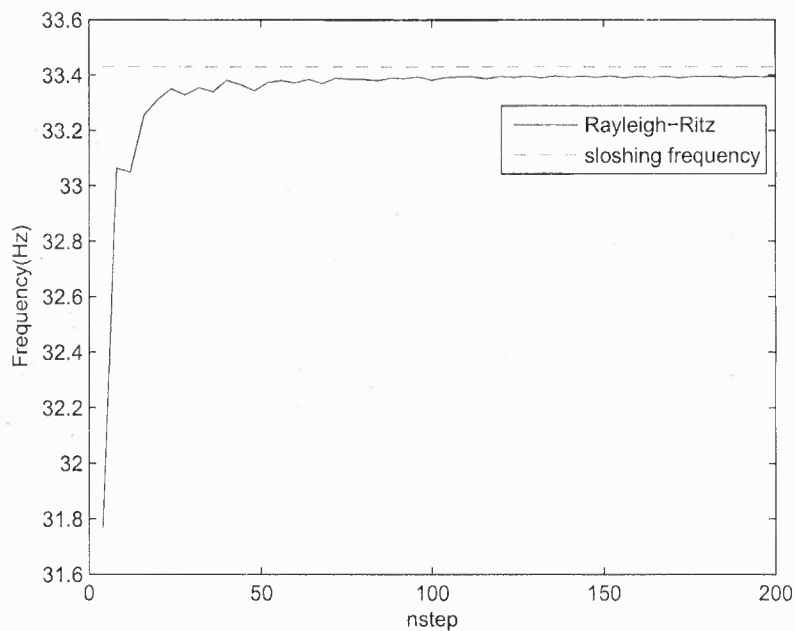


Figure 4.19 Rayleigh-Ritz quotient/sloshing frequency *vs.* *nstep*.

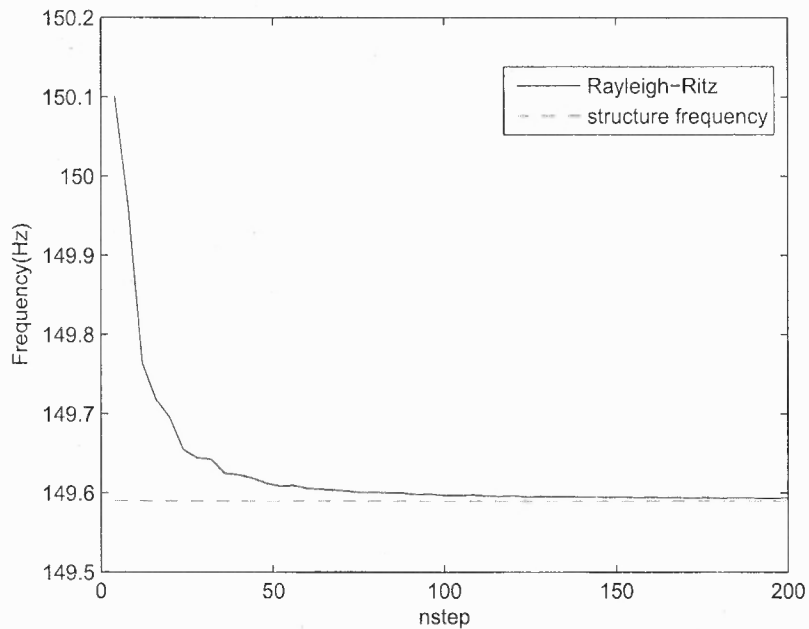
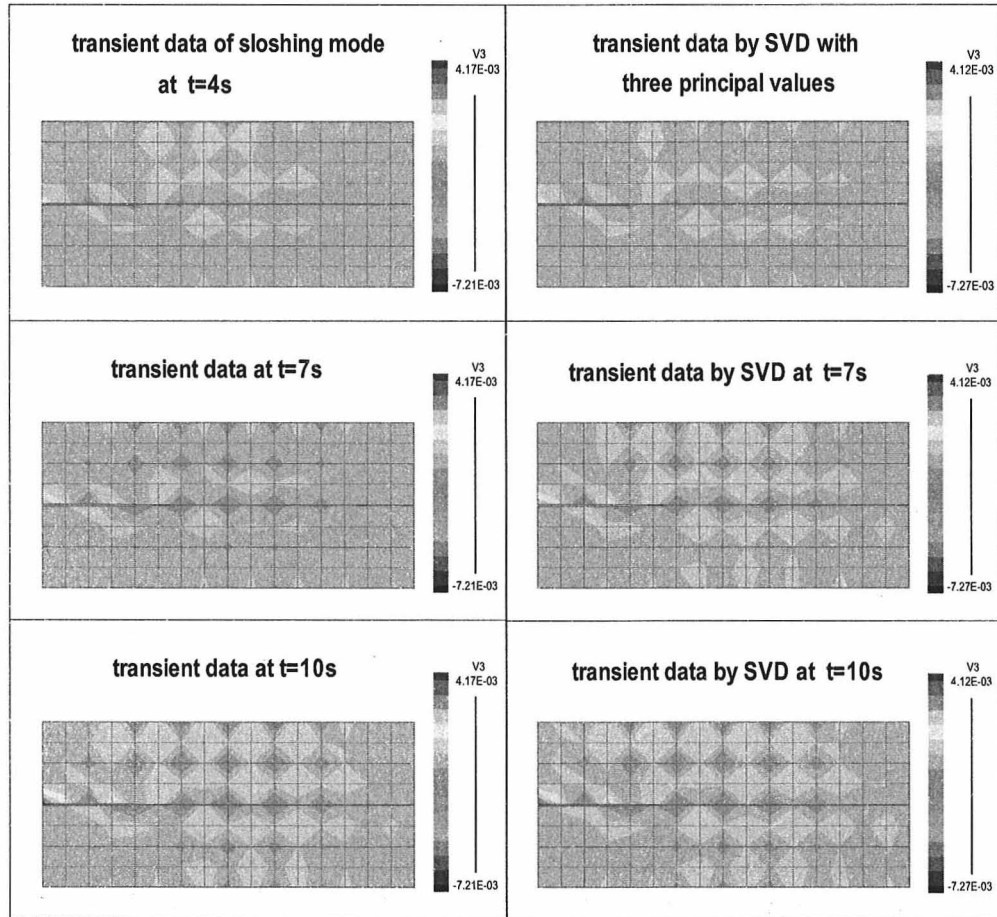


Figure 4.20 Rayleigh-Ritz quotient/structural frequency *vs.* *nstep*.

time instances for sloshing mode. In addition to the similarity of the sub-figures on the left and right column, energies also verify the promising match. Similar results can be obtained for structure (Fig. 4.22) and acoustic mode.



**Figure 4.21** Original and recovered transient data of sloshing mode.

It is anticipated that by varying time step  $dt$ , different recovered transient results can be obtained if the system is perturbed with a combination of two or more eigenmodes. Fig. 4.23 shows the transient data based on the same initial force for different time steps. For example, if  $dt = 0.01$ , part of the sloshing modes can be captured in addition to the structural modes. However, when the time step is decreased to  $dt = 0.0001$ , the acoustic mode emerges while the sloshing mode recedes. This is because the range of natural frequencies are quite separate for each of three

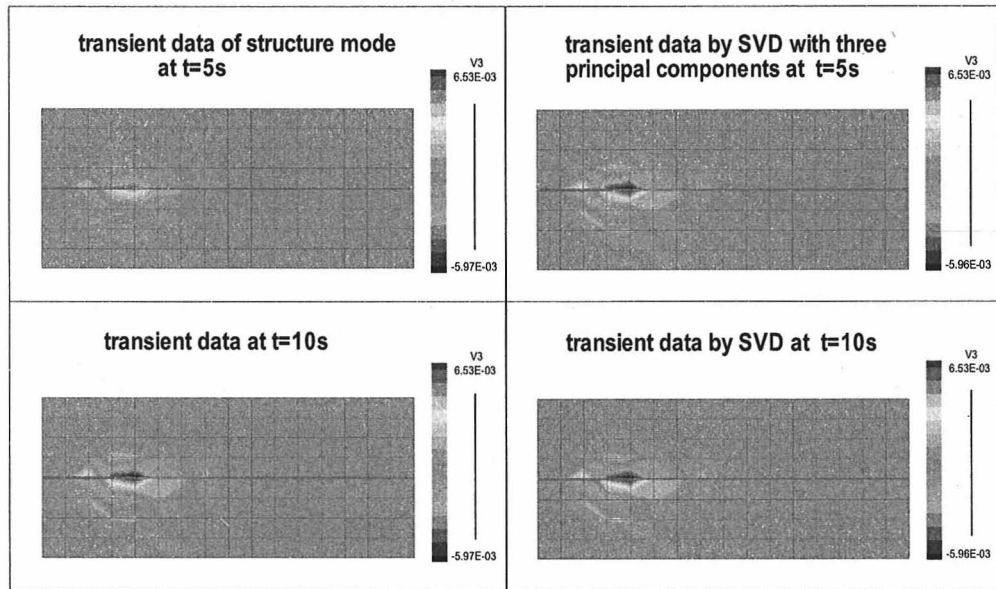


**Figure 4.22** Original and recovered transient data of structural mode.

eigenmodes. This leads to a question: what  $dt$  is the most appropriate time step for singular value decomposition if the motion of the whole system need to be captured, both fluid and solid?

In Fig. 4.24, the solid curve represents the displacement in  $y$ -direction of a node on the free surface in fine temporal scale, while the dashed curve represents coarse temporal scale. Now, starting from the initial time and taking 5 snapshots at time step  $dt$ . If there is  $m$  degrees of freedom after condensation, a  $m$ -by-5 matrix  $\mathbf{A}$  can be assembled. SVD is then implemented in matrix  $\mathbf{A}$ , the transient data can be recovered with a selected number of principal components. Essentially, at every time instance, the coefficients or general coordinates related to these principal components are calculated by solving a normal equation.

Moreover, using the recovered transient information, the system can then be extrapolated based on a much larger time step  $dT$ . At the new time instance  $t + dT$ , after relaxation within a prescribed time duration which is often smaller than  $dT$ . Repeat the same process with this kind of combination of fine and coarse time step

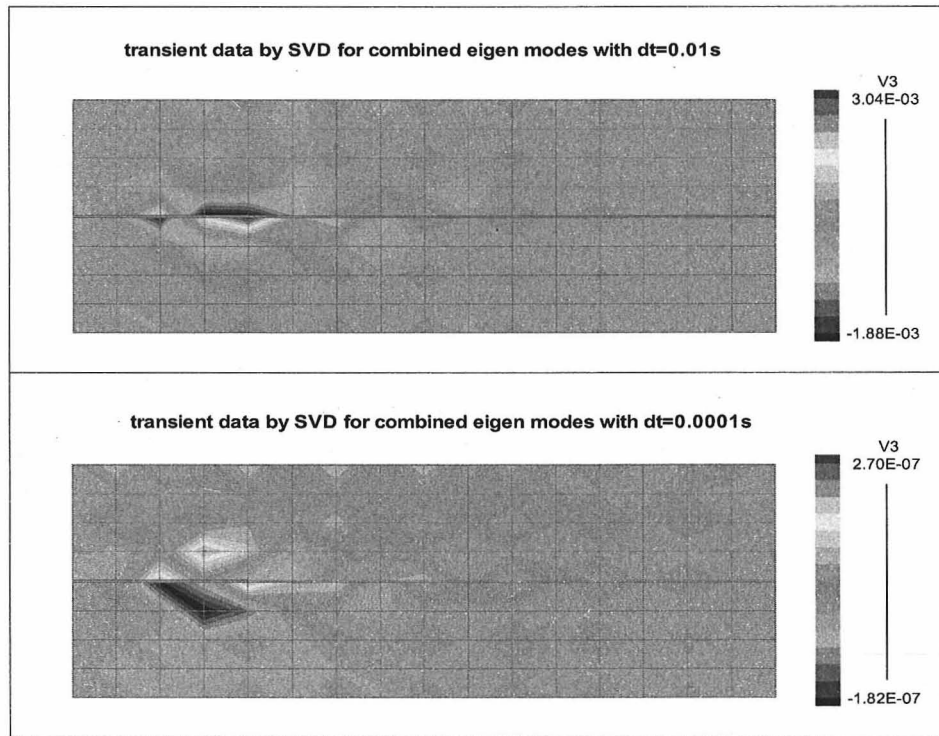


Figure 4.23 Original and recovered transient data of combined mode.

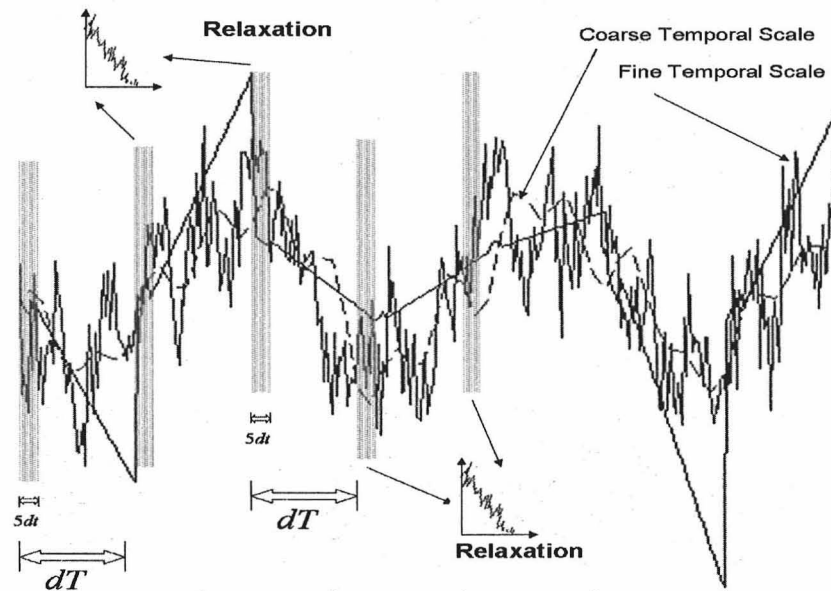


Figure 4.24 Data recovery by SVD and relaxation.

sizes. Fig. 4.25 shows the root mean square deviation (RMSD) error between the original and extrapolated results with respect to  $dT$ . Referring to both figures, it can be found that the slopes at the point  $40dt$  and  $60dt$  are very small (less than 0.03). Moreover, Fig. 4.26 suggests that as soon as the number of snapshots is sufficiently large there is no need to further increase the number of snapshots. Therefore,  $dT = 60dt$  with the number of time snapshots  $nstep$  equal to 2000 is determined. Similar studies can also be carried out for fine time step size  $dt$ . Fig. 4.26 shows some results based on different time steps. In this case, considering the memory and numerical flops,  $dt$  is set to be 0.0005.

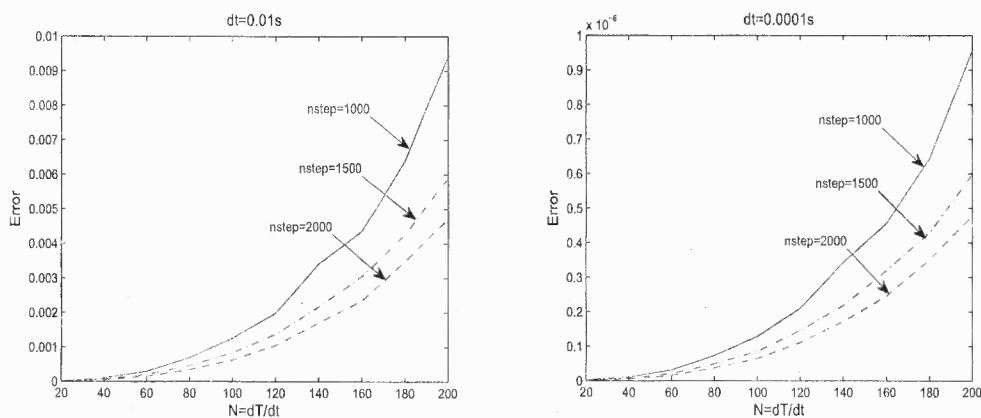


Figure 4.25 RMSD error *vs.*  $dT$  with  $dt = 0.01$  and  $dt = 0.0001$ .

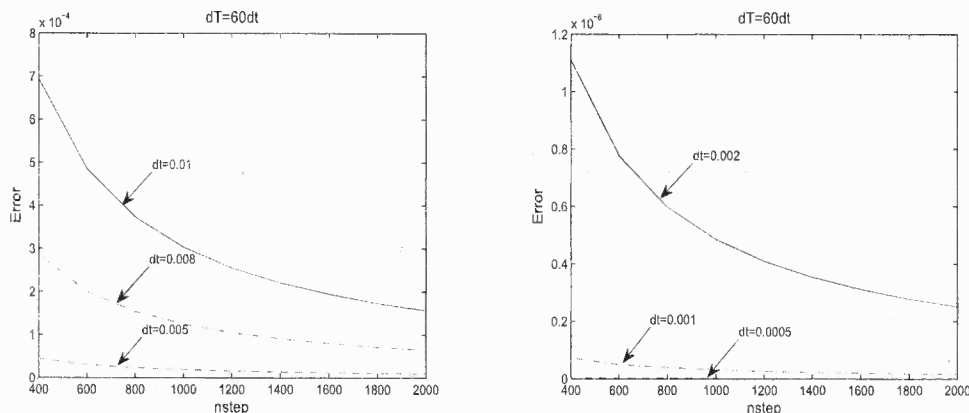
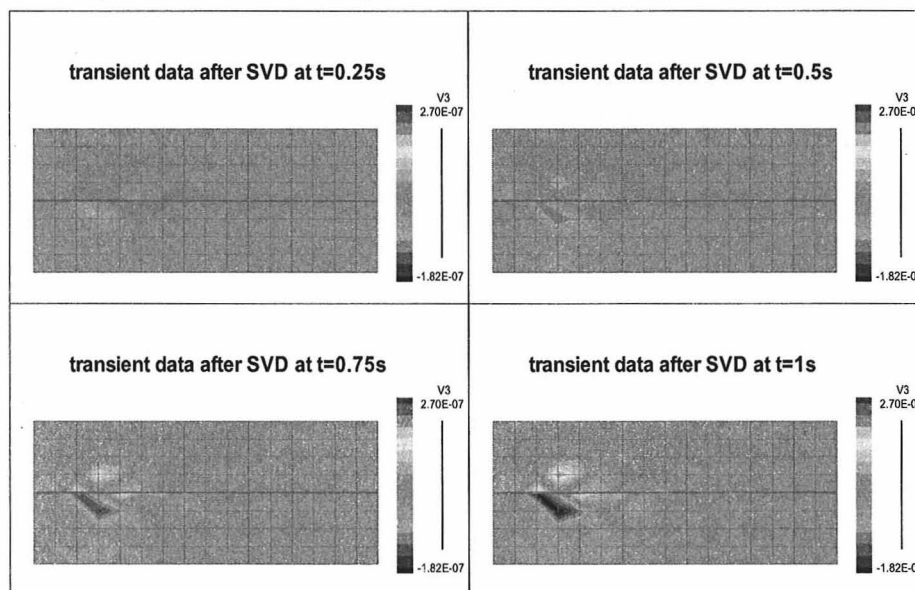


Figure 4.26 RMSD error *vs.*  $nstep$  with different  $dt$ .

Then return to the previous procedure and relax the extrapolated solution for ever time step  $dT$ . Fig. 4.27 shows the recovered transient data with three principal components. The sloshing mode appears around  $t = 0.25$ , and structural and acoustic modes appear late around  $t = 0.75$ . That is to say, by setting appropriate  $dt$ ,  $dT$ , and  $nstep$ , all three modes can be captured at different time instances.



**Figure 4.27** Temporal coarse graining using SVD with snapshots at fine time step  $dt$ , extrapolation at coarse time step  $dT$ , and relaxation.

In addition to the configurations of mode shapes, the energy also needs to be considered between the transient data and the recovered results. Since the eigenmode is set as the initial displacement, it is equivalent to loading a harmonic excitation to the FSI system. Therefore, it can be seen that both energies monotonically increase as time passes, as shown in Fig. 4.28 shows. Moreover, even though the recovered displacements at certain time snapshots are not identical to the original data, the energy figure shows that SVD with relaxation is indeed applicable to the FSI system. These two curves match relatively well because the harmonic excitation makes the slope of the extrapolation uniformly consistent. Therefore, the extrapolation results approach the original data.

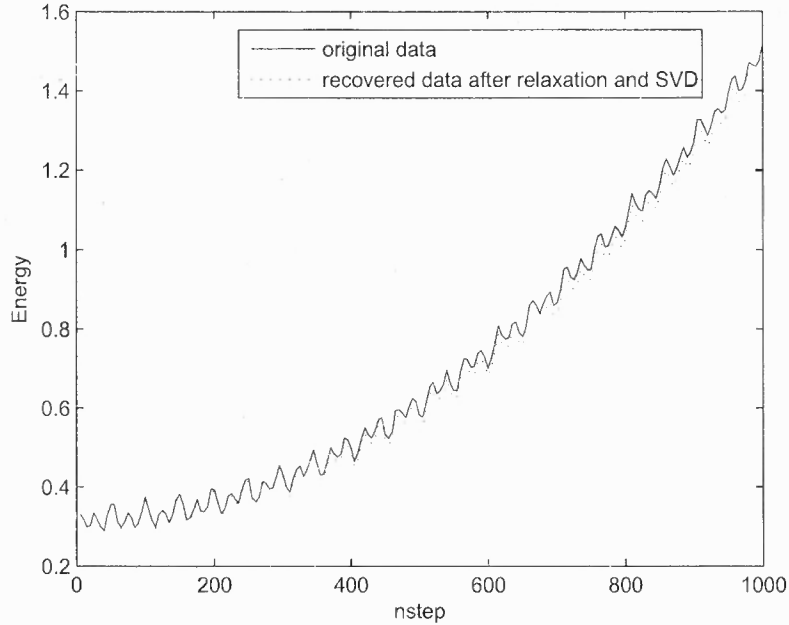


**Figure 4.28** Energy of transient combined modes and recovered data by SVD and relaxation.

However, when this method is implement with an FSI system with other initial conditions, the result is not as promising as the result shown above, especially when the slope of the transient data changes quickly. Fig. 4.29 shows the energy comparison when a constant external force is loaded on a node on the free surface. The relative error is still less than 7%. Compared with the original transient data in terms of number of snapshots and principal components, this method is still applicable.

Next, assume that Brownian motion is involved in the FSI system. Starting from Eq. (3.22)

$$\mathbf{M}\ddot{\mathbf{X}} + \mathbf{K}\mathbf{X} = \mathbf{V}(t), \quad (4.10)$$

where  $\mathbf{V}(t)$  represents a white noise vector.

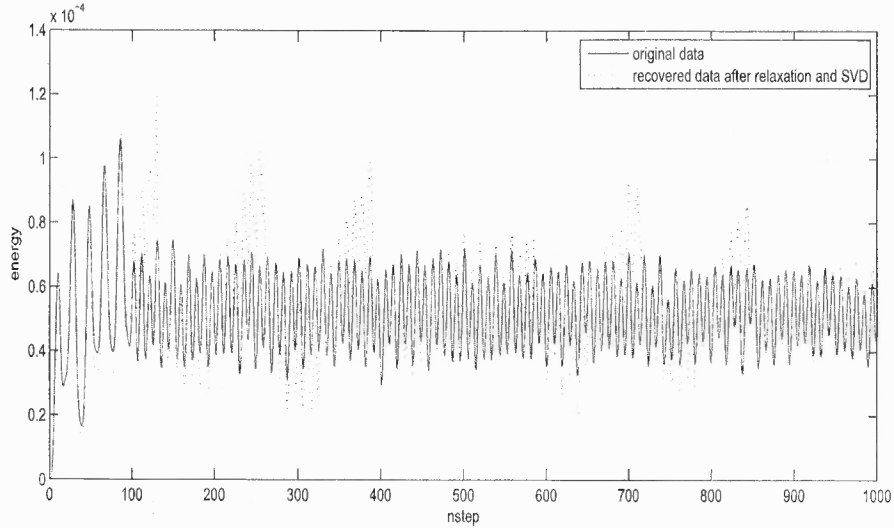


**Figure 4.29** Energy of transient sloshing mode and recovered data by SVD and relaxation.

Let  $\mathbf{Y} = \dot{\mathbf{X}}$ , a stochastic differential Eq. can be derived as

$$\begin{pmatrix} \dot{\mathbf{X}} \\ \dot{\mathbf{Y}} \end{pmatrix} = - \begin{pmatrix} \mathbf{0} & -\mathbf{I} \\ \mathbf{M}^{-1}\mathbf{K} & \mathbf{0} \end{pmatrix} \begin{pmatrix} \mathbf{X} \\ \mathbf{Y} \end{pmatrix} + \begin{pmatrix} \mathbf{0} \\ \mathbf{M}^{-1}\mathbf{V}(t) \end{pmatrix}, \quad (4.11)$$

i.e.,

$$d\mathbf{X} = -\mathbf{a}\mathbf{X}dt + \mathbf{b}d\mathbf{W}(t), \quad (4.12)$$

where

$$\mathbf{a} = \begin{pmatrix} \mathbf{0} & -\mathbf{I} \\ \mathbf{M}^{-1}\mathbf{K} & \mathbf{0} \end{pmatrix} \quad \text{and} \quad \begin{pmatrix} \mathbf{0} \\ \mathbf{M}^{-1} \end{pmatrix}. \quad (4.13)$$

Eq. (4.11) can also be expressed as Langevin equation

$$\dot{\mathbf{X}}_t = -\mathbf{a}\mathbf{X}_t + \mathbf{b}\dot{\mathbf{W}}(t). \quad (4.14)$$

Implementing implicit Euler method as Eq. (3.21), the following Eq. can be obtained

$$\begin{pmatrix} \mathbf{X}_{n+1} \\ \mathbf{Y}_{n+1} \end{pmatrix} = \begin{pmatrix} \mathbf{X}_n \\ \mathbf{Y}_n \end{pmatrix} - \Delta t \begin{pmatrix} \mathbf{0} & -\mathbf{I} \\ \mathbf{M}^{-1}\mathbf{K} & \mathbf{0} \end{pmatrix} \begin{pmatrix} \mathbf{X}_{n+1} \\ \mathbf{Y}_{n+1} \end{pmatrix} + \begin{pmatrix} \mathbf{0} \\ \mathbf{M}^{-1}\Delta\mathbf{W}_n \end{pmatrix}, \quad (4.15)$$

i.e.,

$$\begin{pmatrix} \mathbf{X}_{n+1} \\ \mathbf{Y}_{n+1} \end{pmatrix} = \begin{pmatrix} \mathbf{I} & -\mathbf{I}\Delta t \\ \mathbf{M}^{-1}\mathbf{K}\Delta t & \mathbf{I} \end{pmatrix}^{-1} \begin{pmatrix} \mathbf{X}_n \\ \mathbf{Y}_n \end{pmatrix} + \begin{pmatrix} \mathbf{I} & -\mathbf{I}\Delta t \\ \mathbf{M}^{-1}\mathbf{K}\Delta t & \mathbf{I} \end{pmatrix}^{-1} \begin{pmatrix} \mathbf{0} \\ \mathbf{M}^{-1}\Delta\mathbf{W}_n \end{pmatrix}. \quad (4.16)$$

If there exists deterministic exterior force besides the pure white noise vector  $\mathbf{V}(t)$ , e.g., constant load vector  $\mathbf{C}$ , the SDE turns to be

$$\mathbf{M}\ddot{\mathbf{X}} + \mathbf{K}\mathbf{X} = \mathbf{V}(t) + \mathbf{C}. \quad (4.17)$$

The iteration Eq. becomes

$$\begin{pmatrix} \mathbf{X}_{n+1} \\ \mathbf{Y}_{n+1} \end{pmatrix} = \begin{pmatrix} \mathbf{I} & -\mathbf{I}\Delta t \\ \mathbf{M}^{-1}\mathbf{K}\Delta t & \mathbf{I} \end{pmatrix}^{-1} \begin{pmatrix} \mathbf{X}_n \\ \mathbf{Y}_n \end{pmatrix} + \begin{pmatrix} \mathbf{I} & -\mathbf{I}\Delta t \\ \mathbf{M}^{-1}\mathbf{K}\Delta t & \mathbf{I} \end{pmatrix}^{-1} \begin{pmatrix} \mathbf{0} \\ \mathbf{M}^{-1}\Delta\mathbf{W}_n + \mathbf{M}^{-1}\Delta t\mathbf{C} \end{pmatrix}. \quad (4.18)$$

Similar to the case without noise, the Rayleigh-Ritz quotients are compared with the natural frequencies of different modes. If SVD is implemented to process the transient data, white noise will be weakened since the coefficients are determined based on the largest variance of data. Therefore, the white noise with relatively small variance decays. Figs. 4.30 and 4.31 show the Rayleigh-Ritz quotients calculated from the primitive singular vector, whose percentage of variance are 82.3253% and

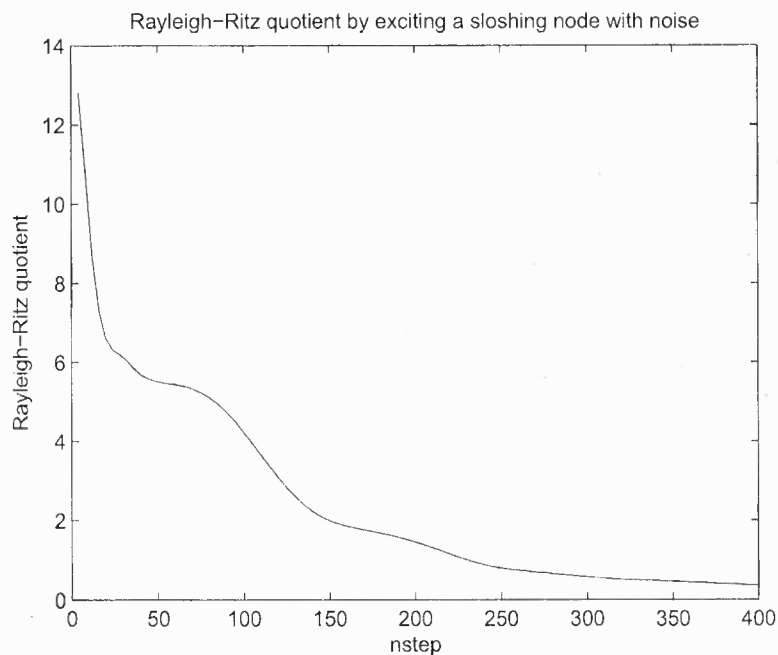


Figure 4.30 Rayleigh-Ritz quotient *vs.*  $nstep$  for sloshing mode with white noise.

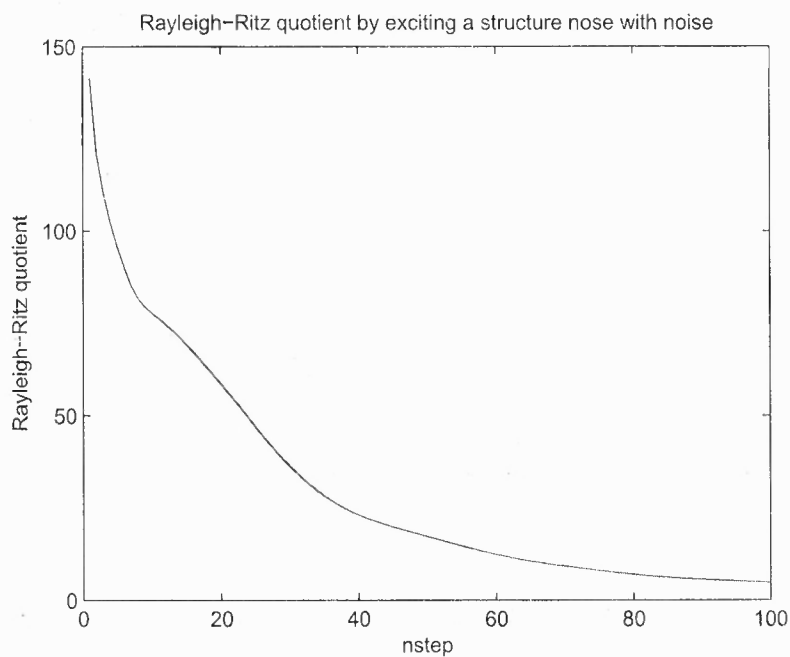


Figure 4.31 Rayleigh-Ritz quotient *vs.*  $nstep$  for structural mode with white noise.

77.8395%, respectively. When these two quantities are compared to the variances without noise, it can be clearly seen that the noise distracts the energy from the FSI system. Similar to Figs. 4.15 and 4.16, the Rayleigh-Ritz quotient starts from a typical sloshing/ structural frequency and decreases to some non-zero quantities as the number of snapshots increases. In addition, the quotients decrease much more quickly than in the case without noise, another significant difference is that there are no almost-constant quotients in a range of  $nstep$ . Due to the disturbance of the white noise, the first singular vector, on which the transient data projected, lose the characteristics of the corresponding eigenmodes of the FSI system. The pressure of noise reduces the capability of SVD to generate the natural frequencies.

Figs. 4.32 and 4.33 depict the mean of the transient displacement and pressure with white noise, respectively. The initial condition is set to be the positive displacements on all the degrees of freedom. In Fig. 4.32, it can be seen that the mean results significantly reduce the effect of the Brownian motion. For the same reason, the nodal pressure in Fig. 4.33 gradually approaches zero as time passes. Here, the number of realization 50 is determined based on the sample variances of the first principal component  $u$ . It is shown in Fig. 4.34 that the sample variance

$$S_N^2 = \frac{1}{N-1} \sum_{i=1}^N (x_i - \bar{x}_N)^2 \quad (4.19)$$

begins to converge when the number of samples is around 50. Here,  $N$  is the number of samples,  $x_i$  is the  $i$ -th sample and  $\bar{x}_N$  is the sample mean. If  $x_i$ s are vectors, the  $L_2$  norm is chosen to determine the distance between each sample and the sample mean.

In order to know how good the numerical simulation of the stochastic differential equation, the accuracy of the time discrete approximation is considered. Two basic approaches are employed for this FSI model. Firstly, the mean error is estimated [33]. Take the mean of the stochastic differential Eq. (4.12), the solution is

$$E(X_T) = E(X_0)e^{aT}. \quad (4.20)$$

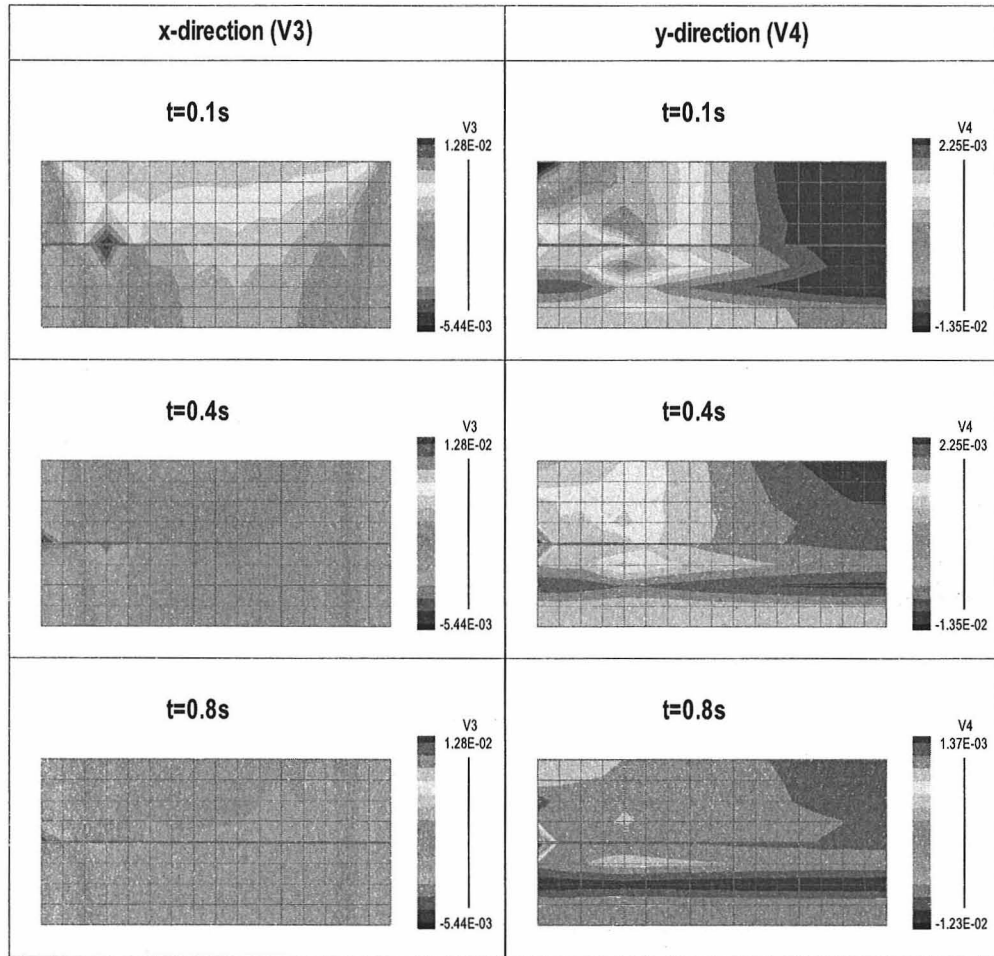


**Figure 4.32** Displacement wave propagation of transient analysis with white noise.

For any given initial value, repeat  $N$  different simulations of sample path by implicit Euler method. Then use  $M$  different initial values, i.e., generating a series of trajectories with distinct initial values. The mean error of the  $j$ -th batch by the statistic is

$$\hat{\mu}_j = \frac{1}{N} \sum_{k=1}^N Y_{T,k,j} - E(X_T) \quad (4.21)$$

for  $j = 1, 2, \dots, M$ , and their average is

$$\hat{\mu} = \frac{1}{MN} \sum_{j=1}^M \sum_{k=1}^N Y_{T,k,j} - E(X_T), \quad (4.22)$$

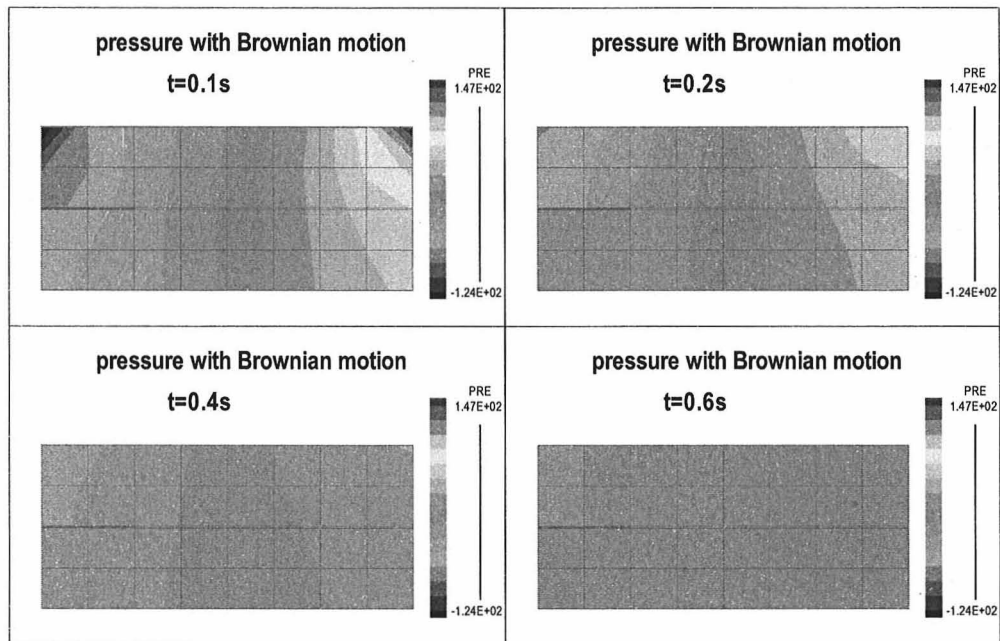


Figure 4.33 Pressure wave propagation of transient analysis with white noise.

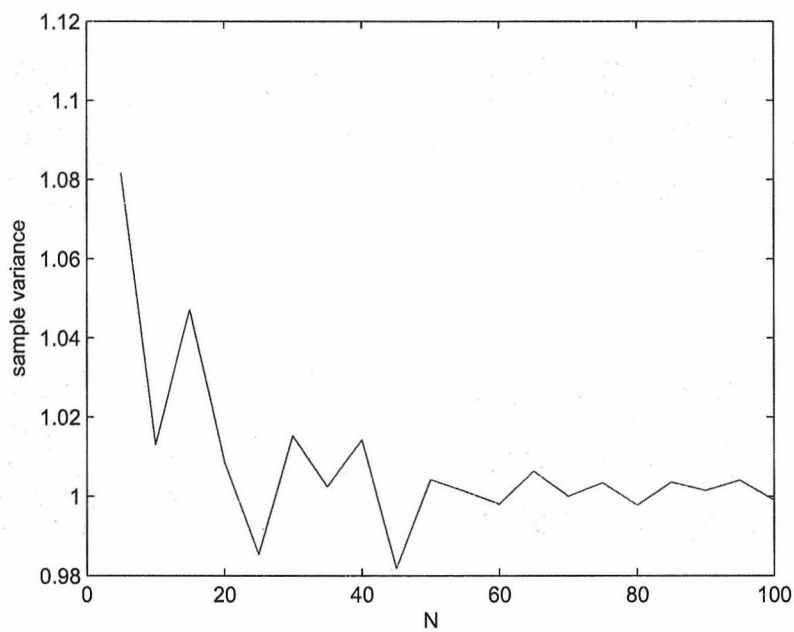


Figure 4.34 Sample variance *vs.* sample number.

where  $Y_{T,k,j}$  represents the  $k$ -th numerical simulation with the  $j$ -th initial value at time  $T$ . The variance of the batch average  $\hat{\mu}_j$  can be estimated by

$$\hat{\sigma}_\mu^2 = \frac{1}{M-1} \sum_{j=1}^M (\hat{\mu}_j - \hat{\mu})^2. \quad (4.23)$$

For the student t-distribution with  $M-1$  degree of freedom, a 90% confidence interval ( $\alpha = 0.1$ ) for the mean error  $\mu$  is

$$(\hat{\mu} - \Delta\hat{\mu}, \hat{\mu} + \Delta\hat{\mu}) \quad (4.24)$$

with

$$\Delta\hat{\mu} = t_{1-\alpha, M-1} \sqrt{\frac{\hat{\sigma}_\mu^2}{M}}. \quad (4.25)$$

Figs. 4.35 and 4.36 show the confidence intervals of displacement and velocity for increasing number of batches, respectively. It can be seen from both figures that the length of the interval decreases as the number of batches increases. In other words, 90% of the times that upper and lower thresholds are calculated, the true mean lies below the upper threshold and above the lower threshold. As the number of batches increases, the range between upper and lower thresholds gets smaller and smaller.

In addition to the confidence interval with different initial conditions, the confidence intervals for increasing number of time snapshots based on the mean error are also considered. Figs. 4.37 and 4.38 show that the confidence interval increases as time passes, because the error between the explicit solution and numerical simulation accumulates gradually as time passes.

Next, since the analytic solution is known for the SDE (Eq.(3.20)), the absolute error can be further taken account to test whether or not a good pathwise approximation is realized. Unlike the procedure of mean error, the same sample path of the Wiener process generating the explicit and numerical solution should be employed.

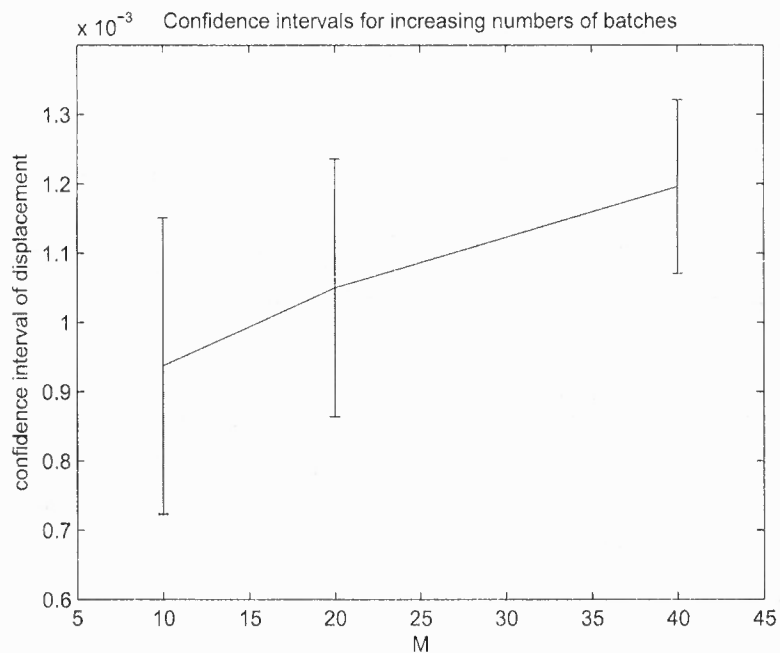


**Figure 4.35** Confidence intervals of displacement for increasing number of batches based on mean error.

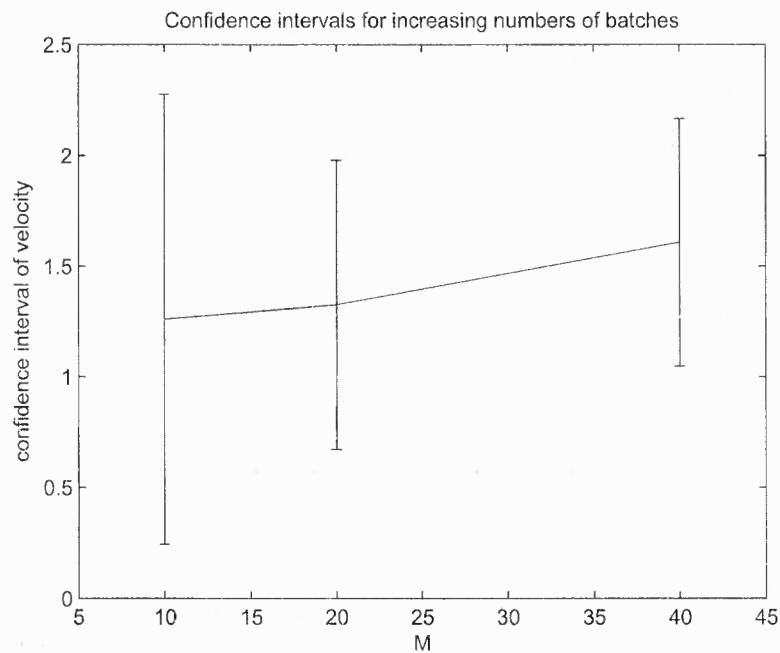


**Figure 4.36** Confidence intervals of velocity for increasing number of batches based on mean error.

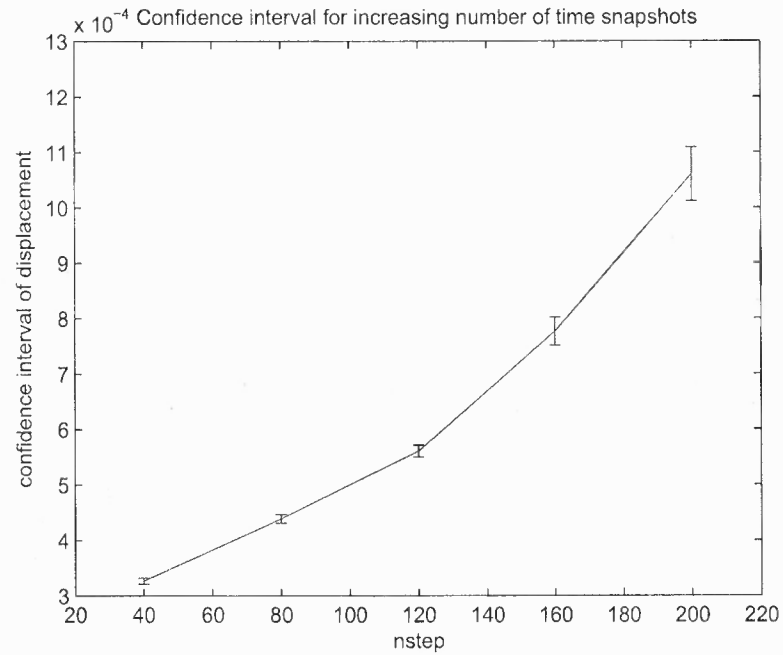


**Figure 4.37** Confidence intervals of displacement for increasing number of snapshots based on mean error.

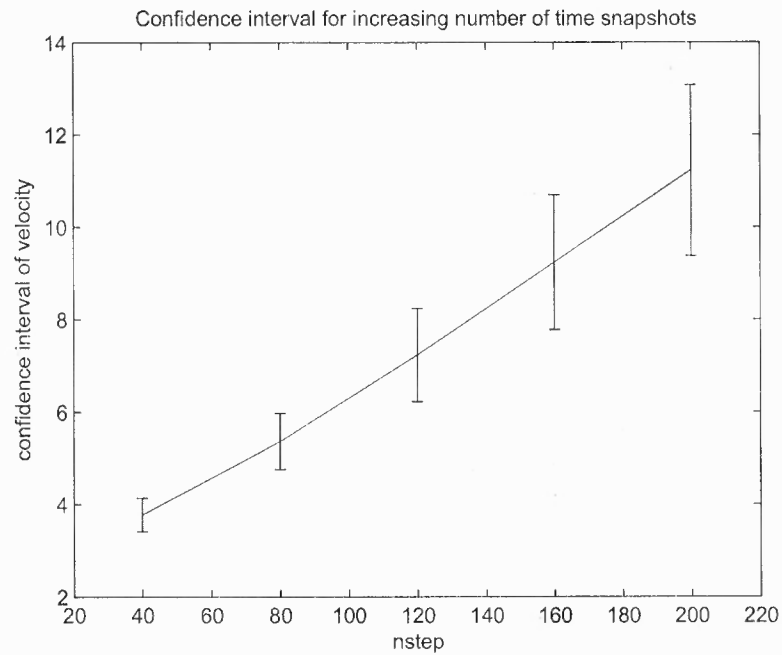


**Figure 4.38** Confidence intervals of velocity for increasing number of snapshots based on mean error.

Repeat  $N$  different simulations of sample path of the Ito process and their implicit Euler approximation with the same sample paths of the Wiener process. Consider the absolute error [28] by the statistic at time  $T$ :

$$\epsilon = \frac{1}{N} \sum_{k=1}^N |X_{T,k} - Y_{T,k}|. \quad (4.26)$$

Then, arrange  $M$  batches with  $N$  simulations for each and estimate the average error

$$\epsilon_j = \frac{1}{N} \sum_{k=1}^N |X_{T,k,j} - Y_{T,k,j}| \quad (4.27)$$

and the mean of the batch averages is

$$\hat{\epsilon} = \frac{1}{NM} \sum_{j=1}^M \sum_{k=1}^N |X_{T,k,j} - Y_{T,k,j}|. \quad (4.28)$$

The variance of the batch average can be estimated by the formula

$$\hat{\sigma}_\epsilon^2 = \frac{1}{M-1} \sum_{j=1}^M (\epsilon_j - \hat{\epsilon})^2. \quad (4.29)$$

Same as the formula for mean error, the  $100(1 - \alpha)\%$  confidence interval with  $M - 1$  degree of degree based on student t-distribution has the form

$$(\hat{\epsilon} - \Delta\hat{\epsilon}, \hat{\epsilon} + \Delta\hat{\epsilon}) \quad (4.30)$$

with

$$\Delta\hat{\epsilon} = t_{1-\alpha, M-1} \sqrt{\frac{\hat{\sigma}_\epsilon^2}{M}}. \quad (4.31)$$

Figs. 4.39 and 4.40 show the confidence intervals based on absolute error *vs.* the number of batches  $M$  of displacement and velocity. From both of the figures, it can be observed that the confidence interval gets smaller as the number of batches increases. That is because  $\Delta\hat{\epsilon}$  decreases as  $M$  increases.

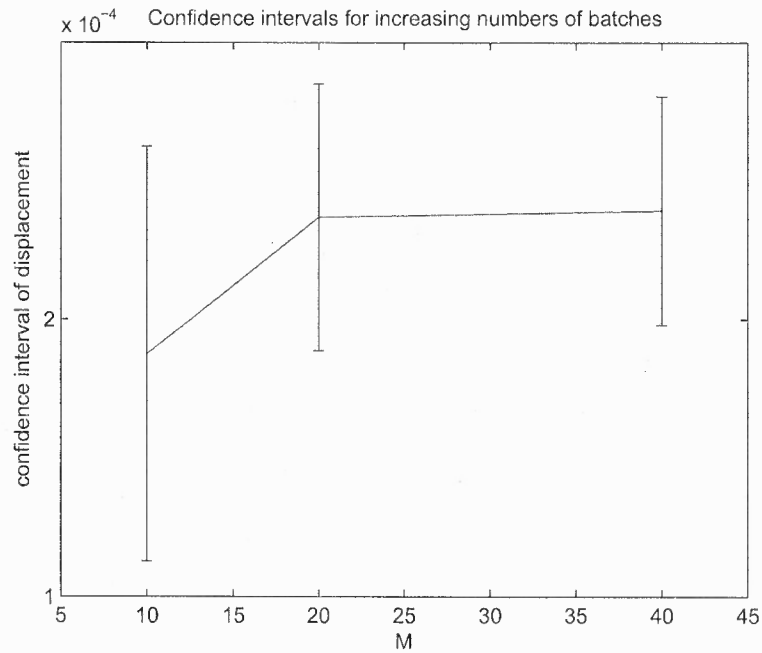


**Figure 4.39** Confidence intervals of displacement for increasing number of batches based on absolute error.

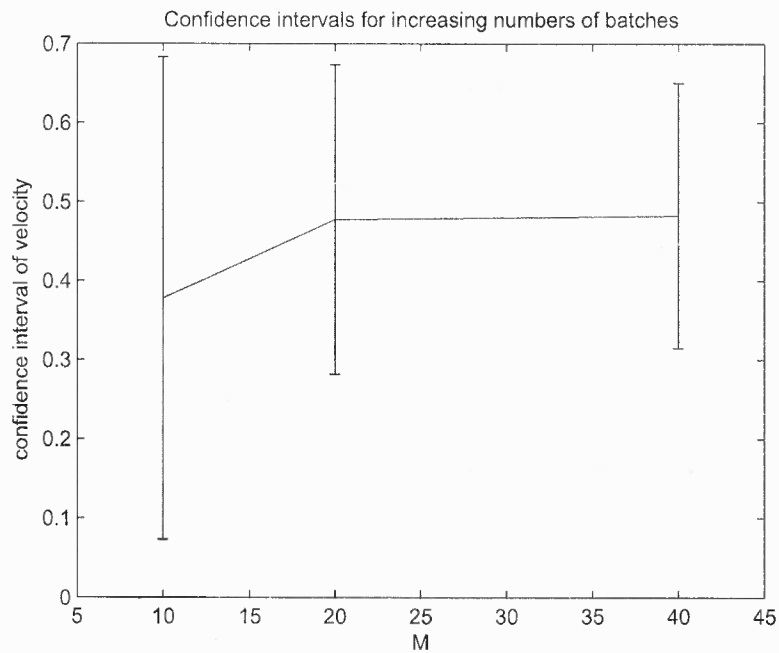


**Figure 4.40** Confidence intervals of velocity for increasing number of batches based on absolute error.

### 4.3 Three Masses Connected to the Walls with Springs

This 1-D problem is considered in order to understand the relationship between eigenvalues/ eigenmodes calculated by mode superposition method and principal values/ components by principal component analysis. In addition, the effect of white noise on the system is also tested.

The mathematical model, shown in Fig. 4.41 is composed of three masses with mass  $m$ ,  $2m$  and  $3m$  respectively and four springs with the same stiffness coefficient  $k$ . Both sides of the system are attached to the fixed wall.

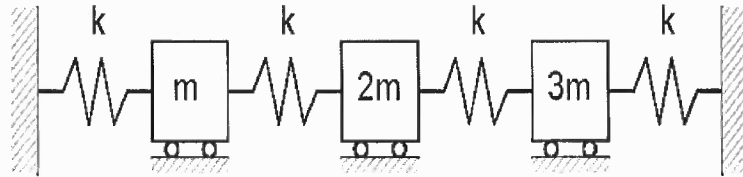


**Figure 4.41** Model III: Three masses connected to the walls with springs.

The mathematical model indicates three degrees of freedom. Therefore, the equilibrium Eq. of the system can be directly assembled:

$$\mathbf{M}\ddot{\mathbf{x}} + \mathbf{K}\mathbf{x} = \mathbf{R}(t) \quad (4.32)$$

with  $\mathbf{x} = [x_1 \ x_2 \ x_3]^T$ ,

$$\mathbf{M} = \begin{pmatrix} m & 0 & 0 \\ 0 & 2m & 0 \\ 0 & 0 & 3m \end{pmatrix} \quad \text{and} \quad \mathbf{K} = \begin{pmatrix} 2k & -k & 0 \\ -k & 2k & -k \\ 0 & -k & 2k \end{pmatrix}.$$

Table 4.3 shows the root of eigenvalues, which is the natural frequencies, and the corresponding eigenvectors by solving the generalized eigenvalue problem

$$\mathbf{K}\boldsymbol{\phi} = \omega^2\mathbf{M}\boldsymbol{\phi}. \quad (4.33)$$

The numerical results are exactly the same as the analytic solutions.

**Table 4.3** Eigenvalues and Eigenvectors

number	root of eigenvalue	eigenvector
1	1.18161	0.40298, 0.46837, 0.27219
2	2.23607	-0.40825, 0.40825, 0.40825
3	3.45502	0.06539, -0.33758, 0.87135

In order to activate the system, the initial force (impulse) is exerted on all the masses as the initial condition

$$\mathbf{R} = \alpha \phi_k \quad k = 1, 2, 3, \quad (4.34)$$

where  $\phi_k$  indicates the eigenvector corresponding to the  $k$ -th eigenvalue ( $k$  goes from 1 to 3 because of 3 degrees of freedom) and  $\alpha$  is a finite scalar. Implementing the Newmark method and record the iteration results for every time step  $\Delta t$  with  $\Delta t = 0.05$  and total number of time snapshots  $nstep = 100$ , a 3-by-100 matrix  $\mathbf{A}$  can be obtained. Each column of  $\mathbf{A}$  indicates the displacements of three masses. Then the singular value decomposition is performed on matrix  $\mathbf{A}$ .

In Table 4.4, the dominant singular vectors and their corresponding Raleigh-Ritz quotients are shown. Based on linear algebra theory, the Raleigh-Ritz quotients must lie between the minimal and maximal eigenvalues. From the table, it can be easily observed that the dominant singular vectors behave as the corresponding eigenvectors and the Raleigh-Ritz quotients are approximately equal to the corresponding root of eigenvalues in Table 4.3. Most importantly, if unique-frequency excitations nearing a generic natural frequency are imposed on the system, e.g.,  $R_i = \alpha \text{eigve}(i, k) \sin(\omega_k t)$ , the resonance phenomenon will occur. Here,  $\text{eigve}(i, k)$  represents the  $i$ -th eigen vector corresponding to the  $k$ -th eigenvalue  $\omega_k$ .

In addition, it also can be noticed that the Raleigh-Ritz quotients will converge around some typical quantities as the number of snapshot  $nstep$  increases. Figs. 4.42,

**Table 4.4** SVD and Raleigh-Ritz Results with Initial Impulse

k	dominant singular vector	Raleigh-Ritz quotient
1	-0.39637, -0.69160, -0.60381	1.18175
2	-0.59924, -0.58138, 0.55137	2.23570
3	-0.93295, 0.35454, -0.06248	3.45481

4.43, and 4.44 show this phenomenon for different initial forces loaded on the masses. For example, when the initial forces are proportional to the eigenmodes corresponding to the first natural frequency, the Raleigh-Ritz quotient goes to a limit between 1.18 and 1.19, which is quite close to the first natural frequency of the system, shown in dashed line. The second and third Raleigh-Ritz quotients approach to 2.23 and 3.45 respectively, consistent with the corresponding natural frequencies. Based on these figures, it also can be further proposed that the Raleigh-Ritz approximations begin to converge at some certain quantity of  $nstep$ . For this test problem,  $nstep = 50$  is the critical point. The results will not become more accurate if the number of time snapshots increases.

In order to verify the principal components of the transient data, principal component analysis is employed to the system. If the initial force is set to be the eigenmodes corresponding to the first natural frequency, the percentages of variance can be obtained, which are 96.6129%, 2.4230%, 0.9640%. In other words, only the first principal component is enough to depict the motion of the system. Likewise, this result is suitable for other initial force which is proportional to a single eigenvectors. If  $k = 2$  and  $k = 3$ , the percentages of the variance are 74.7747%, 18.0146%, 7.2107% and 88.9409%, 6.4401%, 4.6190% respectively.

Sub-figures to the left of Fig. 4.45 show the power of three masses and their summation. Similarly, the power of the scores is plotted from  $k = 1$  to  $k = 3$  to the right. There are two points worth mentioning: first, the principal score is good

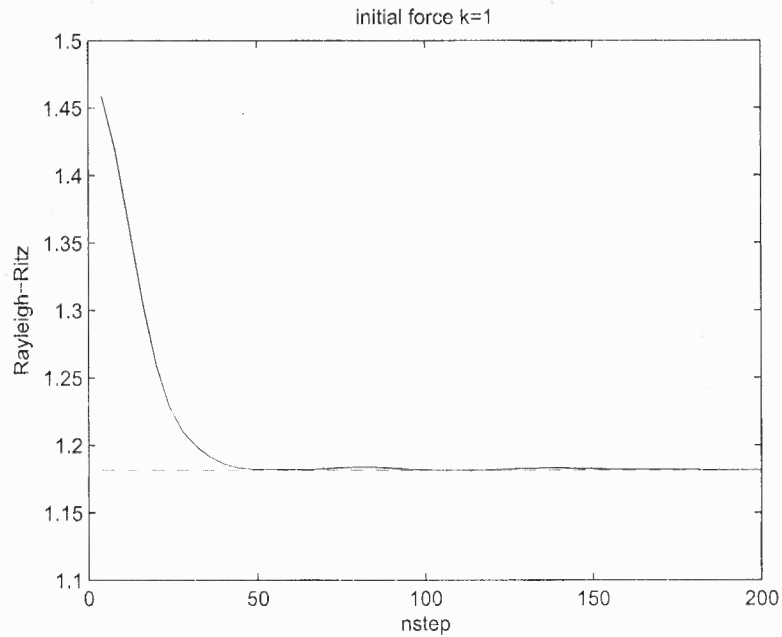


**Figure 4.42** Rayleigh-Ritz quotients *vs. nstep* activated by initial force proportional to the first eigenmode.

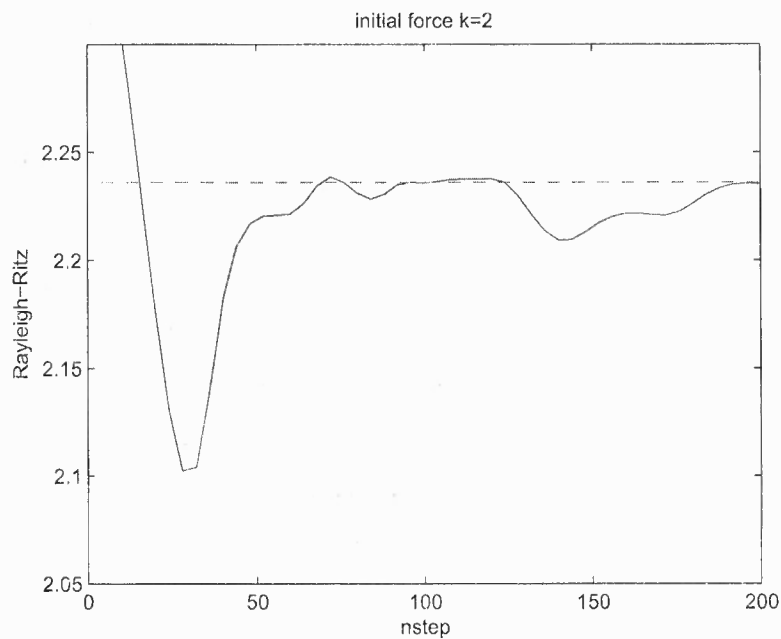


**Figure 4.43** Rayleigh-Ritz quotients *vs. nstep* activated by initial force proportional to the second eigenmode.

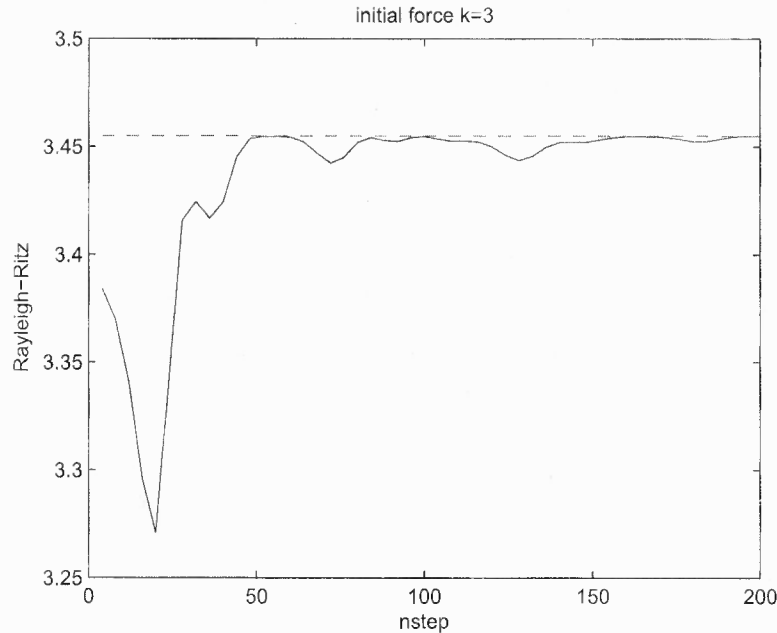


**Figure 4.44** Rayleigh-Ritz quotients *vs. nstep* activated by initial force proportional to the third eigenmode.

enough to describe the energy of the systems, since its power is almost the same as the total power of the three masses; Second, the figures also show that the spikes happen at certain natural frequencies. For example, when  $k = 1$ , there is a spike at  $f = 0.2$  (as the data cursor indicated). That is to say, the energy focuses on the angular frequency  $\omega = 2\pi f = 1.2566\text{rad/s}$ , which approaches the first natural frequency  $\omega_1 = 1.1816\text{rad/s}$ . Similarly, for  $k = 2$  and  $k = 3$ , the spikes happen at  $\omega = 2.5133\text{rad/s}$  and  $\omega = 3.1416\text{rad/s}$  respectively, compared to the second ( $\omega_2 = 2.2361\text{rad/s}$ ) and third ( $\omega_3 = 3.4550\text{rad/s}$ ) natural frequency.

Now, let us consider the spring system with Brownian motion. Assume the exterior force  $\mathbf{R}(t) = \mathbf{V}(t)$ , where  $\mathbf{V}(t)$  is a vector of white noise.

$$\text{Let } \begin{pmatrix} y_1 \\ y_2 \\ y_3 \end{pmatrix} = \begin{pmatrix} \dot{x}_1 \\ \dot{x}_2 \\ \dot{x}_3 \end{pmatrix}. \text{ The SDE then becomes}$$

$$\begin{pmatrix} \dot{x}_1 \\ \dot{x}_2 \\ \dot{x}_3 \\ \dot{y}_1 \\ \dot{y}_2 \\ \dot{y}_3 \end{pmatrix} = - \begin{pmatrix} 0 & 0 & 0 & -1 & 0 & 0 \\ 0 & 0 & 0 & 0 & -1 & 0 \\ 0 & 0 & 0 & 0 & 0 & -1 \\ 2k/m & -k/m & 0 & 0 & 0 & 0 \\ -k/2m & k/m & -k/2m & 0 & 0 & 0 \\ 0 & -k/3m & 2k/3m & 0 & 0 & 0 \end{pmatrix} \begin{pmatrix} x_1 \\ x_2 \\ x_3 \\ y_1 \\ y_2 \\ y_3 \end{pmatrix} + \begin{pmatrix} 0 \\ 0 \\ 0 \\ 1/m \\ 1/2m \\ 1/3m \end{pmatrix} \cdot \begin{pmatrix} 0 \\ 0 \\ 0 \\ V_1(t) \\ V_2(t) \\ V_3(t) \end{pmatrix}. \quad (4.35)$$

Let  $\mathbf{X} = \begin{pmatrix} x_1 \\ x_2 \\ x_3 \\ y_1 \\ y_2 \\ y_3 \end{pmatrix}$ ,  $\mathbf{a} = \begin{pmatrix} 0 & 0 & 0 & -1 & 0 & 0 \\ 0 & 0 & 0 & 0 & -1 & 0 \\ 0 & 0 & 0 & 0 & 0 & -1 \\ 2k/m & -k/m & 0 & 0 & 0 & 0 \\ -k/2m & k/m & -k/2m & 0 & 0 & 0 \\ 0 & -k/3m & 2k/3m & 0 & 0 & 0 \end{pmatrix}$ ,

$\mathbf{b} = \begin{pmatrix} 0 \\ 0 \\ 0 \\ 1/m \\ 1/2m \\ 1/3m \end{pmatrix}$  and  $\mathbf{V} = \begin{pmatrix} 0 \\ 0 \\ 0 \\ V_1(t) \\ V_2(t) \\ V_3(t) \end{pmatrix}$ , the same Eq. for 1-degree-of-freedom

system can be derived as in Chapter 3

$$d\mathbf{X} = -\mathbf{a}\mathbf{X}dt + \mathbf{b}d\mathbf{W}(t), \quad (4.36)$$

where  $d\mathbf{W}(t) = \mathbf{V}(t)dt$ ,  $\mathbf{W}(t)$  is a vector of Brownian motion.

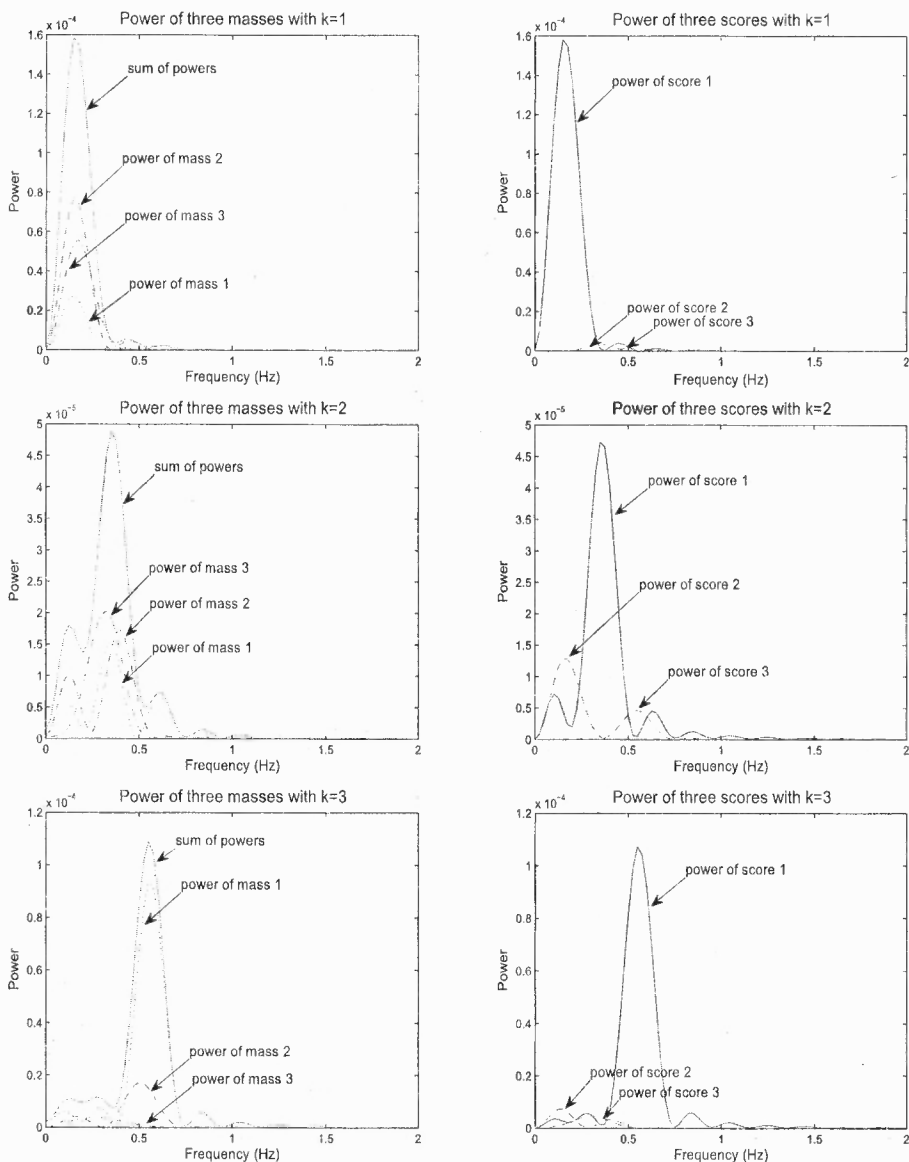


Figure 4.45 Power spectrum *vs.* frequency with  $k=1,2,3$ .

Consider the mass motions activated by the initial displacement given, i.e.,  $\mathbf{X}_0$ . In order to compare the explicit and numerical solution, Fig. 4.46 shows the results of displacement and velocity for one mass. Fig. 4.47 shows two realizations of displacement and velocity as time passes with noise by implicit Euler method for three springs.

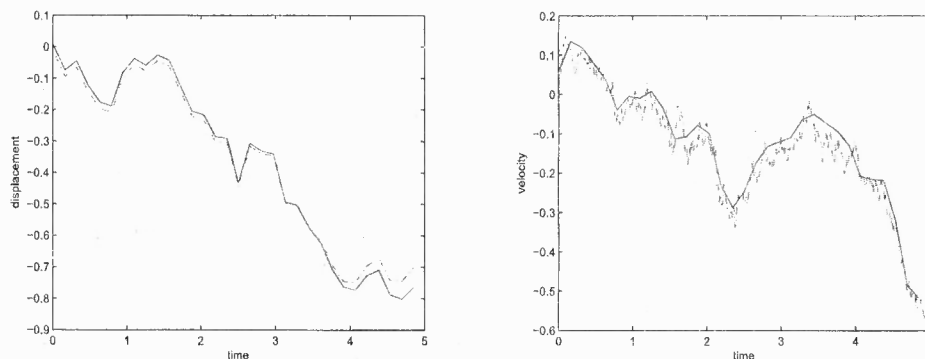


Figure 4.46 Explicit and numerical solution of displacement/velocity *vs.* time.

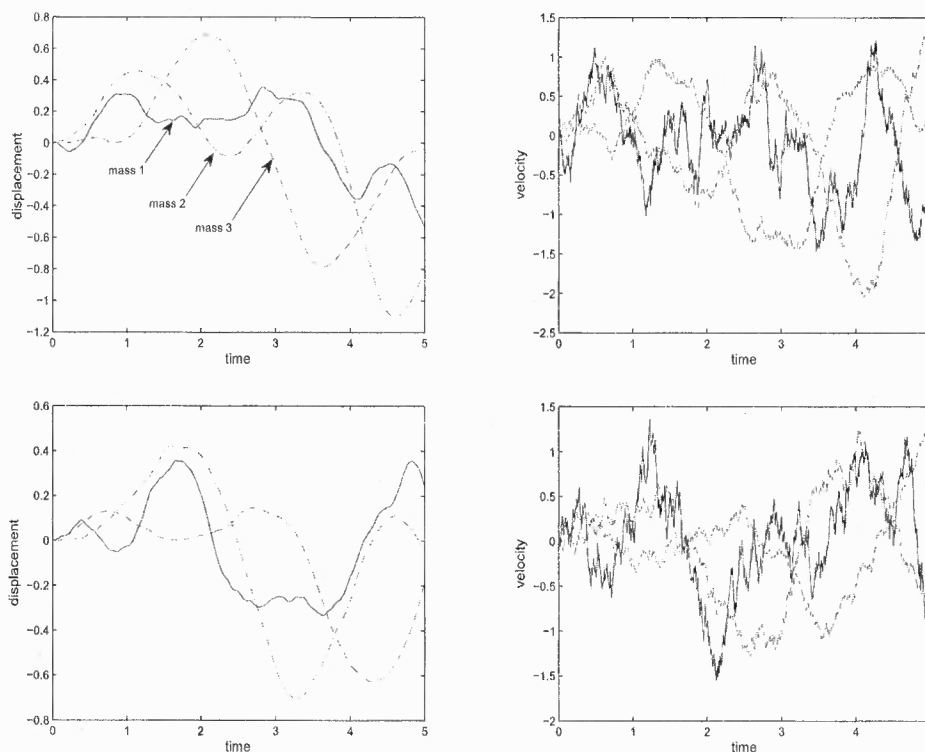
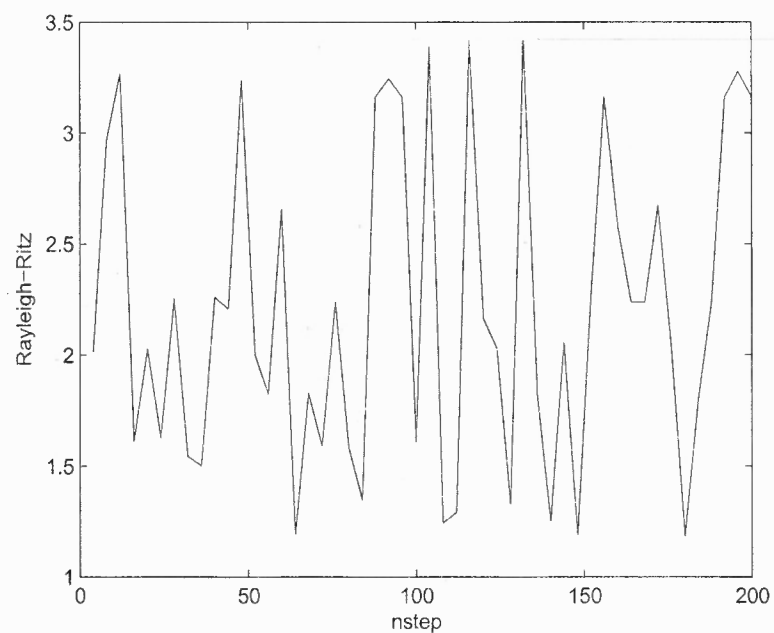


Figure 4.47 Displacement/velocity *vs.* time by implicit Euler method.

Repeat  $N = 100$  numerical simulations for each given number of snapshots  $nstep$ , take the dominant singular vector and calculate Rayleigh-Ritz quotient, the mean of the quotients is plotted *vs.*  $nstep$  in Fig. 4.48. This indicates that when

the white noise is involved and plays an important role in the transient analysis, the Raleigh-Ritz quotients oscillate and do not approach a limit.



**Figure 4.48** Raleigh-Ritz quotient *vs* nstep with noise.

## CHAPTER 5

### CONCLUSION

The acoustoelastic problems are very typical, since their free surface modes, structural modes and acoustic modes are coupled together. Mixed finite element formulation, i.e.,  $\mathbf{u}/p$  and  $\mathbf{u} - p - \Lambda$  formulations can be implemented to capture all of them, simultaneously. Moreover, the crucial advantage of  $\mathbf{u} - p - \Lambda$  formulation is that it can solve the acoustic fluid-structure interaction problems without introducing the spurious non-zero frequencies and many zero frequencies by comparing the number of zero frequencies with the mathematical prediction. In addition, it is proved that the mixed finite element formulations with the corresponding mixed elements satisfy the inf-sup condition in two approaches. The first one is the traditional method, which is considering the inf-sup value based on the formulation in Chapter 2. The second way comes from the idea of singular value decomposition. Essentially, the inf-sup value corresponds to the minimum non-zero singular value of matrix  $\mathbf{K}_{us}$ . Therefore, this singular value is chosen to replace the role of inf-sup value. In this way, the solvability and stability condition of mixed elements is testified for the FSI system.

In the model reduction section, the Rayleigh-Ritz quotient calculated through the first singular vector is compared with the natural frequency obtained by mode superposition method. Excellent agreements are obtained for the results of low frequency, eg, sloshing and structural frequency. It is also verified that SVD-based model reduction methods are reliable by comparing the original transient data with recovered simulation results composed by only a few dominant principal components for single mode excitation. As for the combined eigenmodes, the effects of time step  $dt$  on principal component analysis need to be identified in order to capture all three modes. Therefore, root mean square deviation is introduced and the effects of the

parameter  $dt$ ,  $dT$  and  $nstep$  on it are considered. The dimension of the transient data matrix can be further decreased by relaxation method combined with SVD or PCA, since the motion of the system in some time instances can be directly skipped. Energy calculated by first-order Sobolev norm verify the accuracy of the recovered data.

In addition to the deterministic FSI system, i.e., all the material properties, excitations are determined without any random quantities, the system with additive noise is also considered in order to testify the effect of white noise. Therefore, the matrix-form Langevin equation is involved and implicit Euler method is employed as the numerical simulation method for the sake of stability condition. Similar as the procedure in the deterministic system, SVD is performed and Rayleigh-Ritz quotient *vs.* number of snapshots is plotted. It is found that the Rayleigh-Ritz quotient decays from the first beginning. That is because the perturbation of the Brownian motion greatly dissipates the energy of the system and therefore significantly changes the configuration of the Rayleigh-Ritz quotients.

## APPENDIX A

### NEWMARK METHOD

The Newmark integration scheme can be considered as an extension of the linear acceleration method. In order to solve the equilibrium equation

$$\mathbf{M}\ddot{\mathbf{U}} + \mathbf{C}\dot{\mathbf{U}} + \mathbf{K}\mathbf{U} = \mathbf{R}, \quad (\text{A.1})$$

,i.e.,

$$\mathbf{M}\ddot{\mathbf{U}}^{t+\Delta t} + \mathbf{C}\dot{\mathbf{U}}^{t+\Delta t} + \mathbf{K}\mathbf{U}^{t+\Delta t} = \mathbf{R}^{t+\Delta t}, \quad (\text{A.2})$$

the following assumptions are used:

$$\dot{\mathbf{U}}^{t+\Delta t} = \dot{\mathbf{U}}^t + [(1 - \delta)\ddot{\mathbf{U}}^t + \delta\ddot{\mathbf{U}}^{t+\Delta t}]\Delta t, \quad (\text{A.3})$$

$$\mathbf{U}^{t+\Delta t} = \mathbf{U}^t + \dot{\mathbf{U}}^t\Delta t + [(\frac{1}{2} - \alpha)\ddot{\mathbf{U}}^t + \alpha\ddot{\mathbf{U}}^{t+\Delta t}]\Delta t^2, \quad (\text{A.4})$$

where  $\delta$  and  $\alpha$  are parameters that can be determined to obtain integration accuracy and stability. For example, when  $\delta = \frac{1}{2}$  and  $\alpha = \frac{1}{4}$ , trapezoidal rule is proposed; when  $\delta = \frac{1}{2}$  and  $\alpha = \frac{1}{6}$ , the Wilson  $\theta$  method with  $\theta = 1$  is obtained.

Solving from (A.2) for  $\ddot{\mathbf{U}}^{t+\Delta t}$  in terms of  $\mathbf{U}^{t+\Delta t}$  and then substituting for  $\ddot{\mathbf{U}}^{t+\Delta t}$  into (A.1), the equations for  $\ddot{\mathbf{U}}^{t+\Delta t}$  and  $\dot{\mathbf{U}}^{t+\Delta t}$  can be obtained, each in terms of the unknown displacements  $\mathbf{U}^{t+\Delta t}$  only. These two relations for  $\dot{\mathbf{U}}^{t+\Delta t}$  and  $\ddot{\mathbf{U}}^{t+\Delta t}$  are substituted into (A.3) to solve for  $\mathbf{U}^{t+\Delta t}$ , after which, using (A.1) and (A.2),  $\ddot{\mathbf{U}}^{t+\Delta t}$  and  $\dot{\mathbf{U}}^{t+\Delta t}$  can also be calculated.

Step-by-step solution using Newmark integration method.

A. Initial calculations:

1. Initialize  $\mathbf{U}^0, \dot{\mathbf{U}}^0$  and  $\ddot{\mathbf{U}}^0$ .

2. Select time step  $\Delta t$  and parameters  $\alpha$  and  $\delta$  and calculate integration constants:

$$\delta \geq 0.50, \quad \alpha \geq 0.25(0.5 + \delta)^2$$

$$a_0 = \frac{1}{\alpha \Delta t^2}, \quad a_1 = \frac{\delta}{\alpha \Delta t}, \quad a_2 = \frac{1}{\alpha \Delta t}, \quad a_3 = \frac{1}{2\alpha} - 1;$$

$$a_4 = \frac{\delta}{\alpha} - 1, \quad a_5 = \frac{\Delta t}{2} \left( \frac{\delta}{\alpha} - 2 \right), \quad a_6 = \Delta t(1 - \delta), \quad a_7 = \delta \Delta t;$$

3. Form effective stiffness matrix  $\hat{\mathbf{K}}$ :  $\hat{\mathbf{K}} = \mathbf{K} + a_0 \mathbf{M} + a_1 \mathbf{C}$ .

4. Triangularize  $\hat{\mathbf{K}}$ :  $\hat{\mathbf{K}} = \mathbf{LDL}^T$ .

B. For each time step:

1. Calculate effective loads at time  $t + \Delta t$ :

$$\hat{\mathbf{R}}^{t+\Delta t} = \mathbf{R}^{t+\Delta t} + \mathbf{M}(a_0 \mathbf{U}^t + a_2 \dot{\mathbf{U}}^t + a_3 \ddot{\mathbf{U}}^t) + \mathbf{C}(a_1 \mathbf{U}^t + a_4 \dot{\mathbf{U}}^t + a_5 \ddot{\mathbf{U}}^t). \quad (\text{A.5})$$

2. Solve for displacement at time  $t + \Delta t$ :

$$\mathbf{LDL}^T \mathbf{U}^{t+\Delta t} = \hat{\mathbf{R}}^{t+\Delta t}. \quad (\text{A.6})$$

3. Calculate accelerations and velocities at time  $t + \Delta t$ :

$$\ddot{\mathbf{U}}^{t+\Delta t} = a_0 (\mathbf{U}^{t+\Delta t} - \mathbf{U}^t) - a_2 \dot{\mathbf{U}}^t - a_3 \ddot{\mathbf{U}}^t, \quad (\text{A.7})$$

$$\dot{\mathbf{U}}^{t+\Delta t} = \dot{\mathbf{U}}^t + a_6 \ddot{\mathbf{U}}^t + a_7 \ddot{\mathbf{U}}^{t+\Delta t}. \quad (\text{A.8})$$

## APPENDIX B

### PATHWISE AND MOMENTS APPROXIMATIONS

A realistic problem, which depicts a mass immersed into fluid is considered. The mass is suspended vertically by a soft spring affixed to a rigid wall. In this model, the effect of vertical Brownian motion on the oscillation of the mass is considered. Therefore, an SDE can be built up to describe the mass motion:

$$m\ddot{x} + kx = V(t). \quad (\text{B.1})$$

Let  $y = \dot{x}$  and rewrite the above SDE, the equation above can be rewritten as

$$\begin{pmatrix} \dot{x} \\ \dot{y} \end{pmatrix} = - \begin{pmatrix} 0 & -1 \\ k/m & 0 \end{pmatrix} \begin{pmatrix} x \\ y \end{pmatrix} + \begin{pmatrix} 0 \\ 1/m \end{pmatrix} V(t). \quad (\text{B.2})$$

Assuming  $\mathbf{X} = \begin{pmatrix} x \\ y \end{pmatrix}$ ,  $\mathbf{a} = \begin{pmatrix} 0 & -1 \\ k/m & 0 \end{pmatrix}$ ,  $\mathbf{b} = \begin{pmatrix} 0 \\ 1/m \end{pmatrix}$ , the stochastic differential equation as above can be derived as

$$d\mathbf{X} = -\mathbf{a}\mathbf{X}dt + \mathbf{b}d\mathbf{W}(t). \quad (\text{B.3})$$

Assume  $m = 1$ ,  $k = 4$ , and  $\mathbf{X}_0 = [0.02 \ 0.01]^T$ , the explicit solution and numerical simulation can be calculated based on Eq. (3.20) and (3.21). Fig. B.1 shows a realizations of displacement and velocity as time passes. Solid curve represents the explicit solution while the dashed curve describes the solution by implicit Euler method.

The errors of stochastic time discrete approximation comparing with explicit solution are shown as follows. Figs. B.2 and B.3 show the confidence intervals based on absolute error *vs* the number of batches  $M$  in displacement and velocity.

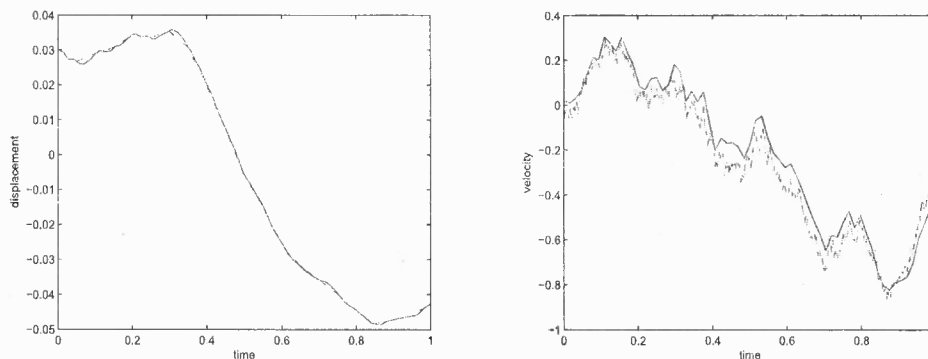


**Figure B.1** Explicit and numerical solution of displacement/velocity *vs.* time.

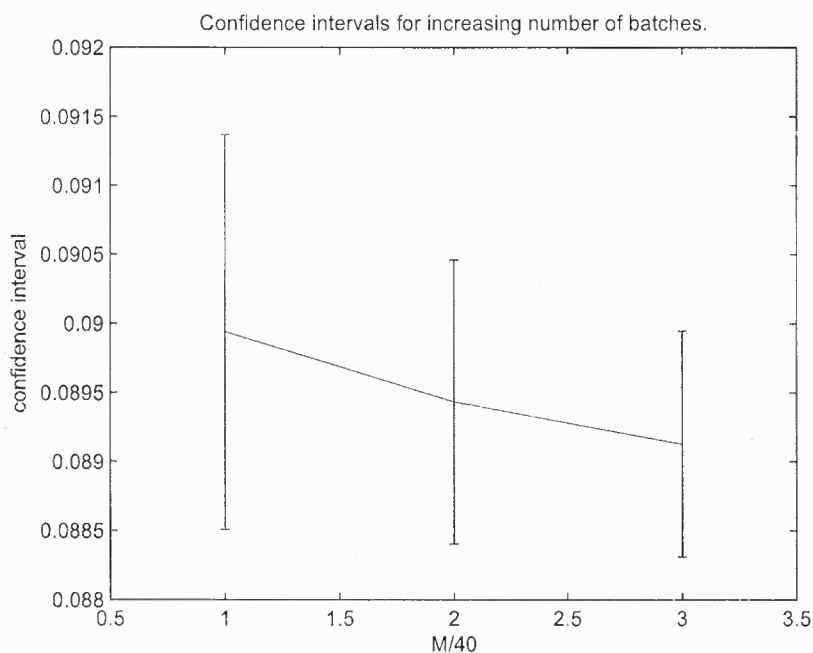


**Figure B.2** Confidence intervals of displacement for increasing numbers of batches based on absolute error.

Figs. B.4 and B.5 plot the confidence interval *vs* number of time snapshots with  $M = 50$  batches based on the mean error. Both figures show the confidence interval increases as time increases. It can be seen that the mean of displacement increases as the number of snapshots increases, because of the augment of the initial values;

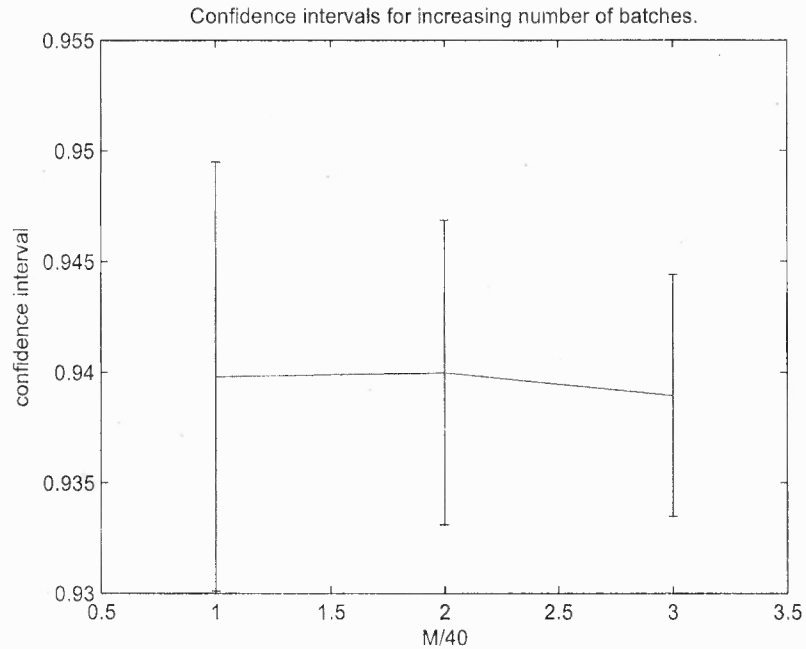


**Figure B.3** Confidence intervals of velocity for increasing numbers of batches based on absolute error.

whereas the mean of velocity decreases due to the property of the spring, which says that displacement is inversely proportional to velocity.

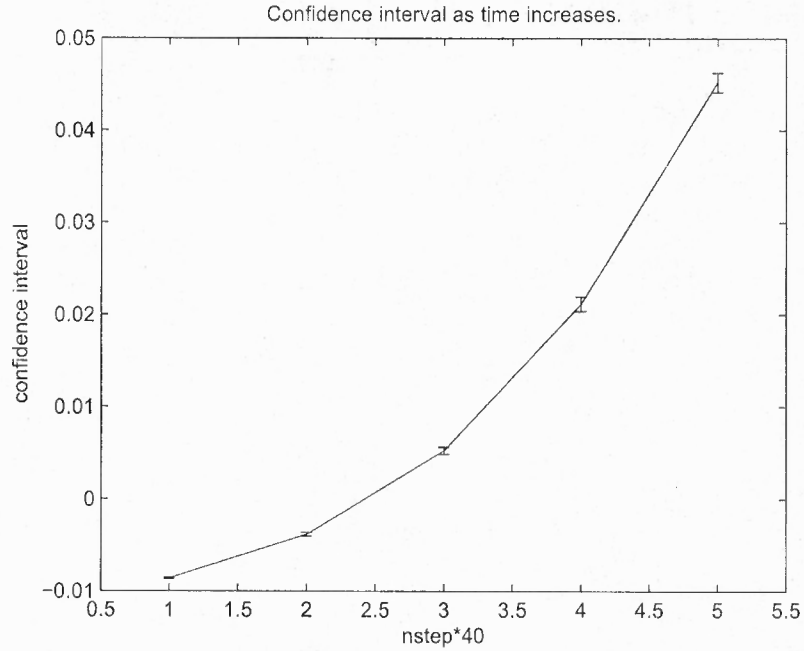


**Figure B.4** Confidence intervals of displacement for increasing time based on mean error.

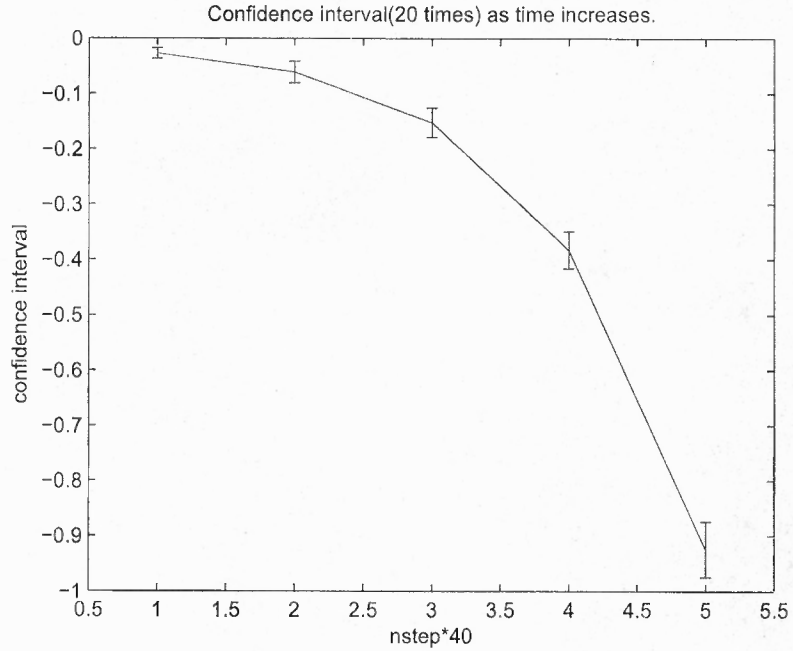


**Figure B.5** Confidence intervals of velocity for increasing time based on mean error.

## APPENDIX C

### ORTHONORMAL BASIS CHOSEN BY SINGULAR VALUES

Suppose a set of orthonormal basis  $\phi_1, \phi_2, \dots, \phi_m$  is chosen in  $R^m$  arbitrarily. Each sample  $a_i$  can be decomposed into:

$$a_i = \alpha_{1i}\phi_1 + \alpha_{2i}\phi_2 + \dots + \alpha_{mi}\phi_m. \quad (\text{C.1})$$

Assume the first  $r$  basis vectors are determined to approximate the samples, we have

$$\tilde{a}_i = \alpha_{1i}\phi_1 + \alpha_{2i}\phi_2 + \dots + \alpha_{ri}\phi_r. \quad (\text{C.2})$$

Then the mean square error is

$$\epsilon^2 = \sum_{i=1}^n \|a_i - \tilde{a}_i\|^2 = \sum_{i=1}^n \left\| \sum_{j=r+1}^m \alpha_{ji}\phi_j \right\|^2 = \sum_{i=1}^n \sum_{j=r+1}^m \alpha_{ji}^2. \quad (\text{C.3})$$

Since  $\phi_j^T a_i = \alpha_{ji}$ , the above equation becomes

$$\epsilon^2 = \sum_{i=1}^n \sum_{j=r+1}^m \phi_j^T a_i a_i^T \phi_j = \sum_{j=r+1}^m \phi_j^T A A^T \phi_j. \quad (\text{C.4})$$

Now, the problem turns to find the orthonormal basis vectors  $\phi_{r+1}, \phi_{r+2}, \dots, \phi_m$  such that  $\epsilon^2$  is minimum. By Lagrangian multiplier method, we build up the function

$$L = \sum_{j=r+1}^m \phi_j^T A A^T \phi_j - \sum_{i=r+1}^m \sum_{j=r+1}^m \gamma_{ij} (\phi_i^T \phi_j - \delta_{ij}). \quad (\text{C.5})$$

Take the first derivative with respect to  $\phi_j$  and set it to be zero, we have

$$\frac{\partial L}{\partial \phi_j} = 2A A^T \phi_j - 2\gamma_{ij} \sum_{i=r+1}^m \phi_i, \quad j = r+1, r+2, \dots, m. \quad (\text{C.6})$$

Assume  $\Phi = (\phi_{r+1}, \phi_{r+2}, \dots, \phi_m)$  and

$$\Gamma = \begin{pmatrix} \gamma_{r+1,1} & \gamma_{r+1,2} & \cdots & \gamma_{r+1,m} \\ \gamma_{r+2,1} & \gamma_{r+2,2} & \cdots & \gamma_{r+2,m} \\ \cdots & \cdots & \cdots & \cdots \\ \gamma_{m,1} & \gamma_{m,2} & \cdots & \gamma_{m,m} \end{pmatrix}. \quad (\text{C.7})$$

Then equation( C.6) can be written into matrix form

$$\frac{\partial L}{\partial \Gamma} = 2AA^T\Phi - 2\Phi\Gamma = 0. \quad (\text{C.8})$$

Therefore, we have the relationship

$$AA^T\Phi = \Phi\Gamma. \quad (\text{C.9})$$

Since  $\Gamma$  is a semi-definite matrix, there exists an orthonormal matrix  $P$  such that  $\Lambda = P^T\Gamma P$ , where  $\Lambda = \text{diag}\{\lambda_1, \lambda_2, \dots, \lambda_{m-r}\}$  is a diagonal matrix. Postmultiplying equation( C.9) by  $P$ , we obtain

$$AA^T\Phi P = \Phi\Gamma P = \Phi P P^T\Gamma P = \Phi P\Lambda. \quad (\text{C.10})$$

Let  $U = \Phi P$ , then equation above turns to be an eigen problem  $AA^TU = U\Lambda$ , where each column of  $U$  is an eigenvector of matrix  $AA^T$ . Correspondingly, each diagonal entree of matrix  $\Lambda$  is an eigenvalue. Go back to the mean square error equation and represent it in term of matrix form, we have

$$\epsilon^2 = \text{tr}(\Phi^T AA^T\Phi) = \text{tr}(P^T\Phi^T AA^T\Phi P) = \text{tr}(U^T U\Lambda) = \text{tr}(\Lambda) = \sum_{i=r+1}^m \lambda_i. \quad (\text{C.11})$$

Therefore, in order to minimize the mean-square error, the best way is to choose the first  $m - r$  minimal eigen values. In other words, choosing the singular vectors corresponding to the first few eigenvalues with determined number of  $r$ , the recovered data is most significantly close to the original data.

## REFERENCES

- [1] M. F. Azeez and A. F. Vakakis. Proper orthogonal decomposition (POD) of a class of vibroimpact oscillations. *J. Sound Vibr.*, 240:859–889, 2001.
- [2] W. Bao, X. Wang, and K. J. Bathe. On the inf-sup condition of mixed finite element formulations for acoustic fluid. *Math. Meth. Mod. App. Sci*, 11:883–901, 2001.
- [3] K. J. Bathe. *Finite Element Procedures*. Englewood Cliffs, NJ: Prentice-Hall, 1996.
- [4] K. J. Bathe and W. Hahn. On transient analysis of fluid-structure systems. *Comput. Struct.*, 10:383–391, 1978.
- [5] T. B. Belytschko and J. M. Kennedy. A fluid-structure finite element method for the analysis of reactor safety problems. *Nucl. Engng Des.*, 38:71–81, 1976.
- [6] T. B. Belytschko and J. M. Kennedy. Computer models for subassembly simulation. *Nucl. Engng Des.*, 49:17–38, 1978.
- [7] E. Biglieri and K. Yao. Some properties of singular value decomposition and their applications to digital signal processing. *Sig. Proc.*, 18:277–289, 1989.
- [8] D. Chapelle and K. J. Bathe. The inf-sup test. *Comput. Struct.*, 47:537–545, 1993.
- [9] H. C. Chen and R. L. Taylor. Vibration analysis of fluid-solid systems using a finite element displacement formulation. *Int. J. Numer. Meth. Engng*, 29:683–698, 1990.
- [10] R. W. Clough and E. L. Wilson. Early finite element research at Berkeley. *National Conference on Computational Mechanics*, Aug.:4–6, 1999.
- [11] A. Craggs. The transient response of a coupled plate-acoustic system using plate and acoustic finite elements. *J. Sound Vibr.*, 15:509–528, 1971.
- [12] W. Dubitzky, D. P. Berrar and M. Granzow. *A Practical Approach to Microarray Data Analysis*. Kluwer academic publishers, 2004.
- [13] W. J. T. Daniel. Performance of reduction methods for fluid-structure and acoustic eigenvalue problems. *Int. J. Numer. Meth. Engng*, 15:1585–1594, 1980.
- [14] G. H. Dunteman. *Principal Components Analysis*. California: Sage Publications Inc., California, 1989.
- [15] A. Ern and J. L. Guermond. *Theory and Practice of Finite Elements*, volume 159. Springer-Verlag, New York, 2003.
- [16] G. C. Everstine. A symmetric potential formulation for fluid-structure interaction. *J. Sound Vibr.*, 79:157–160, 1981.

- [17] G. C. Everstine. Finite element formulations of structural acoustics problems. *Comput. Struct.*, 65:307–321, 1997.
- [18] G. C. Everstine, E. A. Schroeder, and M. S. Marcus. The dynamic analysis of submerged structures. *NASTRAN: Users' Exper.*, NASA TM X-3278:419–429, 1975.
- [19] B. F. Feeny. On proper orthogonal co-ordinates as indicators of modal activity. *J. Sound Vibr.*, 255:805–817, 2002.
- [20] G. E. Forsythe, M. A. Malcolm, and C. B. Moler. *Computer methods for mathematical computations*. Englewood Cliffs, NJ: Prentice-Hall, 1977.
- [21] T. L. Geers. Residual potential and approximate methods for three-dimensional fluid-structure interaction problems. *J. Acoust. Soc. Am.*, 49:1505–1510, 1971.
- [22] M. A. Hamdi and Y. Ousset. A displacement method for the analysis of vibrations of coupled fluid-structure systems. *Int. J. Numer. Meth. Engng*, 13:139–150, 1978.
- [23] P. Holmes, J. L. Lumley, and G. Berkooz. *Turbulence, Coherent Structures, Dynamical Systems and Symmetry*. Cambridge University Press, 1996.
- [24] I. T. Jolliffe. *Principal Component Analysis*. Springer, 2002.
- [25] S. L. Marple Jr. *Digital Spectral Analysis with applications*. Englewood Cliffs, NJ: Prentice-Hall, 1987.
- [26] L. Kiefling and G. C. Feng. Fluid-structure finite element vibrational analysis. *AIAA J.*, 14:199–203, 1976.
- [27] V. C. Klema and A. J. Laub. The singular value decomposition: its computation and some applications. *IEEE Trans. Auto. Control*, 25:164–176, 1980.
- [28] P. E. Kloeden and E. Platen. *Numerical Solution of Stochastic Differential Equations*. Springer, 1999.
- [29] G. L. Lawson and R. J. Hanson. *Solving Least Squares Problems*. Englewood Cliffs, NJ: Prentice-Hall, 1974.
- [30] Y. C. Liang, H. P. Lee, S. P. Lim, W. Z. Lin, K. H. Lee, and C. G. Wu. Proper orthogonal decomposition and its applications - part i: theory. *J. Sound Vibr.*, 252:527–544, 2002.
- [31] Y. C. Liang, W. Z. Lin, H. P. Lee, S. P. Lim, and K. H. Lee. Proper orthogonal decomposition and its applications - part ii: model reduction for mems dynamical analysis. *J. Sound Vibr.*, 256:512–532, 2002.
- [32] J. L. Lumley. *Stochastic Tools in Turbulence*. Academic Press, New York, 1970.

- [33] G. N. Milstein. A method of second-order accuracy integration of stochastic differential equations. *Theor. Prob. Appl.*, 23:396–401, 1978.
- [34] H. Morand and R. Ohayon. Substructure variational analysis of the vibrations of coupled fluid-structure systems. finite element results. *Int. J. Numer. Meth. Engng*, 14:741–755, 1979.
- [35] W. C. Muller. Simplified analysis of linear fluid-structure interaction. *Int. J. Numer. Meth. Engng*, 17:113–121, 1981.
- [36] L. G. Olson and K. J. Bathe. A study of displacement-based fluid finite elements for calculating frequencies of fluid and fluid-structure systems. *Nucl. Engng Des.*, 76:137–151, 1983.
- [37] L. G. Olson and K. J. Bathe. Analysis of fluid-structure interactions. a direct symmetric coupled formulation based on the fluid velocity potential. *Comput. Struct.*, 21:21–32, 1985.
- [38] I. K. Mortimer P. D. Drummond. Computer simulations of multiplicative stochastic differential equations. *J. Comput. Phys.*, 93, No.1:144–170, 1991.
- [39] L. Sirovich. Turbulence and dynamics of coherent structures. part 1:coherent structures. *Q. Appl. Math.*, 45:561–571, 1987.
- [40] X. Wang. *Fundamentals of Fluid-Solid Interactions*, volume 8. Elsevier Science.
- [41] X. Wang and K. J. Bathe. Displacement/pressure based mixed finite element formulations for acoustic fluid-structure interaction problems. *Int. J. Numer. Meth. Engng*, 40:2001–2017, 1997.
- [42] X. Wang and K. J. Bathe. On mixed elements for acoustic fluid-structure interactions. *Math. Meth. Mod. App. Sci.*, 7:329–343, 1997.
- [43] E. L. Wilson and M. Khalvati. Finite elements for the dynamic analysis of fluid-solid systems. *Int. J. Numer. Meth. Engng*, 19:1657–1668, 1983.
- [44] O. C. Zienkiewicz and R. E. Newton. Coupled vibrations of a structure submerged in a compressible fluid. *Proceedings of the International Ship Structure Congress, Symposium on the FEM-Technique, Stuttgart.*, 1969.